Uncertainty Quantification with Shallow Water Equations

Dissertation

submitted to and approved by the

Carl-Friedrich-Gauss Faculty
University of Braunschweig – Institute of Technology

and the

Faculty of Engineering
University of Florence

in candidacy for the degree of a
Doktor der Naturwissenschaften (Dr. rer. nat.) /
Dottore di Ricerca in Risk Management on the Built Environment[1]

by

Dishi Liu
Born on 27. 06. 1970
from Liaoning, China

Submitted on	September 1, 2009
Oral examination on	November 6, 2009
Professorial advisors	Prof. Hermann G. Matthies Prof. Ignazio Becchi Prof. Enrica Caporali

2010

[1]Either the German or the Italian form of the title may be used.

Abstract

The present thesis proposes two novel numerical integration techniques as an endeavour to break the "curse of dimension" to high-dimensional integrations, and investigates the efficiency of some numerical techniques quantifying uncertainty in the solution of shallow water equations (SWE) for flood modelling.

The novel *uncorrelated dimensions* (UD) quadrature and compound UD quadrature have convergence rates independent of the dimension number of the integration if the integrand can be expressed by a multilinear functional of any integrable functions.

A stochastic SWE model is set up by a probabilistic parameterisation of the SWE, whereon UD and quasi-Monte Carlo quadrature show advantage on the integrations for statisctics. The model is also approximated by polynomial chaos expansions and Karhunen-Loève expansions which are shown to be effective data compression techniques.

Acknowledgements

This thesis is based on my research work in the Institute of Scientific Computing, Technical University of Braunschweig and in the University of Florence during the years from 2004 to 2009.

Foremost, I would like to thank Professor Dr. Hermann G. Matthies for the opportunity of this doctorate study, for setting me up in the project by establishing important academic cooperations, for giving me freedom to develop my own idea, and for his always accessible guidance and support which are essential to the completion of the thesis.

Also, I would like to thank Professor Ignazio Becchi for his professional advice on the Hydraulic aspect of the study, and Professor Enrica Caporali for helpful discussions.

I feel also grateful to Dr. Sandra Soares-Frazão in the *Université Catholique de Louvain* who provided me the numerical solver of shallow water equations and kind helps on operating it. My special gratitude also goes to Elmar Zander for many valuable discussions, Dr. Andreas Keese for the help on StoFEM, Martin Krosche for the help on Smolyak quadrature, and Dominik Jürgens for his constant rescue in my operations of Linux systems.

I thank Prof. Dr. Udo Peil and Prof. Dr. Claudio Borri for the chance to study within the International Graduate College of "Risk Management of Natural and Civilisation Hazards on Buildings and Infrastructure" of the Deutsche Forschungsgemeinschaft.

Last but not least, my thankfulness also goes to all my colleagues in the Institute of Scientific Computing and the International Graduate College for the cooperative working environment.

Braunschweig, August 2009 Dishi Liu

Contents

Chapter 1

Introduction

Flood has been ever a threat to people live in river valleys or on floodplains. In the recent years, population growth, urbanisation processes and over-exploitations of natural resources brought about more and more imbalances in the global ecological system. As a consequence, emergencies of natural disasters increased in both their frequencies and scales. The worldwide statistics in [10] shows the number of floods occurred during the period from 1990 to 1998 was more than the total number of the previous three and a half decade, from 1950 to 1985, and the economic losses caused by floods in the former period is more than seven times of those in the latter. The floods in China in the year 1996 and 1998 caused losses of 30 billion and 26.5 billion US dollars respectively. The flood in Bangladesh in 1991 killed 140,000 people. According to [8], the economic losses caused by floods in Europe during the period from 1970 to 1988 and the period from 1989 to 2006 is about 50 and 90 billion US dollars respectively. Floods are part of the nature and will continue to occur in the future, however, the flood risk can be mitigated if an appropriate flood protection system is built.

An effective flood protection system should be a combination of both structural measures, like dams, reservoirs, etc, and non-structural measures among which flood forecast-warning systems are very important [77]. A flood forecast-warning system is usually based on modelling of floods which gives predictions on the range of inundation, inundated water depth and velocity, etc. Analysis of the characteristics of flood waves shows the area of flooding is generally much larger than the inundated water depth and the water pressure is hydrostatic, i.e., the flood waves has the characteristics of shallow water waves [128]. Therefore, shallow water equations (SWE) are usually taken as the mathematical tool for flood modelling.

1.1 Motivation

As pointed out in [81], managing uncertainties is essential for flood modelling practice. Flood modelling with SWE is subject to uncertainties due to various reasons, e.g. difficulties in obtaining precise knowledge of topography or inflow discharge data. Minor uncertainties can have an amplified impact in some instances and lead to potential occurrence of rare catastrophic events. It is thus important to quantify the effect of the uncertainties on the results of the models.

Uncertainty can be taken into account by setting the SWE model in a probabilistic framework, i.e. to combine the model and a probabilistic description of the input parameters. This combination is hereafter called the stochastic SWE model. In this setting, the uncertainties are represented by random variables/fields, therefore the response is also a random variable/field resulted by the propagation of the random input through the model.

The SWE model is often solved by numerical methods with non-negligible computation cost, and the stochastic SWE model introduces an extra stochastic dimension making it more expensive to investigate. The numerical integration and approximation of the model pose a challenge by which this research is motivated.

1.2 Objectives

The objectives of this research are to investigate the efficiency of some numerical techniques for the integration and approximation of the stochastic SWE model, and try to devise new techniques with stronger capacity. Complement of the objectives would facilitate the manage of flood risk by more efficient investigations of flood behaviours.

1.3 In the context of risk management

Flood risk R can be defined as the product of failure probability (expected value of danger) P_f and expected value of the consequence damage D [107]:

$$R = P_f \cdot D$$

The failure probability P_f can be further broken down as [5]

$$P_f = P_H \cdot P_{EX} \cdot P_V$$

with P_H, P_{EX} and P_V denote the probability of hazard, exposure and vulnerability. This work is to facilitate the evaluation of P_H, the probability of flood hazard, in the risk management process, corresponding to the *Hazard analysis* part in the framework of risk management as shown in Figure 1.1.

1.4 Structure of the thesis

The thesis is written in six chapters. Chapter 1 gives the general introduction of the research. Chapter 2 reviews the literatures in the related fields, Chapter 3 gives the settings of the stochastic SWE model under study and discretisation of the random fields. Chapter 4 investigates the efficiency of some techniques for numerical integrations, also describes and analyses two novel methods, uncorrelated dimensions quadrature and its compound version. Chapter 5 introduces approximations of the model with polynomial chaos and Karhunen-Loève expansion. Chapter 6 gives some conclusion remarks.

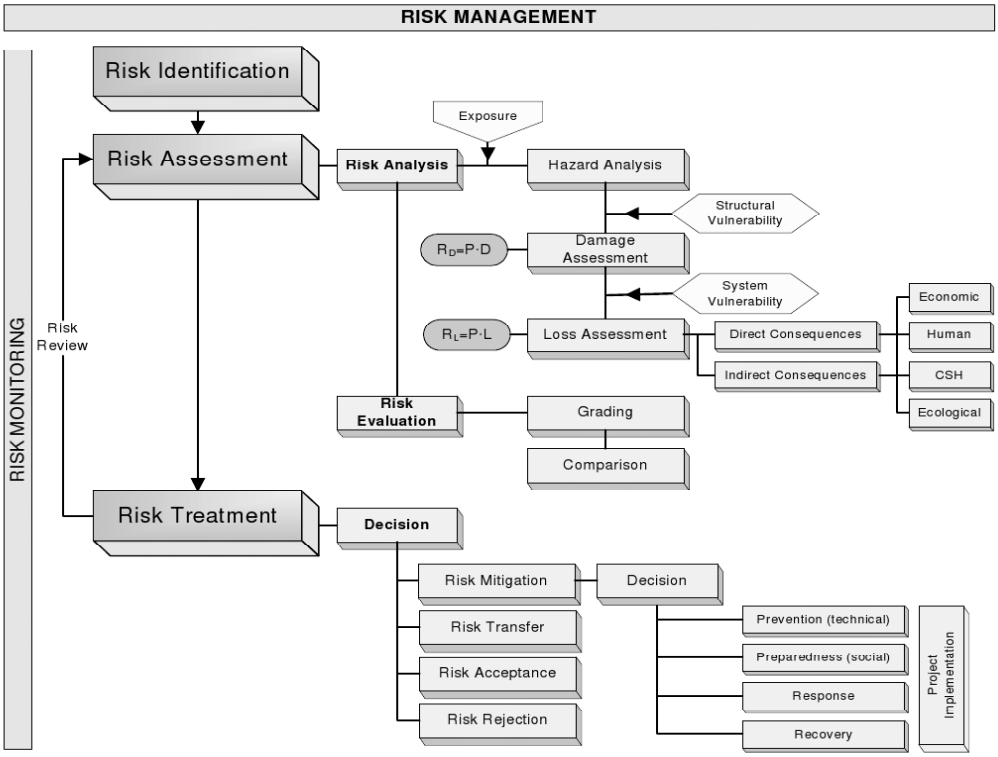

Figure 1.1: Overview of the whole risk management process, from [107]

Chapter 2

Uncertainty and Flood Modelling

The shallow water equations (SWE) is often taken as a mathematical model for the simulation of flood flows [23]. But some parameters in the SWE which can substantially affect the simulation are associated with uncertainties. Incorporating these uncertainties into the SWE gives rise to stochastic SWE which provides a new possibility of more robust flood simulation as well as to pose a computational challenge.

2.1 Shallow water equations on flood modelling

2.1.1 Introduction of shallow water equations

This section gives a brief introduction to the SWE, including its derivation, parametrisation and some properties of its solutions. It will be seen that although simplifying assumptions have been made in the derivation of SWE, there are still some parameters not yet theoretically determined and empirical values have to be adopted for practical uses [131].

2.1.1.1 Derivation of shallow water equations

Shallow-water flows are flows with their vertical scales much smaller than typical horizontal scales (ratio less than 0.05 as suggested in [78]), and are nearly horizontal so that a hydrostatic pressure distribution applies. This category includes many natural flow phenomena, e.g. atmospheric flows [49], tidal flows [51], river floods [102] and tsunamis [118] etc.

The SWE, also known as Saint-Venant equations named after *Barré de Saint Venant* who first derived the one-dimensional (1-D) SWE for unsteady open channel flow in 1871 [32], is widely used to describe shallow water flows. It is a specialisation of the incompressible Navier-Stokes equations (NSE) by an averaging on the vertical dimension. The 2-dimensional (2-D) SWE are hence computationally much cheaper than the 3-D NSE by generally demanding less than 1 percent of the computation effort needed by the latter [57].

The NSE stems from the principles of mass and momentums conservation. In Cartesian coordinate these principles can be written as

$$\frac{\partial \rho}{\partial t} + \nabla \cdot (\rho \boldsymbol{v}) = 0 \tag{2.1}$$

$$\frac{\partial}{\partial t}(\rho \boldsymbol{v}) + \nabla \cdot (\rho \boldsymbol{v} \otimes \boldsymbol{v}) = \nabla \cdot \boldsymbol{\Sigma} + \rho \boldsymbol{f}_b \tag{2.2}$$

where ρ is the fluid density, $\boldsymbol{v} = (v_x, v_y, v_z)^T$ is the velocity vector, ∇ is the Nabla operator, $\boldsymbol{\Sigma}$ is the stress tensor and $\rho \boldsymbol{f}_b$ is the body force exerted on the fluid.

In the special case of Newtonian flows, one can use the Newtonian constitutive relation [9] to relate the stress tensor $\boldsymbol{\Sigma}$ to the velocity $\boldsymbol{v}$, this leads to the NSE. On further assuming incompressibility for the fluid, which means the density ρ is a constant, one obtains the incompressible NSE [136] directly from which the SWE will be derived,

$$\nabla \cdot \boldsymbol{v} = 0 \tag{2.3}$$

$$\frac{\partial \boldsymbol{v}}{\partial t} + \nabla \cdot (\boldsymbol{v} \otimes \boldsymbol{v}) = -\frac{1}{\rho} \nabla p + \nu \nabla^2 \boldsymbol{v} + \boldsymbol{f}_b \tag{2.4}$$

where p is the pressure, ν is the kinematic viscosity and ∇^2 the Laplace operator.

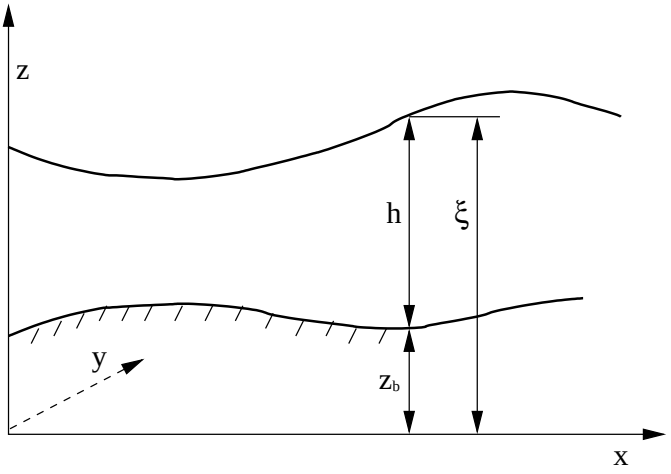

Figure 2.1: Schematic representation of a shallow water flow, from [136]

Consider a three-dimensional domain of free surface flow as illustrated in Figure 2.1 with ξ and z_b represent the free surface elevation and the bed elevation respectively. The SWE is derived by an integration of equations (2.3) and (2.4) over the vertical dimension z with the following boundary conditions and assumption:

- At the free surface and the bed, the vertical velocity components v_z's are

$$v_z|_{z=\xi} = \frac{\partial \xi}{\partial t} + v_x \frac{\partial \xi}{\partial x} + v_y \frac{\partial \xi}{\partial y} \quad \text{and} \quad v_z|_{z=z_b} = \frac{\partial z_b}{\partial t} + v_x \frac{\partial z_b}{\partial x} + v_y \frac{\partial z_b}{\partial y}$$

  and the shear stress items are

$$\nu \nabla^2 \begin{pmatrix} v_x \\ v_y \end{pmatrix}_{z=\xi} = \boldsymbol{\tau}_w \quad \text{and} \quad \nu \nabla^2 \begin{pmatrix} v_x \\ v_y \end{pmatrix}_{z=z_b} = \boldsymbol{\tau}_b$$

in which $\boldsymbol{\tau}_w$ and $\boldsymbol{\tau}_b$ denote the wind stress and the bed friction stress vectors respectively.

- A hydrostatic pressure distribution

$$p(z) = p_a + (\xi - z)\rho g, \quad z_b \leq z \leq \xi$$

applies, with p_a denotes the atmosphere pressure at the surface, g the acceleration of gravity.

- The vertical velocity v_z in the vertical range (z_b, ξ) is negligible.
- The bed elevation is stable, i.e., $\frac{\partial z_b}{\partial t} = 0$.

With the assumptions and boundary conditions given above, integrating NSE (2.3) and (2.4) from z_b to ξ on z dimension, one obtains the *conservative* form 2-D SWE [108, 154],

$$\frac{\partial h}{\partial t} + \nabla \cdot (h\boldsymbol{u}) = 0 \tag{2.5}$$

$$\frac{\partial (h\boldsymbol{u})}{\partial t} + \nabla \cdot (h\boldsymbol{u} \otimes \boldsymbol{u}) + gh\nabla h + \boldsymbol{\vartheta} = 0 \tag{2.6}$$

where now $\boldsymbol{u} = (u_x, u_y)^T$ is a 2-D depth-averaged velocity vector. The vector $\boldsymbol{\vartheta}$ represents the sum of external forces.

$$\boldsymbol{\vartheta} = gh\nabla z_b - \boldsymbol{\tau}_b - \boldsymbol{\tau}_w + \boldsymbol{\Omega}\boldsymbol{u} - h\nu_c\nabla^2\boldsymbol{u}, \quad \text{with} \quad \boldsymbol{\Omega} = \begin{pmatrix} 0 & -2\omega\sin\phi \\ 2\omega\sin\phi & 0 \end{pmatrix}$$

The term $\boldsymbol{\Omega}\boldsymbol{u}$ represents the Coriolis force, ω is the magnitude of the angular velocity of the earth, ϕ is the latitude. In the viscosity term, instead of kinematic viscosity ν, ν_c is used to represent the compound stress caused by molecular viscosity and turbulence effects, more about which is to be discussed in section 2.1.1.4.

If one expands the differential items in equation (2.6) and cancels some items by using the continuity equation (2.5), a non-conservative SWE is obtained [131], which can be written as

$$\frac{\partial \mathbf{w}}{\partial t} + \mathbf{A}(\mathbf{w})\frac{\partial \mathbf{w}}{\partial x} + \mathbf{B}(\mathbf{w})\frac{\partial \mathbf{w}}{\partial y} + \mathbf{Q} = 0 \tag{2.7}$$

$$\mathbf{w} = \begin{pmatrix} h \\ \boldsymbol{u} \end{pmatrix}, \ \mathbf{A}(\mathbf{w}) = \begin{pmatrix} u_x & h & 0 \\ g & u_x & 0 \\ 0 & 0 & u_x \end{pmatrix}, \ \mathbf{B}(\mathbf{w}) = \begin{pmatrix} u_y & 0 & h \\ 0 & u_y & 0 \\ g & 0 & u_y \end{pmatrix}, \ \mathbf{Q} = \begin{pmatrix} 0 \\ \boldsymbol{\vartheta}/h \end{pmatrix}$$

where $\mathbf{w}$ can be interpreted as a quantity to be transported, $\mathbf{A}$ and $\mathbf{B}$ are advection matrices in x and y direction. $\mathbf{Q}$ is a source term representing external influences.

Since the non-conservative SWE are obtained by performing differentiations of the primitive variables h and $\boldsymbol{u}$, it is also called a *differential* form of SWE. Cautions should be taken on using this form if there are discontinuities occurred in flows, in which case differentials no longer make sense and the problem can only have a weak solution [131]. In such situations only conservative form of SWE should be used.

2.1.1.2 Characteristic surfaces and dispersion relations

A solution of the 2-D SWE can be interpreted as a superposition of different waves, of which characteristic surfaces are the wave fronts.

To identify the characteristic surfaces one substitutes a plane wave solution $\mathbf{w} = \hat{\mathbf{w}} e^{i\theta(t,x,y)}$ into a homogeneous version of equation (2.7), with $\hat{\mathbf{w}}$ a constant and $\theta(t,x,y) = n_0 t + n_1 x + n_2 y$. It turns out plane waves are solutions only if

$$n_0 + n_1 u_x + n_2 u_y = 0 \tag{2.8}$$

or

$$n_0 + n_1 u_x + n_2 u_y = \pm c\sqrt{n_1^2 + n_2^2}\,, \quad c = \sqrt{gh} \tag{2.9}$$

Relations (2.8) and (2.9) describe two kinds of wave fronts or characteristic surfaces [136]. The relation (2.8) corresponds to a vorticity wave with the characteristic surface $\theta(t,x,y)$ fulfils the equation

$$\frac{\partial \theta}{\partial t} + u_x \frac{\partial \theta}{\partial x} + u_y \frac{\partial \theta}{\partial y} = 0 \tag{2.10}$$

This is a wave which moves with velocity $\boldsymbol{u}$, representing the transport of vorticity, i.e., the vorticity remains constant — so that is called a *Riemann invariant* — along this wave front. The relation (2.9) corresponds to gravity waves, of which the characteristic surface $\theta(t,x,y)$ fulfils

$$\frac{\partial \theta}{\partial t} + (u_x \pm c\cos\beta)\frac{\partial \theta}{\partial x} + (u_y \pm c\sin\beta)\frac{\partial \theta}{\partial y} = 0 \tag{2.11}$$

with β an arbitrary angle. On x dimension the wave moves with velocity $u_x \pm c$ and Riemann invariants $u_x \pm 2c$, while on y dimension with velocity $u_y \pm c$ and Riemann invariants $u_y \pm 2c$ [128].

Equation (2.8) and (2.9) also state relations of wave speed n_0 and wave numbers n_1 and n_2, which are called *dispersion relations*. More realistic dispersion relations could have been derived if the source term $\mathbf{Q}$ was taken into account, like in [136] and [131]. But in that situation, for the plane wave analysis to proceed a linearised SWE has to be used.

2.1.1.3 Boundary and initial conditions

Boundary and initial conditions have to be prescribed to make the shallow water equations well-posed. If one ignores the viscosity term $\nu_c \nabla^2 \boldsymbol{u}$, the SWE is a first-order hyperbolic system, while including it leads to a parabolic system. In these two cases different boundary conditions are expected for a well-posed system.

Hyperbolic cases In this situation, the number of boundary conditions in a point on the boundary must be equal to the number of characteristics entering the domain at that point [26]. Section 2.1.1.2 shows that it is the velocity normal to the boundary determines the number of incoming characteristics. If $\boldsymbol{n}$ is a unit vector normal to

Situation	Num. of outward characteristics	Num. of inward characteristics	Num. of necessary boundary conditions
$\boldsymbol{u}\cdot\boldsymbol{n} < -c$	0	3	3
$-c \leq \boldsymbol{u}\cdot\boldsymbol{n} < 0$	1	2	2
$0 \leq \boldsymbol{u}\cdot\boldsymbol{n} < c$	2	1	1
$\boldsymbol{u}\cdot\boldsymbol{n} \geq c$	3	0	0

Table 2.1: Number of necessary boundary conditions for hyperbolic SWE, from [131]

the boundary, pointing outward, the number of necessary boundary conditions are tabulated in Table 2.1.

The type of boundary conditions is related to what is transported by the corresponding characteristic surfaces. For gravity waves, value of h or $\boldsymbol{u}\cdot\boldsymbol{n}$, or a relation function $f(h,\boldsymbol{u})$ should be proscribed. For vorticity waves which is irrelevant to h, another velocity condition $\boldsymbol{u}\cdot\boldsymbol{s}$ has to be given, with $\boldsymbol{s}$ a unit tangential vector of the boundary [136].

On closed boundaries which are barriers of flow, $\boldsymbol{u}\cdot\boldsymbol{n}=0$, according to Table 2.1 only one condition is needed here which is of course just $\boldsymbol{u}\cdot\boldsymbol{n}=0$. However on free boundaries which are fictitious fluid-fluid boundaries delimiting the domain of interest, the prescription of correct boundary conditions is often difficult. Since these boundary conditions are determined by the domain outside the model on which one has very limited knowledge. It is likely that the boundary conditions prescribed are at least partially wrong. Wrong boundary conditions cause reflections to the outgoing waves. Many attempts have been made to minimise these spurious reflections, as in [33], [130], [55] and [56], but in general to eliminate them is impossible. A practical solution is to put the open boundary far enough away from the area of interest so that the influence of spurious reflections is sufficiently damped.

Initial conditions are also boundary conditions on the temporal dimension, so the above principles also apply. Since all characteristic enter the domain on this boundary, one needs to prescribe all the unknowns h and $\boldsymbol{u}$ for the initial condition, in compatibility with the boundary conditions.

Parabolic cases If one has the SWE as a parabolic system by including the viscosity term $\nu_c\nabla^2\boldsymbol{u}$, additional boundary conditions about velocity $\boldsymbol{u}$ are needed for the well-poseness.

On closed boundaries, a tangential velocity condition should be prescribed as either $\boldsymbol{u}\cdot\boldsymbol{s}=0$ for *no-slip* boundaries or $\frac{\partial\boldsymbol{u}}{\partial\boldsymbol{n}}\cdot\boldsymbol{s}=0$ for *free-slip* boundaries [131].

On free boundaries, the additional boundary conditions are again less evident. [127] proposed $\frac{\partial\boldsymbol{u}}{\partial\boldsymbol{n}}\cdot\boldsymbol{n}=0$ on inflow open boundaries and $\frac{\partial\boldsymbol{u}}{\partial\boldsymbol{n}}\cdot\boldsymbol{s}=0$ on outflow open boundaries.

2.1.1.4 Miscellaneous forces

Apart from the gravity, many other forces work on flood flows. These include bed friction stress, Coriolis stress, lateral stress caused by viscosity and turbulence, wind

stress, stress caused by atmospheric pressure gradients, etc. An intensive introduction and formulation of them can be found in [128]. In this section only wind stress, bed friction stress and lateral stress are discussed.

Wind stress The wind stress is a shear stress occurs on the surface of flow pointing to the direction of the wind. An accepted semi-empirical formula for the magnitude of the wind stress is given by Gill [43],

$$\boldsymbol{\tau}_w = \rho_{\text{air}}\, c_f\, \boldsymbol{v}_w\, |\boldsymbol{v}_w| \tag{2.12}$$

in which $\boldsymbol{v}_w$ is the wind speed and c_f is the friction coefficient. The wind speed is conventionally measured 10 meters above the flow surface. The friction coefficient is of the order 10^{-3} [131], but its value is highly variable and depends on the degree of irregularity of the flow surface which is not known a priori. Researchers rather relate the value of c_f to the wind speed, which is believed to be proportional to the degree of surface irregularity. Detailed review of literatures dealing this subject can be found in [106], or [39] where it is concluded for practical purposes that c_f can be related to wind speed measured in meters per second (m/s) by

$$c_f = 0.51\, |\boldsymbol{v}_w|^{0.46} \times 10^{-3} \tag{2.13}$$

or

$$c_f = (0.75 + 0.067\, |\boldsymbol{v}_w|) \times 10^{-3} \tag{2.14}$$

for flows more than 2.5 meters deep, in the range $4 < |\boldsymbol{v}_w| < 21$m/s. If $v_w < 4$m/s or water depth less than 2.5 meters the c_f is approximated by a constant 0.001 since surface irregularity is minor in these cases.

In [23] another formula of wind stress in terms of the relative velocity $\boldsymbol{v}_r = \boldsymbol{u} - \boldsymbol{v}_w$ between flow and wind is given:

$$\tau_w = -\frac{\rho_{\text{air}} c_f \boldsymbol{v}_r\, |\boldsymbol{v}_r|}{2} \tag{2.15}$$

Bed friction stress Bed friction stress is theoretically a *result* of the flow system, decided by the local force equilibrium at the flow bottom. But to close the SWE one needs an *a priori* expression of it in terms of the other variables such as flow velocities and depth.

In [23] the bed friction stress is expressed in a form of local force equilibrium :

$$\boldsymbol{\tau}_b = -\rho g h \boldsymbol{S}_f$$

where the non-dimensional *friction slope* $\boldsymbol{S}_f$ is to be related to flow velocity and bottom friction coefficient through Manning's equation in case of fully turbulent flow, or Darcy-Weisbach equation otherwise. [52] gives the following criterion for fully turbulent flow:

$$n^6 \sqrt{h\, |\boldsymbol{S}_f|} \geq 1.1 \times 10^{-13} \quad \text{with } h \text{ in meters}$$

in which n is the non-dimensional *Manning's roughness coefficient*.

For fully turbulent flows, according to Manning's equation in SI units (International System of Units), $\boldsymbol{u} = h^{\frac{2}{3}}\boldsymbol{S}_f^{\frac{1}{2}}/n$, the bed friction stress vector has the expression

$$\boldsymbol{\tau}_b = -\frac{\rho g n^2 \boldsymbol{u}\,|\boldsymbol{u}|}{h^{\frac{1}{3}}} \qquad \text{(in SI units)} \tag{2.16}$$

n's value is available in a number of references such as [22, 36, 7]. Equation (2.16) is sometimes also written in term of the Chezy coefficient $C = h^{\frac{1}{6}}/n$ as

$$\boldsymbol{\tau}_b = -\frac{\rho g \boldsymbol{u}\,|\boldsymbol{u}|}{C^2} \qquad \text{(in SI units)} \tag{2.17}$$

In case of not fully turbulent flow, $\boldsymbol{S}_f$ is linked with velocity and friction coefficient through Darcy-Weisbach equation, $\boldsymbol{u} = (8gh\boldsymbol{S}_f/f)^{\frac{1}{2}}$. The resulted expression of $\boldsymbol{\tau}_b$ is

$$\boldsymbol{\tau}_b = -\frac{\rho f \boldsymbol{u}\,|\boldsymbol{u}|}{8} \tag{2.18}$$

where the Darcy-Weisbach friction factor f could be calculated from equations presented by [22] and [52], or estimated through a *Moody diagram* presented by [23].

Groen *et al.* [46] presented another expression of bed friction stress by including the effect of wind stress,

$$\boldsymbol{\tau}_b = -\frac{\rho g \boldsymbol{u}\,|\boldsymbol{u}|}{C^2} - 0.05\,\boldsymbol{\tau}_w \tag{2.19}$$

Viscous and turbulent stresses Viscous and turbulent stresses are resisting stresses in flow due to flow viscosity and turbulence.

Viscous stress could be represented in SWE by a term

$$\tau_v = h\nu\nabla^2\boldsymbol{u} \tag{2.20}$$

But it is considered several orders of magnitude smaller than turbulent stress [128, 136, 131], as [128] indicates the ratio is about 10^{-4} to 10^{-8}, so is often neglected in practical computation.

The turbulent stress is also known as *Reynolds stress*. Due to the second law of thermodynamics, *"there is a tendency on the part of nature to proceed toward a state of greater disorder"* [150], when energy of parallel motion is converted into energy of less parallel motion in flow, essentially short-wave motion and turbulent motion, the process cannot be reversed [1]. This means the energy in parallel flow (or more precisely, potential flow) is lost due to turbulence effect, hence turbulence effect acts on a fluid element as a stress. To express turbulent stress in term of parallel flow quantities remains an unsolved problem [136], known as the *closure problem* of fluid dynamics. Boussinesq's closure hypothesis is a classical approximation leading to such an expression of turbulent stress [128]:

$$\tau_t = h\nu_t\nabla^2\mathbf{u} \tag{2.21}$$

ν_t is called turbulent viscosity (or eddy viscosity, apparent viscosity) coefficient analogous to the molecular viscosity coefficient ν. Unlike the molecular viscosity coefficient, ν_t is not decided solely by the fluid property but also by the state of turbulence

motion, it may vary significantly on both spatial and temporal dimension [79]. A review of the efforts on estimating ν_t can be found in [79]. For practical use in SWE, a depth-averaged ν_t is sought. [98] proposed a rough estimate of depth-averaged $\nu_t = 0.1$ m^2/s. However, [128] pointed out that in most SWE applications the turbulent viscosity term is either included in a bed friction term or totally neglected.

2.1.2 Flood modelling by SWE with uncertain parameters

Flood modelling with SWE has been practised by researchers with various parameterisations. Many of them notice and stress the uncertainties associated with some parameters of SWE, some of them treat the uncertain parameters in a probabilistic way.

A 2-D SWE model with nesting local grid refinement is applied in [152] to flood simulation in Kofu basin, Japan, with a complex land-cover. In this simulation, different inflow hydrograph is used, each associate with a probability. Two sets of values of Manning's n are applied, one takes the effect of vegetation and buildings into consideration, one does not. The simulation result shows the effect of n value on the accuracy of simulation is significant and enough attentions must be paid to the uncertainties of Manning's n in a practical flood modelling.

A flood model on the basis of 2-D SWE and a finite difference numerical scheme is applied on the Fuji river basin in central Japan [139]. The result indicates that the model can fully describe the transportation of flood wave in the temporal and spatial domain with satisfactory accuracy. The model is helpful not only in the flood risk management of river basin, but also in the study of real-time operations of rescue jobs and evacuation routes in a flood event.

Floods are modelled by [93] in a dense urban area of Nimes, France, using 2-D SWE. A sensitivity analysis is also made on uncertainties in the inflow hydrographs, bed friction coefficient and topographical data. The numerical results show a high standard deviation in the peak water depth and the authors stress on the importance of obtaining precise input hydrograph and bed friction coefficient for the accuracy of modelling.

A review of recent progress in the use of reduced complexity models with SWE for predicting floodplain inundation is given in [63]. In the part of model parameterisation the authors point out that all the three key data items, topographic data, bed friction coefficient and inflow hydrograph, are subject to considerable uncertainties.

Horritt [60] uses a second-order perturbation approach to investigate the effects of topographic uncertainty in a flood model on the basis of 1-dimensional non-inertia SWE. The topographic uncertainty is assumed to be of Gaussian distribution and its convariance function be of exponential type. An efficiency comparison of the perturbation approach and Monte Carlo method shows the former is favoured.

A sampling-based flood risk analysis for dike system is introduced in [30] with an inundation model using one-dimensional linear SWE. The analysis is done by a 5000 runs of the model each with a Monte Carlo sampling of the random inflow discharge.

A dam-break flood in an urban residential area in southern California is modelled in [37] with SWE. The model uses topographic data from a $1.5m$ resolution Digital Terrain Model, and a spatially distributed Manning's coefficient n based on a land-cover classification. A sensitivity analysis shows that high-resolution topographical

data and heterogeneity in Manning's coefficient n are important for the accuracy of the modelling.

Neal *et al.* [96] report a set-up and calibration of two 2-D SWE models based on digital elevation data with and without buildings. The validation data were collected in January 2005 after a major flood event in the city of Carlisle, UK, including distributed urban maximum water level and extent measurements with gauged hydrographs. The comparison of the two model shows the latter is more accurate due to blockages on the floodplain when building heights were included in the topography.

2.1.3 Spectral approximation

A spectral approach to approximate functions of random parameters was introduced by Wiener [137] and Chorin [20] where random variables were represented with an expansion of orthogonal Hermite polynomials in Gaussian random variables. The method was extended to utilise polynomials in other type of random variables by [142], these polynomials are termed generalised polynomial chaos. Ghanem and Spanos employed Galerkin approach to construct Hermite polynomial chaos representations of random processes and applied the technique to many engineering problems with success [42]. Reviews of techniques on probabilistic numerical analysis in term of finite element methods can be found in [87, 126, 70]. Generalised polynomial chaos were used to simulate fluid flow with random parameters in [140], [143], [133] and [132]. A recent review in this field can be found in [141].

2.2 Stochastic properties of uncertain parameters

Many parameters of SWE are subject to uncertainties due to the inherent randomness of natural processes and/or our incomplete knowledge on them. These uncertain parameters may include initial and boundary condition data, domain's topographical data, data and coefficients that determine the wind stress, bed friction coefficient such like Manning's coefficient, turbulent viscosity coefficient, etc. To incorporate uncertain parameters into the stochastic SWE, the stochastic properties of them are required. This section gives a discussion on the stochastic properties of the three parameters that are considered uncertain in this study, namely the inflow boundary condition (inflow hydrograph), the bed friction coefficient and the domain topography.

2.2.1 Flood hydrograph

The usually used *flood frequency analysis* on hydraulic engineering focuses on statistical analysis of flood peak discharge, however many design problem can only be solved by specifying design flood hydrograph. It was recognised that floods cannot be characterised by only peak volume, total volume and duration, different distribution of discharge over time may cause significant differences in flood behaviour and appropriate flood management policies [149, 23].

Flood hydrographs show distributions of river discharge over the time of flood (Figure 2.2 gives two examples), they are influenced by many random factors, such

as rainfall pattern and amount, watershed geomorphology, ground infiltration rate, vegetation of the watershed and temperature, etc.

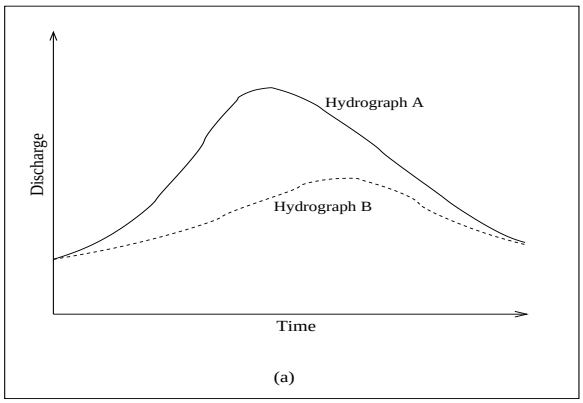

Figure 2.2: Examples of flood hydrograph

Most often it is a *excess rainfall* that causes a flood downstream. Excess rainfall, or effective rainfall, is the rainfall that is neither retained on the land surface nor infiltrated into the soil. After being gathered by the watershed surface flow, excess rainfall cause an extra discharge (with respect to the base flow), a *direct runoff* in the downstream river [23]. A direct runoff hydrograph (DRH) is usually obtained through a rainfall-runoff model. Singh [119] gave an extensive summary of rainfall-runoff models among which the *unit hydrograph* (UH) method is the one most widely used.

First proposed by Sherman [117], the unit hydrograph of a watershed is defined as a direct runoff hydrograph resulted by one unit depth (1 cm or 1 inch) of excess rainfall generated uniformly over the drainage area at a constant rate. Another similar concept, *Instantaneous unit hydrograph* (IUH) is defined as the hydrograph produced by a unit depth of uniform excess rainfall deposited instantaneously on the watershed, i.e. a hypothetical impulse of a unit excess rainfall. DRH caused by any amount of excess rainfall can be obtained by a convolution integral of UH or IUH [23]. In this process, the transformation of a rainfall to a run-off is assumed linear.

By modelling the watershed as a cascade of equal linear reservoirs and solving a series of differential equations simulating the flow among the reservoirs, Nash [95] derives such an expression of IUH

$$H(t) = \frac{1}{\Gamma(n)}(\frac{t}{k})^{n-1} \cdot \frac{e^{-t/k}}{k}$$

where $H(t)$ represents IUH, Γ is the Gamma function, n and k are two parameters decided by the watershed characteristics. Based on the recorded rainfall data and DRH of historical storm events, Bras [12] and Serrano *et al.* [116] estimate the values of n and k by the method of matching moments [23].

Yang *et al.* [144] assess the uncertainty associates with the parameters n and k of Nash's IUH using multi-storm analysis in the case that observed rainfall and DRH data of multiple storms are available. They sample m storms from the storm set in a way of bootstrap re-sampling, and estimate the n and k by minimising the total

squared error between the observed and computed IUH for m storms simultaneously. By repeating the procedure they obtain a population of estimated n and k from where their statistical properties are concluded. They find that the probability density of the parameter n of Lan-Yang watershed in Taiwan follows a shifted exponential distribution, while the probability density of k of the watershed is of Gaussian distribution, and correlation coefficient between n and k is -0.59. The uncertainty of the IUH is then estimated on the basis of the statistical properties of n and k by Rosenblueth point estimation method [112].

Since flow in Nash's linear reservoirs is modelled by differential equations, Sarino *et al.* [114] instead obtain stochastic properties of IUH by solving stochastic differential equations with parameters n and k. In the 14 realisations of IUH obtained by using the technique of matching moment on 14 pairs of recorded rainfall and DRH data of the Middle Thames River, Ontario, they find k is the one exhibiting the highest degree of uncertainty so assume n to be constant and take k as a random variable. The Chi-squared test, Kolmogorov-Smirnov and W test [48] are conducted to investigate the feasibility of candidate probability distributions of k, the Gaussian distribution is accepted as the one appropriate. Sarino *et al.* hence obtain explicit expression of the mean and variance of IUH. Hjelmfelt *et al.* [58] did a similar work. But Yang *et al.* [144] report that assuming n a constant causes inaccuracy in the estimation of IUH.

Yeh et al. [146] assume both n and k be of log-normal distribution and estimate their mean, variance and covariance from observed data through regional regression equations, as tabulated in table 2.2, and transmit the uncertainties of n and k to the resulted IUH by probabilistic point-estimate methods.

Regression	μ_n	σ_n	μ_k	σ_k	$Cov_{n,k}$
1	3.206	1.453	2.141	1.419	-0.557
2	3.206	1.453	2.141	1.419	-0.604
3	2.613	1.131	2.424	1.581	-0.622
4	2.931	1.282	2.424	1.581	-0.602

Table 2.2: Statistics of n and k for Tan-Shui watershed at Jei-Shou Bridge from different regression equations, from [146]

Another group of practitioners are not satisfied with conceptual models and go further toward physical details of watersheds. Rodriguez-Iturbe *et al.* [111] and Gupta *et al.* [47] develop the *geomorphologic instantaneous unit hydrograph* (GIUH) to estimate the IUH from watershed geomorphology. In this approach, excess rainfall is routed in different paths on overland areas and channels probabilistically and the IUH is interpreted as the probability density function (PDF) of the travel time that a unit rainfall, landing anywhere in the watershed, takes to reach the outlet where the hydrograph is to be modelled. The resulted IUH is expressed as:

$$H(t) = f(t) = \sum f_s(t)\ P(s) \tag{2.22}$$

where $H(t)$ represents IUH, $f(t)$ is the PDF of the time a unit rainfall takes to travel through the whole watershed to the outlet, $f_s(t)$ is the PDF of that travel time through the path s. $P(s)$ is the probability that a unit rainfall takes path s. This

method assumes that the travel time in each path is an independent random variable. In [47] $f_s(t)$ is assumed to be of a exponential type as below,

$$f_s(t) = ue^{-\lambda t}$$

with u the dynamic velocity of flood wave in the path s, $\lambda = u/(1-\delta)$, δ is the infiltrated percentage. Another expression of $f_s(t)$ in the form of a Gamma-type distribution is proposed in [67]. The probability $P(s)$ is obtained by an analysis of the geomorphological structure of the watershed. This method requires detailed geomorphological information of a watershed which could be obtained from a digital elevation model.

Other practitioners regard the rainfall-runoff process as a blackbox and use statistical methods to find out stochastic property of UH from historical records. Assuming that observed excess rainfall hyetograph (ERH) and DRH data of r storms are available, the convolution relationship between ERH , DRH and UH is [23]

$$\begin{bmatrix} \mathbf{q}_1 \\ \mathbf{q}_2 \\ \cdot \\ \cdot \\ \mathbf{q}_r \end{bmatrix} = \begin{bmatrix} \mathbf{p}_1 \\ \mathbf{p}_2 \\ \cdot \\ \cdot \\ \mathbf{p}_r \end{bmatrix} \cdot \boldsymbol{H} \tag{2.23}$$

where $\mathbf{q}_i$ and $\mathbf{p}_i$ are the DRH vector and the ERH matrix of the i-th storm respectively, $\boldsymbol{H}$ is the UH vector. Many methods have been developed to solve Equation (2.23) for $\boldsymbol{H}$. Some of them use data of a single storm, as summarised by Singh [119], others use data of multiple storms simultaneously, usually involving an optimisation technique such like least square estimation [89, 90, 153]. Zhao *et al.* [153] show two theorems supporting the use of multi-storm analysis rather than single storm ones.

Yue *et al.* [149] also use statistical methods but instead of expressing UH in a vector form they simulate UH by a function $H(t)$ as below,

$$H(t) = \frac{1}{B(a,b)} t^{a-1}(1-t)^{b-1} \quad , \quad t \in [0,1]$$

$$B(a,b) = \int_0^1 s^{a-1}(1-s)^{b-1} ds$$

where $B(a,b)$ is a Beta function with parameter a and b decided by hydrograph shape. To obtain the stochastic property of a and b, two variables for each hydrograph, namely shape mean S_m and shape variance S_v, are defined to describe hydrograph shape. A series of S_m and S_v are obtained from recorded historical flood hydrographs and Yue *et al.* [149] claim that both S_m and S_v are of log-normal distribution. They then obtain the stochastic properties of a and b through the relationships

$$a = \frac{S_m^2(1-S_m)}{S_v^2} - S_m$$

$$b = a(\frac{1}{S_m} - 1)$$

Flood hydrograph can also be obtained from discharge records which is derived from *rating curve* models by converting measured water levels to a flow [53, 54]. The uncertainty in the rating curve models is documented in [105] and the error in the discharge data in percentage can be as large as 20 percent [104].

2.2.2 Bed friction coefficient

Identification of a bed friction coefficient such as Manning's n for a flood domain is subject to a significant degree of uncertainty, as the coefficient is influenced by many uncertain factors like bed surface characteristics, vegetation type, vegetation submerge height etc.

Possible methods to estimate bed friction coefficients include checking tables of coefficients for different surface types [22, 36], visual estimation at site [7], Cowan's method of matching physical characteristics to photographs to establish a compound roughness coefficient [27, 2], and using established formulas such as Jarret's [65] or Limerinos's formula [82] for Manning's n.

Estimates obtained by different methods may diverge. Wohl [138] estimated the Manning's n of 5 rivers by 4 methods, i.e. visual estimation, Jarret's formula, Limerinos' formula and Cowan's method. Table 2.3 shows the divergence of the estimates.

Method	Proudre	Arun	Chayang	Fitzroy	Paran
Jarret	0.024	0.051	0.096	0.014	0.034
Limerinos	0.037	0.069	0.104	0.019	0.047
Visual	0.045	0.060	0.090	0.030	0.045
Cowan	0.050	0.060	0.070	0.030	0.050

Table 2.3: Estimates of the Manning's n of 5 rivers by 4 methods (from [138])

Johnson [68] made a trial to assess uncertainty associate with subjective estimations. Having 18 students to estimate the Manning's n for a stream, he found the estimates are uniformly distributed. The US Army Corps of Engineers did a similar study by asking a group of experienced engineers to estimate the value of Manning's n for 10 stream reaches according to the site photographs. The estimates were found to be of log-normal distribution with the coefficients of variation ranging from 0.2 to 0.35. In the literatures, probabilistic properties of the friction coefficient are often arbitrarily specified for the convenience of the study as reported in [68]. Some examples of Manning's n specification are tabulated in table 2.4.

Probability Distribution	Coefficient of variation	On basis of	Reference
Gaussian	0.1, 0.15	Arbitrariness	[19]
Gaussian	0.2, 0.053	Arbitrariness	[91]
Gaussian	0.01, 0.02	Arbitrariness	[61]
Triangular	0.08	Tests and statistics	[145]
Log-normal	0.2–0.35	Tests and statistics	[18]
Uniform	0.28, 0.18	Tests and statistics	[68]

Table 2.4: Uncertainty of Manning's n (partially from [68])

Calibration methods are used to identify friction coefficients in a model. In these methods friction coefficients are tuned to optimise the fit between model predictions

and observations. Wener *et al.* [135] try to calibrate distributed floodplain roughness values in a flood model based on SWE with gauged data of flood extents and stages. He finds the higher the floodplain roughness heterogeneity, i.e. the more spatial differentiations of roughness values according to different land uses, the lower the sensitivity of model performance to the roughness value. Horritt [59] also notices that and shows the applicability of calibration methods is limited to floodplain with uniform friction or friction with low degree of spatial heterogeneity.

2.2.3 Bed topography

One of the basic problems of conventional topographic statistics, e.g., the standard deviation of the surface elevation, is that they are sample-size dependent, i.e. their values are affected by the areal extent of the surface [80]. However, scale-independent topographic statistics might be obtained by fractal analysis [24] based on the concept of statistical self-similarity, i.e. statistics measured on a small scale resembles the one on a large scale (but differs in unit) [83], though there are debates over the extent to which the natural surface are truly fractal [113, 6].

Topography in grain-scale may be more suitably represented by a friction term in SWE models [31], but according to statistical self-similarity it might imply topographic statistics in larger scales. Kirchner *et al.* [71] and Nikora *et al.* [99] show that representing topography of gravel river-bed with Gaussian random field is reasonable. Gaussian random field is also used to model topographical elevations of soil-covered surface [28, 29].

A widely used landscape-scale topography data source is the digital elevation model (DEM). The errors of DEM data range over several orders of magnitude along different DEM sources. At the low end of the spectrum, satellite-based radar or optical systems with typical sample spacing of 30 to 100 meters produce elevation standard deviation ranging from 5 to 50 meters, while at the higher end, airborne lidar typically provides DEMs with sample spacing of 0.5 to 2 meters and elevation standard deviation ranging from 0.15 to 0.30 meter [92].

As for the probability distribution of the DEM errors, many researchers find that the errors follow Gaussian type distributions. Kornus *et al.* [74] analyse the accuracy of DEM generated by satellite-based stereo imaging, the elevation error histogram is of a slightly positive-shifted Gaussian type. Gonçalves *et al.* [44] conclude the same result. Hashemian *et al.* [50] analyse the accuracy of DEM of a 60km by 25km hilly area with elevation variation about 350 meters, the error distribution concluded is also of a zero-mean Gaussian type.

Horritt [60] establishes a stochastic model of 1-D shallow water flow over uncertain topography represented by Gaussian random field with exponential covariance function. He finds that Gaussian random field with larger correlation length makes larger perturbation to the model.

Gaussian random field is also an maximum-entropy estimate in the case only second-order statistics are available [66].

Chapter 3

The Stochastic Shallow Water Equations Model

This chapter describes the setup of the stochastic SWE model which is a combination of the SWE and a probabilistic description of the input parameters. It includes the introduction of the physical domain (the model of Toce river valley), the probabilistic settings of the uncertain parameters, the discretisation of the random fields, and the target measurements of the model.

3.1 Model of Toce river valley

The domain of simulation in this work is a reduced physical model (scale 1:100) of the Toce river valley made and managed by CESI (Centro Elettrotecnico Sperimentale Italiano) at its facilities in Milan, Italy, which has been extensively used for flood propagation experiments [129]. It is a 50m long mortar-made model of the valley with topographical features. Details of the model can be found in [123]. The topography data of the model was obtained through the CD-ROM accompanies the publication [129]. This data is then taken as the mean value of the random topography field in the simulation. A 15m long section in the upstream part of the model is taken as the simulation domain in this project, which corresponds to a river valley of 1500m long. Figure 3.1 shows the topography of the domain wherein the position of the three gauge points, $G_1 = (7.955, 6.993)$, $G_2 = (7.902, 4.714)$ and $G_3 = (7.868, 5.882)$ are indicated by the white marks.

In this simulation the hydrograph HY2 introduced in [129] is taken as the mean inflow hydrograph in this flood simulations, as shown in Figure 3.8. On the downstream boundary a transmissive condition is applied which assumes a constant velocity across the boundary. The Manning's roughness coefficient $n = 0.016$ suggested in [129] is taken as the mean value of the random field of n. An initial condition of zeros-depth-water is applied to the whole domain.

3.2 Settings of uncertain parameters

This section states the assumptions on the stochastic properties of the uncertain parameters, e.g. their probability distributions, standard deviations and spatial/temporal

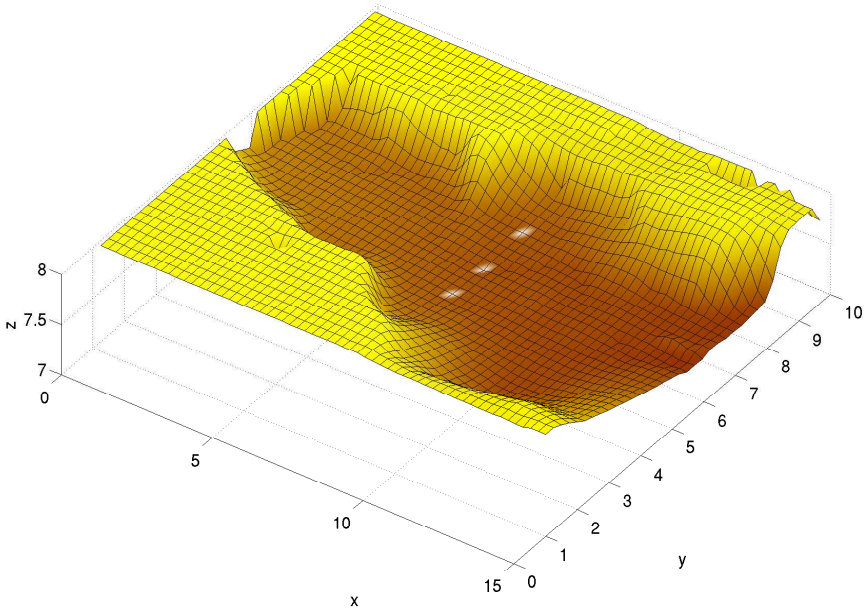

Figure 3.1: Domain of simulation: a 1500m section of Toce valley

correlations.

3.2.1 Topography

The topography data are subject to a random error due to imprecise measurements. The error was proposed to follow a zero-mean or slightly positive-shifted Gaussian type distribution [44, 50, 74]. It is assumed here in the simulation to be of a zero-mean truncated Gaussian distribution within the range $[-3\sigma_t, 3\sigma_t]$, as shown in Figure 3.2.

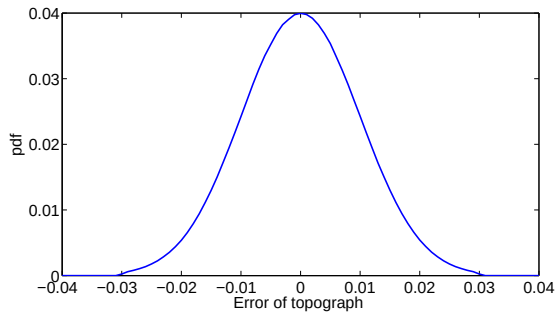

Figure 3.2: Probability density of the error of the topography

The standard deviation σ_t is assumed to be 0.01m (1m in the world of real scale). This is based on the findings in [92] that digital elevation models (DEM) of low precision have standard deviations in a range from 5 to 50 meters while for those of high precision the range is from 0.15 to 0.3 meter.

The spatial correlation of the error is assumed to be of an exponential square type, i.e., the covariance of the error at any two points $\boldsymbol{x}_1$ and $\boldsymbol{x}_2$ is

$$\mathrm{cov}(\boldsymbol{x}_1, \boldsymbol{x}_2) = \sigma_t^2 \exp(-\frac{r^2}{l^2})$$

where r is the distance between $\boldsymbol{x}_1$ and $\boldsymbol{x}_2$, l is the correlation length assumed to be 5m (500m in real scale).

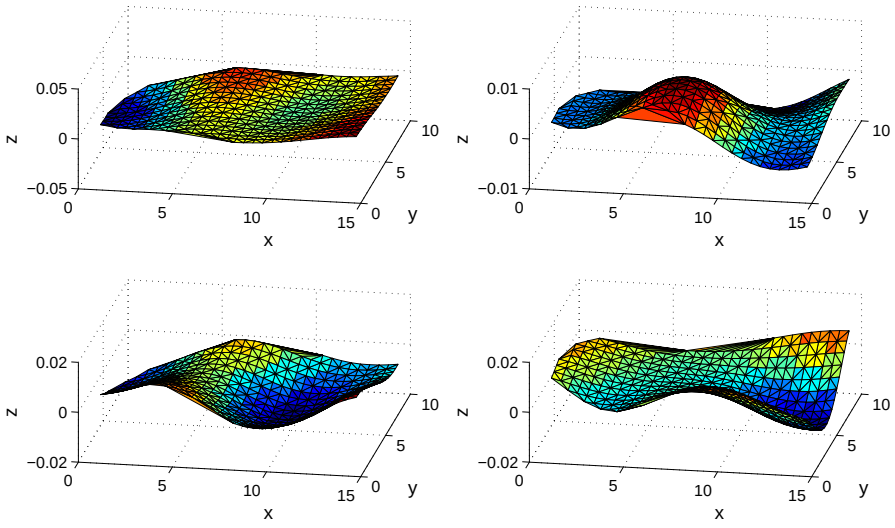

Figure 3.3: Four realisations of the random field of topography error

Figure 3.3 is a visualisation of 4 realisations of the random field of topography error. The realisations of random topography field are generated by perturbing the "mean topography" as shown in Figure 3.1 by this field of random error.

3.2.2 Manning's roughness coefficient

The Manning's roughness coefficient n values over the domain is assumed to be a log-normal random field on the basis of [18], with mean value $\mu_n = 0.016$ and standard deviation $\sigma_n = 0.002$. The former value is given in [129] and the latter is an assumption based on Figure 3.5 from [101]. It is further assumed that $\hat{n} = \log(n)$, a normal random variable, is confined within the range $[\mu_{\hat{n}} - 3\sigma_{\hat{n}}, \mu_{\hat{n}} + 3\sigma_{\hat{n}}]$ with $\mu_{\hat{n}}$ and $\sigma_{\hat{n}}$ the mean and standard deviation[1] of $\hat{n}$, which means n is confined within the range $[0.0109, 0.0231]$ as shown in Figure 3.4. It is also assumed $\hat{n}$ follows the same spatial correlation model as that for topography data with the same correlation length 5m. Figure 3.6 shows 4 realisations of the random field of Manning's n.

[1] $\mu_{\hat{n}} = -4.1429$ and $\sigma_{\hat{n}} = 0.1245$, corresponding to $\mu_n = 0.016$ and $\sigma_n = 0.002$

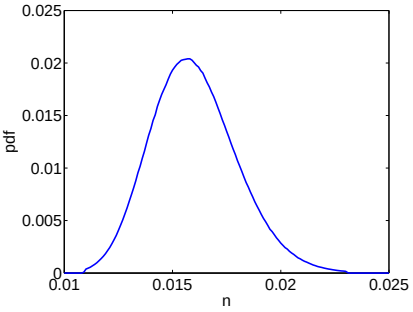

Figure 3.4: Probability density of Manning's n

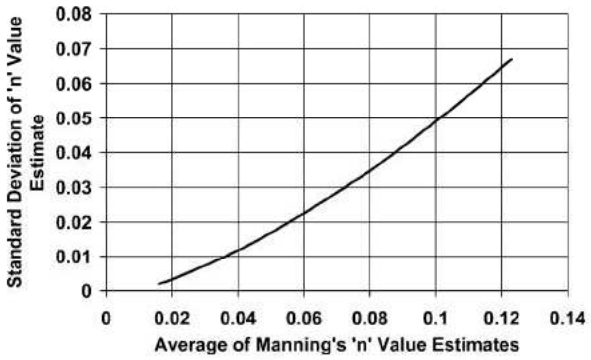

Figure 3.5: Uncertainty in estimates of Manning's n, from [101]

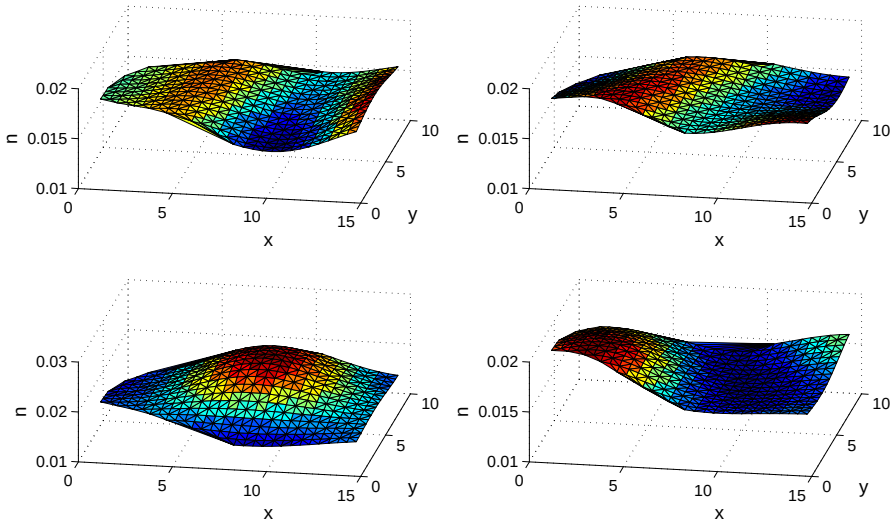

Figure 3.6: Four realisations of the random field of Manning's n

3.2.3 Inflow hydrograph

The inflow hydrograph in the Toce valley test case is a 120-second time series of discharge (corresponds to a 20 minutes discharge in real scale). It is assumed that this discharge is subject to truncated Gaussian random errors (values confined in $[-3\sigma_h, 3\sigma_h]$) as shown in Figure 3.7 due to imprecise measurement. The standard deviation σ_h is assumed $0.01\text{m}^3/\text{s}$ and the correlation length 40s. This random error plus the mean discharge gives the random inflow hydrograph for which Figure 3.8 shows 10 realisations.

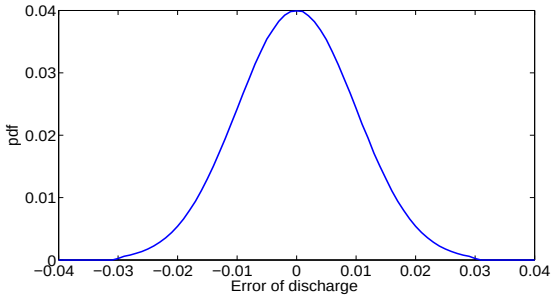

Figure 3.7: Probability density of the error of the discharge

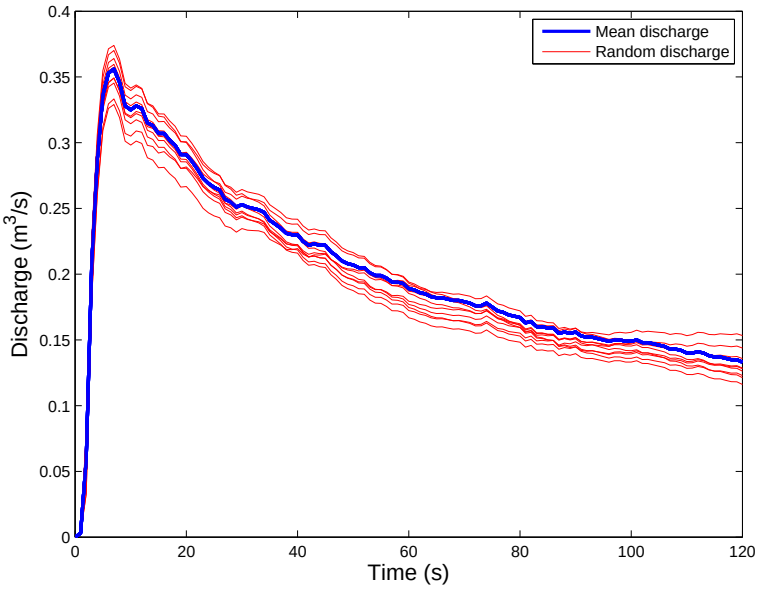

Figure 3.8: 10 realisations of the random random inflow hydrograph

3.3 Discretisation of random fields

For the purpose of numerical computation, the random fields of the uncertain parameters need to be represented in term of uncorrelated random variables. This is furnished by Karhunen-Loève expansions (KLE) [3].

Denoted by $\mathsf{r}(\boldsymbol{x},\omega)$ the random field with $\boldsymbol{x}\in\mathbf{D}$ and by $\mathsf{C}(\boldsymbol{x}_1,\boldsymbol{x}_2)$ its covariance function, the KLE representation of r is:

$$\mathsf{r}(\boldsymbol{x},\omega)=\mu_{\mathsf{r}}(\boldsymbol{x})+\sum_{i=1}^{\infty}\sqrt{\lambda_i}\,\theta_i(\omega)\phi_i(\boldsymbol{x}) \tag{3.1}$$

where $\mu_{\mathsf{r}}(\boldsymbol{x})$ is the mean of $r(\boldsymbol{x},\omega)$, $\{\theta_i(\omega)\}$ is a set of random variables. $\{\lambda_i\}$ and $\{\phi_i(\boldsymbol{x})\}$ are the eigenvalues and the eigenfunctions of $\mathsf{C}(\boldsymbol{x}_1,\boldsymbol{x}_2)$, i.e., they are the solutions of the Fredholm integral equation,

$$\int_{\mathbf{D}}\mathsf{C}(\boldsymbol{x}_1,\boldsymbol{x}_2)\phi_i(\boldsymbol{x}_1)\mathrm{d}\boldsymbol{x}_1=\lambda_i\phi_i(\boldsymbol{x}_2)\quad\forall\, i=1,2,\ldots \tag{3.2}$$

For practical computation the KLE needs to be truncated so that only a finite number of terms are retained. A KLE approximation of r with M terms is,

$$\hat{\mathsf{r}}(\boldsymbol{x},\omega)=\mu_{\mathsf{r}}(\boldsymbol{x})+\sum_{i=1}^{M}\sqrt{\lambda_i}\,\theta_i(\omega)\phi_i(\boldsymbol{x}) \tag{3.3}$$

Due to the symmetry and positive definiteness of the covariance function, its eigenvalues are real and its eigenfunctions form a complete orthogonal basis of $L^2(\mathbf{D})$ which is optimal in the sense that the mean square error (integrated over $\mathbf{D}$) caused by a truncation after the M-th term is minimised.

The random variable $\theta_i(\omega)$ can be expressed as

$$\theta_i(\omega)=\frac{1}{\sqrt{\lambda_i}}\int_{\mathbf{D}}(\mathsf{r}(\boldsymbol{x},\omega)-\mu_{\mathsf{r}}(\boldsymbol{x}))\phi_i(\boldsymbol{x})\mathrm{d}\boldsymbol{x}\quad\forall\, i=1,2,\ldots \tag{3.4}$$

$\theta_i(\omega)$ are mutually uncorrelated and centred with unit variance [3]. If the random field r is Gaussian, by (3.4) $\theta_i(\omega)$ are standard Gaussian random variables for which uncorrelatedness implies independence.

The Fredholm integral equation (3.2) can be solved by a finite element method, which leads to the system

$$\mathbf{C}\boldsymbol{\phi}_i=\lambda_i\boldsymbol{\phi}_i$$

where $\mathbf{C}$ is the $\mathcal{N}\times\mathcal{N}$ convariance matrix of the spatially discretised $\mathsf{r}(\boldsymbol{x},\cdot)$, $\mathcal{N}$ is the degree of freedom of the discretisation. λ_i and $\boldsymbol{\phi}_i$ are the eigenvalue and the eigenfunction of $\mathbf{C}$.

A KLE approximation of the spatially discretised r with M terms is

$$\hat{\mathbf{r}}(\omega)=\mu_{\mathbf{r}}+\sum_{i=1}^{M}\sqrt{\lambda_i}\,\theta_i(\omega)\boldsymbol{\phi}_i \tag{3.5}$$

For the stochastic SWE model, since all the three random fields are Gaussian, equation (3.5) transforms the random fields into representations in term of M independent standard Gaussian random variables. Making M takes the value 1, 2 and 3 respectively generates the representations of the three random fields totally in term of 3, 6 and 9 such Gaussian random variables, corresponding to 3-variate, 6-variate and 9-variate stochastic SWE models. E.g., if abbreviate a 9-variate stochastic SWE model as $\mathcal{U} = f(\boldsymbol{x}, t, \boldsymbol{\xi})$ with $\boldsymbol{\xi}$ a 9-element vector of standard Gaussian random variables, $\{\xi_i\}_{i=1}^{3}$, $\{\xi_i\}_{i=4}^{6}$ and $\{\xi_i\}_{i=7}^{9}$ are $\{\theta_i\}_{i=1}^{3}$ for the random field of topography, Manning's n and inflow hydrograph respectively.

3.4 Numerical SWE solver and target measurements

The numerical solver for SWE in the model is *Roe2d* [121]. The validation of *Roe2d* was extensively performed during the CADAM and IMPACT European research projects [129, 122]. The solver is run on a spatial discretisation of the domain shown in Figure 3.9.

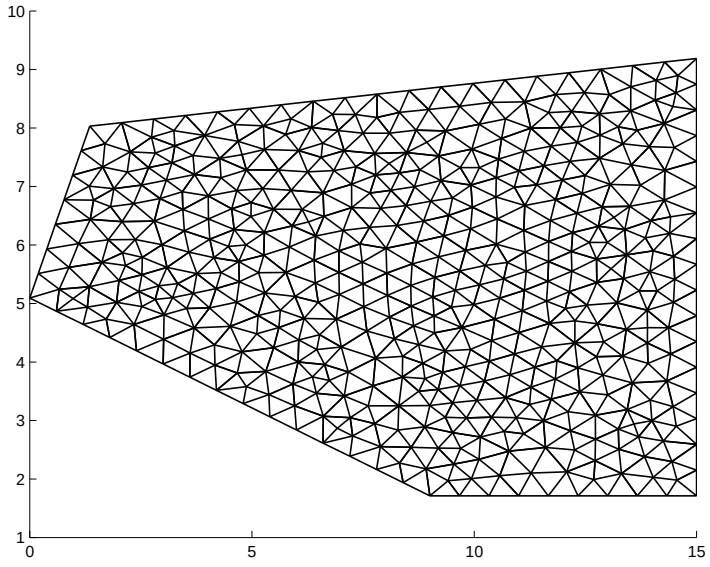

Figure 3.9: Spatial discretisation of the domain

An evaluation of the above described stochastic SWE model with a particular realisation of its input random variables brings a solution that describes the flood flow status, i.e. velocity $\boldsymbol{u}(\boldsymbol{x}, t)$ and water level $h(\boldsymbol{x}, t)$. In this work statistics of six measurements of water level, namely, $\{h_{\max}^{(i)}\}_{i=1}^{3}$, the maximum water level each at one of the three gauge points during the 120s period, and $\{h_{30}^{(i)}\}_{i=1}^{3}$, the three gauged water levels at the time 30th second, are estimated by numerical integrations as introduced in Chapter 4.

Chapter 4

Numerical Integration for Statistics

The stochastic SWE model with d random variables can be expressed as

$$\mathcal{U} = f(\boldsymbol{\xi}) \tag{4.1}$$

in which the spatial and temporal variables are omitted. $\boldsymbol{\xi} \in \Theta = [-\infty, \infty]^d$ is a d-element vector of standard Gaussian random variables with a probability measure $\rho(\boldsymbol{\xi})$. The aim in this chapter is to estimate $\Psi(\mathcal{U})$, a statistics of $\mathcal{U}$ that is described in Section 4.1, by an integration over the domain Θ,

$$\begin{aligned} I[\Psi(\mathcal{U})] =& I[\Psi(f(\boldsymbol{\xi}))] \\ =& \int_{\Theta} \Psi(f(\boldsymbol{\xi}))\rho(\boldsymbol{\xi})\mathrm{d}\boldsymbol{\xi} \end{aligned} \tag{4.2}$$

One approach for this multivariate integration problem is the cubature rules, analogous to most univariate integration rules, designed on the basis of multi-variate polynomial interpolation so that all multivariate polynomials of up to a certain degree can be integrated exactly. An extensive summary of the theoretical and practical aspects of the subject and a large collection of available cubature rules can be found in [125] and to which [25] is a later complement. For a give dimension, a cubature rule has a fixed number of abscissas. This makes the accuracy of the integration can not be systematically refined. In [115] the refining is done through a domain splitting so that cubature rules are applied on each rectangular sub-domain. However, this seems not viable for non-bounded domain or for integrations with non-uniform weight functions.

Another classical approach is the so called *product rule* which is a tensor product of 1-D N-point quadrature rules. The number of function evaluations for it is N^d. If the 1-D quadrature rules has a convergence rate $\mathcal{O}(N^{-a})$, the rate of the corresponding product rule is $\mathcal{O}(N^{-a/d})$. Due to the exponential growth of the effort along increasing number of dimensions to achieve a certain accuracy, the application of product rules on high dimensional problems is impractical. This phenomena has been termed "curse of dimension".

The "curse of dimension" can be broken to some extent on smooth integrands by sparse grid methods (also known as Smolyak methods). One class of these methods is the sparse grid quadrature. A method of this class is a linear combination of tensor products of 1-D quadrature rules which are based on global polynomial interpolation. Another class is the sparse grid finite element methods which approximate

the object function by sparse grid piecewise polynomials. These approximations may also facilitate integration if the polynomial approximation are much cheaper to evaluate than the original function. Among many others in the former class sparse grid Gauss-Hermite quadrature is constructed on the basis of 1-D Gauss-Hermite quadrature which is usually chosen for the integration of functions with Gaussian variables. In the latter class, sparse grid linear finite element method uses hierarchical linear basis functions so demand a quite low regularity of the function. Both the two methods have much better convergence rate than the product rules on high dimensional problems if the integrands possess a certain degree of regularity.

Two common approaches on multivariate integrations are Monte Carlo method and quasi-Monte Carlo method, using pseudo-random number sequence and quasi-random number sequence (also known as low-discrepancy sequence) respectively to generate samples. Monte Carlo method has a convergence rate of order $\mathcal{O}(N^{-1/2})$ which is slow but dimension-independent. Quasi-Monte Carlo method persues uniformity of samples and has a better convergence rate if the integrand is of bounded total variation, but the advantage tends to deteriorate along increasing number of dimensions.

Two novel numerical integration techniques, uncorrelated dimensions (UD) quadrature and compound uncorrelated dimensions (CUD) quadrature, are originally developped in this work. These quadratures sample the integrand on abscissas that are uniform on each dimension and minimise the correlation of the contributions to the integrands from each pair of dimensions. On integrands that can be expressed in multilinear functionals of any integrable functions, UD quadrature has a convergence rate of order $\mathcal{O}(N^{-1})$ if the integrand is of bounded variation, CUD quadrature has a convergence rate of order $\mathcal{O}(N^{-2})$ if the integrand belongs to C^2 space. Both the two rates are independent of the number of dimensions.

Five methods are chosen to integrate the model, they are sparse grid Gauss-Hermite quadrature, sparse grid linear finite element method, Monte Carlo and quasi-Monte Carlo quadratures, and UD quadrature.

4.1 Target statistics and reference results

The target statistics Ψ in this work are the mean, the variance and the exceedance probabilities of the measurements. If h denotes anyone of the six target measurements introduced in Section 3.4, due to equation (4.1) it can also be expressed as a function $h(\boldsymbol{\xi})$. Its mean μ_h and variance σ_h^2 are defined as,

$$\mu_h = \int_\Theta h(\boldsymbol{\xi})\rho(\boldsymbol{\xi})\mathrm{d}\boldsymbol{\xi}, \quad \sigma_h^2 = \int_\Theta (h(\boldsymbol{\xi}) - \mu_h)^2\rho(\boldsymbol{\xi})\mathrm{d}\boldsymbol{\xi}$$

The probability of exceedance $P_{h,1}$, $P_{h,2}$ and $P_{h,3}$ are defined as

$$P_{h,k} = \int_\Theta \mathscr{C}_k[h(\boldsymbol{\xi})]\rho(\boldsymbol{\xi})\mathrm{d}\boldsymbol{\xi}, \quad k = 1, 2, 3$$

where $\mathscr{C}_k[h]$ is an indicator function

$$\mathscr{C}_k[h] = \begin{cases} 1 & \text{if } h > \mu_h + k\sigma_h \\ 0 & \text{otherwise} \end{cases}$$

The above statistics for each of the six measurements are to be estimated by numerical integrations.

The reference results against which the errors of the estimations are evaluated are obtained by a QMC quadrature with 1.5×10^6 samples. Denoting the reference result of the statistics Ψ by $R(\Psi)$, its error is

$$\mathscr{E}_R(\Psi) = |R(\Psi) - \mathbb{E}(\Psi)|$$

If $Q(\Psi)$ denotes an estimation of Ψ by a numerical quadrature, the *true* error of $Q(\Psi)$ is

$$\mathscr{E}_Q(\Psi) = |Q(\Psi) - \mathbb{E}(\Psi)|$$

Since $\mathbb{E}(\Psi)$ is not known, by replacing it by $R(\Psi)$ in the above equation, an estimate of $\mathscr{E}_Q(\Psi)$ is obtained which is used in the efficiency comparison of the quadratures,

$$\widehat{\mathscr{E}_Q}(\Psi) = |Q(\Psi) - R(\Psi)|$$

The normalised error of this error estimation is defined as

$$\mathcal{E}_Q(\Psi) = \frac{|\widehat{\mathscr{E}_Q}(\Psi) - \mathscr{E}_Q(\Psi)|}{\widehat{\mathscr{E}_Q}(\Psi)} = \frac{\mathscr{E}_R(\Psi)}{\widehat{\mathscr{E}_Q}(\Psi)}$$

By assuming the stochastic SWE model is of bounded total variation, $\mathcal{E}_Q(\Psi)$ for a QMC quadrature can be bounded by the Koksma-Hlawka inequality [16] (which is introduced in detail in Section 4.4.2) in the following way. Since the QMC integrations in this work are all with number of sample points no more than 3×10^4, their $\mathscr{E}_Q(\Psi)$ are at least by one and a half order larger than $\mathscr{E}_R(\Psi)$. Taking into account that $\widehat{\mathscr{E}_Q}(\Psi) \geq \mathscr{E}_Q(\Psi) - \mathscr{E}_R(\Psi)$, one has

$$\mathcal{E}_Q(\Psi) < 10^{-1} \tag{4.3}$$

for QMC quadratures. For other numerical integration techniques in this work, because in the numerical results they have $\widehat{\mathscr{E}_Q}(\Psi)$ at best of the same order of the $\widehat{\mathscr{E}_Q}(\Psi)$ for QMC quadratures, the bound in equation (4.3) also applies. This shows the reference result $R(\Psi)$ is valid for the efficiency comparison.

4.2 Sparse grid Gauss-Hermite quadrature

Sparse grid Gauss-Hermite (SGH) quadrature [120, 100] is a linear combination of tensor products of 1-D Gauss-Hermite quadrature rules.

4.2.1 Formulation of the method

Suppose $\{x_n^N\}_{n=1}^N \in \Theta$ are the abscissas of a N-order 1-D Gauss-Hermite quadrature $\mathrm{Q}_N^{\mathcal{G}}$, and $\{w_n^N\}_{n=1}^N$ are the weights,

$$\mathrm{Q}_N^{\mathcal{G}}[f] = \sum_{n=1}^{N} w_n^N f(x_n^N)$$

Let $\boldsymbol{i} = (i_1, \cdots, i_d) \in \mathbb{N}^d$, a tensor product Gauss-Hermite quadrature rules is

$$(\mathrm{Q}_{i_1}^{\mathcal{G}} \otimes \cdots \otimes \mathrm{Q}_{i_d}^{\mathcal{G}})[f] = \sum_{j_1=1}^{i_1} \cdots \sum_{j_1=1}^{i_1} (w_{j_1}^{i_1} \cdots w_{j_d}^{i_d}) \cdot f(x_{j_1}^{i_1}, \cdots, x_{j_d}^{i_d})$$

which has a poor rate of convergence if d is large. A sparse grid quadrature is a linear combination of tensor product rules with relatively low total order $|\boldsymbol{i}|_1$. A d-dimensional q-level sparse grid Gauss-Hermite Quadrature is defined as

$$\mathrm{Q}_{q,d}^{\mathcal{SG}} = \sum_{q \le |\boldsymbol{i}|_1 \le q+d-1} (-1)^{q+d-1-|\boldsymbol{i}|_1} \cdot \begin{pmatrix} d-1 \\ q+d-1-|\boldsymbol{i}|_1 \end{pmatrix} \cdot (\mathrm{Q}_{i_1}^{\mathcal{G}} \otimes \cdots \otimes \mathrm{Q}_{i_d}^{\mathcal{G}})$$

with $q \ge 1$. Let

$$F^r(\Theta) = \{f : \Theta \to \mathbb{R} : D^\beta f \text{ continuous}, |\beta|_\infty \le r\}$$

define the space of all functions with continuous mixed derivative up to order r. The error of $\mathrm{Q}_{q,d}^{\mathcal{SG}}$ is of order $N^{-r}(\log N)^{(d-1)(r+1)}$ for integrands $f \in F^r$ [120, 100].

4.2.2 Numerical results on the model

The SGH quadrature abscissas and weights from [76] are used for the numerical integration of the stochastic SWE model. Only integrations for the mean values are implemented. The average error of these integrations are graphed in Figure 4.2, 4.3 and 4.4. The average is made over the three gauge points.

The result shows the error is not converging. This is due to that SGH quadrature's convergence is based on the assumption that the integrand has at least a global continuity, while the model under study seems very irregular. As an example Figure 4.1 shows $h_{30}^{(2)}$, the water level at G_2 on the 30th second, as an univariate function of ξ_1 by making ξ_2-ξ_9 fixed (for the meaning of ξ_i see the end of section 3.3). This irregularity in the water level might be made by the run-time adaptation of the temporal discretisation by the numerical solver to keep the Courant number below unity.

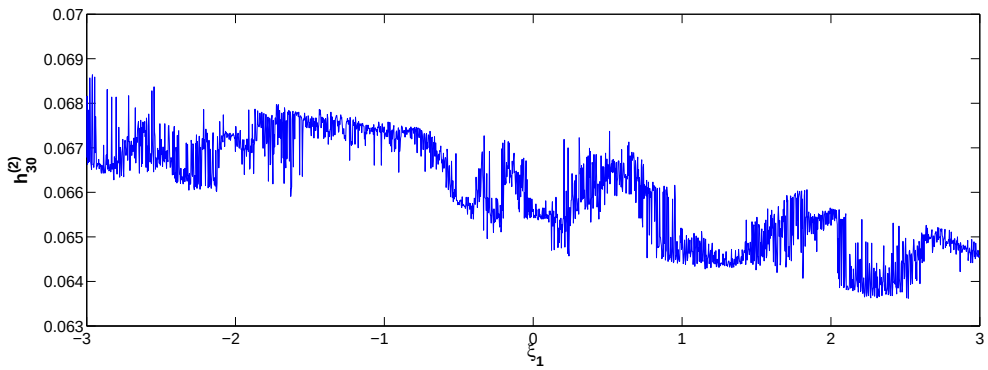

Figure 4.1: Water level $h_{30}^{(2)}$ as a function of ξ_1

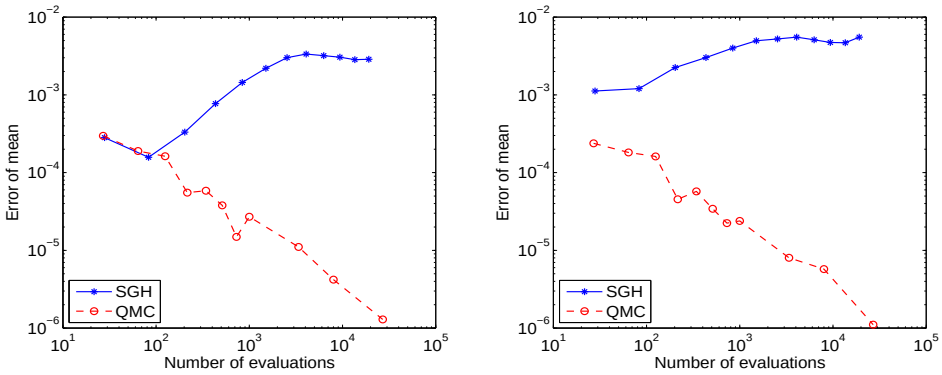

Figure 4.2: Average error of $\mu_{h_{\max}}$ (left) and $\mu_{h_{30}}$ (right), with $d = 3$

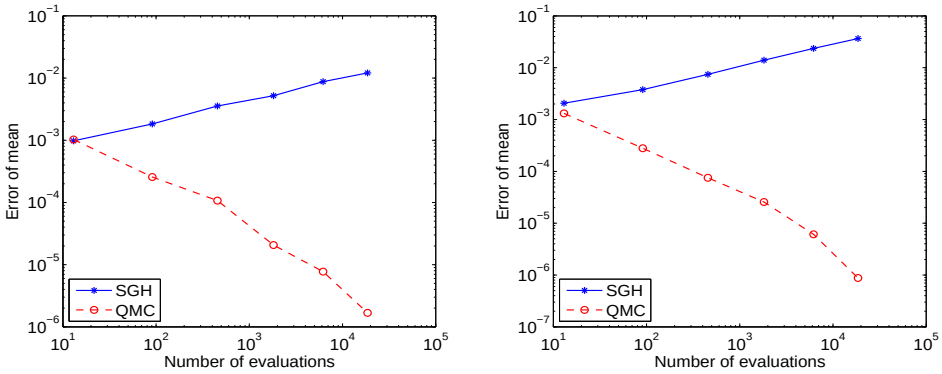

Figure 4.3: Average error of $\mu_{h_{\max}}$ (left) and $\mu_{h_{30}}$ (right), with $d = 6$

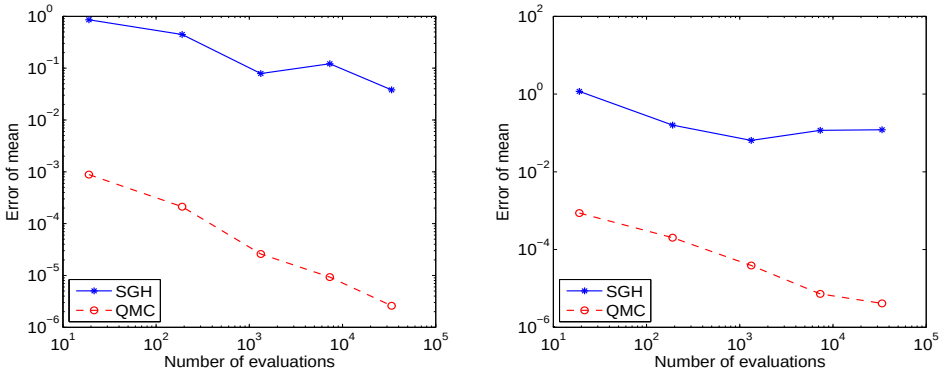

Figure 4.4: Average error of $\mu_{h_{\max}}$ (left) and $\mu_{h_{30}}$ (right), with $d = 9$

4.3 Sparse grid linear finite element method

Sparse grid linear finite element method (SLFEM) [151] is a sparse grid approximation method based on multi-dimensional hierarchical linear basis, which is derived from a 1-D hierarchical linear basis by a special way of tensor product construction. If the object function has bounded second mixed derivatives the approximation error is of order $\mathcal{O}(N^{-2}(\log N)^{3(d-1)})$, N is the number of evaluations.

4.3.1 Full tensor product grids

On domain $\Omega = [0,1]^d$, consider the family of d-dimensional standard rectangular grid $\{\Omega_{\boldsymbol{l}} : \boldsymbol{l} \in \mathbb{N}_0^d\}$, with mesh size

$$h_{\boldsymbol{l}} = (h_{l_1}, \ldots, h_{l_d}) = 2^{-\boldsymbol{l}}$$

the grid points $\boldsymbol{x}_{\boldsymbol{l},\boldsymbol{i}}$ of grid $\Omega_{\boldsymbol{l}}$ are the points

$$\boldsymbol{x}_{\boldsymbol{l},\boldsymbol{i}} = (x_{l_1,i_1}, \ldots, x_{l_d,i_d}) = \boldsymbol{i} \cdot \boldsymbol{h}_{\boldsymbol{l}}$$

Define the 1-D standard hat function

$$\phi_{l_j,i_j}(x_j) = \begin{cases} 1 - |\frac{x_j - i_j \cdot h_{l_j}}{h_{l_j}}| & \text{if } x_j \in [x_{l_j,i_j} - h_{l_j}, x_{l_j,i_j} + h_{l_j}] \\ 0 & \text{otherwise} \end{cases}$$

and the d-dimensional linear basis function on each grid point $\boldsymbol{x}_{\boldsymbol{l},\boldsymbol{i}}$

$$\phi_{\boldsymbol{l},\boldsymbol{i}}(x) = \prod_{j=1}^{d} \phi_{l_j,i_j}(x_j)$$

then the space of piecewise d-dimensional linear functions on $\Omega_{\boldsymbol{l}}$ is

$$V_{\boldsymbol{l}} = \text{span}\{\phi_{\boldsymbol{l},\boldsymbol{i}} : 0 \leq \boldsymbol{i} \leq 2^{\boldsymbol{l}}\}$$

While by defining an index set

$$\mathcal{B}_{\boldsymbol{l}} = \left\{ \begin{array}{llll} i_j = 1, \ldots, 2^{l_j} - 1, & i_j \text{ odd}, & j = 1, \cdots, d, & \text{if } l_j > 0 \\ i_j = 0, 1 & & j = 1, \cdots, d, & \text{if } l_j = 0 \end{array} \right\}$$

the hierarchical difference spaces are

$$W_{\boldsymbol{l}} = \text{span}\{\phi_{\boldsymbol{l},\boldsymbol{i}} : \boldsymbol{i} \in \mathcal{B}_{\boldsymbol{l}}\}$$

Given an integer $n \geq 0$, V_n can be expressed as a direct sum of subspaces $W_{\boldsymbol{l}}$,

$$V_n = \bigoplus_{l_1=0}^{n} \cdots \bigoplus_{l_d=0}^{n} W_{\boldsymbol{l}} = \bigoplus_{|\boldsymbol{l}|_\infty \leq n} W_{\boldsymbol{l}}$$

The family of functions

$$\{\phi_{\boldsymbol{l},\boldsymbol{i}} : \boldsymbol{i} \in \mathcal{B}_{\boldsymbol{l}}\}$$

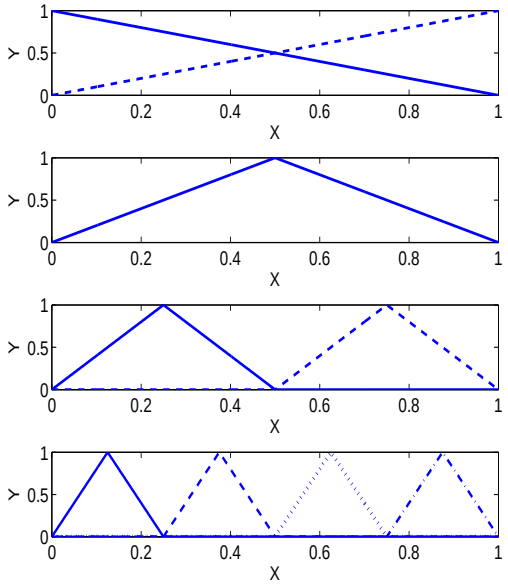

Figure 4.5: 1-D hierarchical basis functions for V_3, level 0 (top) to level 3 (bottom)

is the hierarchical basis [147, 148] of V_n. Figure 4.5 shows 1-D such basis functions for V_3.

V_n is the space of full tensor product grids approximation functions. Each function $f \in V_n$ can be represented as

$$f(\boldsymbol{x}) = \sum_{|\boldsymbol{l}|_\infty \leq n} \sum_{\boldsymbol{i} \in \mathcal{B}_{\boldsymbol{l}}} \alpha_{\boldsymbol{l},\boldsymbol{i}} \cdot \phi_{\boldsymbol{l},\boldsymbol{i}}$$

where $\alpha_{\boldsymbol{l},\boldsymbol{i}}$ are the coefficients of the hierarchical tensor product basis, also known as *hierarchical surplus*. They scale the basis functions to what has to be added to the linear approximation of level $l-1$, to obtain the one of level l. In 1-D cases,

$$\alpha_{l,i} = \begin{cases} f(x_{l,i}) - \frac{1}{2}(f(x_{l,i-1}) + f(x_{l,i+1})) & \text{if } l \geq 1 \\ f(x_{l,i}) & \text{if } l = 0 \end{cases}$$

On defining a function operator $\mathcal{S}$

$$\mathcal{S} = \begin{cases} \begin{bmatrix} -\frac{1}{2} & 1 & -\frac{1}{2} \end{bmatrix}_{l,i} & \text{if } l \geq 1 \\ 1_{l,i} & \text{if } l = 0 \end{cases}$$

$\alpha_{l,i}$ can also be written as

$$\alpha_{l,i} = \mathcal{S} f$$

and a d-dimensional $\alpha_{\boldsymbol{l},\boldsymbol{i}}$ can be expressed in the following operator form

$$\alpha_{\boldsymbol{l},\boldsymbol{i}} = \left(\bigotimes_{t=1}^{d} \mathcal{S}_t \right) f$$

For example, in a 2-D case, if none of the elements of $\boldsymbol{l}$ is zero, $\alpha_{\boldsymbol{l},\boldsymbol{i}}$ has the form

$$\alpha_{\boldsymbol{l},\boldsymbol{i}} = \begin{bmatrix} \frac{1}{4} & -\frac{1}{2} & \frac{1}{4} \\ -\frac{1}{2} & 1 & -\frac{1}{2} \\ \frac{1}{4} & -\frac{1}{2} & \frac{1}{4} \end{bmatrix}_{\boldsymbol{l},\boldsymbol{i}} f$$

if one of the elements of $\boldsymbol{l}$ is zero, $\alpha_{\boldsymbol{l},\boldsymbol{i}}$ has the form

$$\alpha_{\boldsymbol{l},\boldsymbol{i}} = \begin{bmatrix} -\frac{1}{2} & 1 & -\frac{1}{2} \end{bmatrix}_{\boldsymbol{l},\boldsymbol{i}} f$$

and if all of the two elements of $\boldsymbol{l}$ are zero, $\alpha_{\boldsymbol{l},\boldsymbol{i}}$ is just $f_{\boldsymbol{l},\boldsymbol{i}}$ itself.

4.3.2 Sparse grids

The complexity of the full tensor grid space V_n increases exponentially with d. To alleviate this curse of dimension, [45, 151] introduce the *sparse grids* space $V_n^s \in V_n$ as

$$V_n^s = \bigoplus_{|\boldsymbol{l}|_1 \leq n} W_{\boldsymbol{l}}$$

every function $f \in V_n^s$ can now be represented as

$$f_n^s(\boldsymbol{x}) = \sum_{|\boldsymbol{l}|_1 \leq n} \sum_{\boldsymbol{i} \in \mathcal{B}_{\boldsymbol{l}}} \alpha_{\boldsymbol{l},\boldsymbol{i}} \cdot \phi_{\boldsymbol{l},\boldsymbol{i}}$$

Let

$$H^{q,r}(\Omega) = \{f : \Omega \to \mathbb{R} : D^\beta f \in L_q(\Omega), |\beta|_\infty \leq r\}$$

$$H_0^{q,r}(\Omega) = \{f \in H^{q,r} : f|_{\partial\Omega} = 0\}$$

defines the space of all functions with bounded (with respect to L_q norm) mixed derivative up to order r, and the subspace of $H^{q,r}$ consisting of functions $f \in H^{q,r}$ that vanish on the boundary. [14] shows that for $f \in H_0^{q,2}$, a n-level sparse grid approximation f_n^s of f has the interpolation error

$$||f - f_n^s||_2 = \mathcal{O}(h_n^2 (\log h_n^{-1})^{d-1})$$

and the number of function evaluations N is of order $\mathcal{O}(h_n^{-1}(\log h_n)^{d-1})$. It turns out the interpolation error in term of N is of order $\mathcal{O}(N^{-2}(\log N)^{3(d-1)})$. This result also holds for $f \in H^{q,2}$ [38].

Figure 4.3.2 display the difference of 2-D V_3^s and V_3 . The hierarchical subspaces $W_{\boldsymbol{l}}$ included by V_3^s are depicted in black colour, while those not included by V_3^s but included by V_3 are depicted in grey colour.

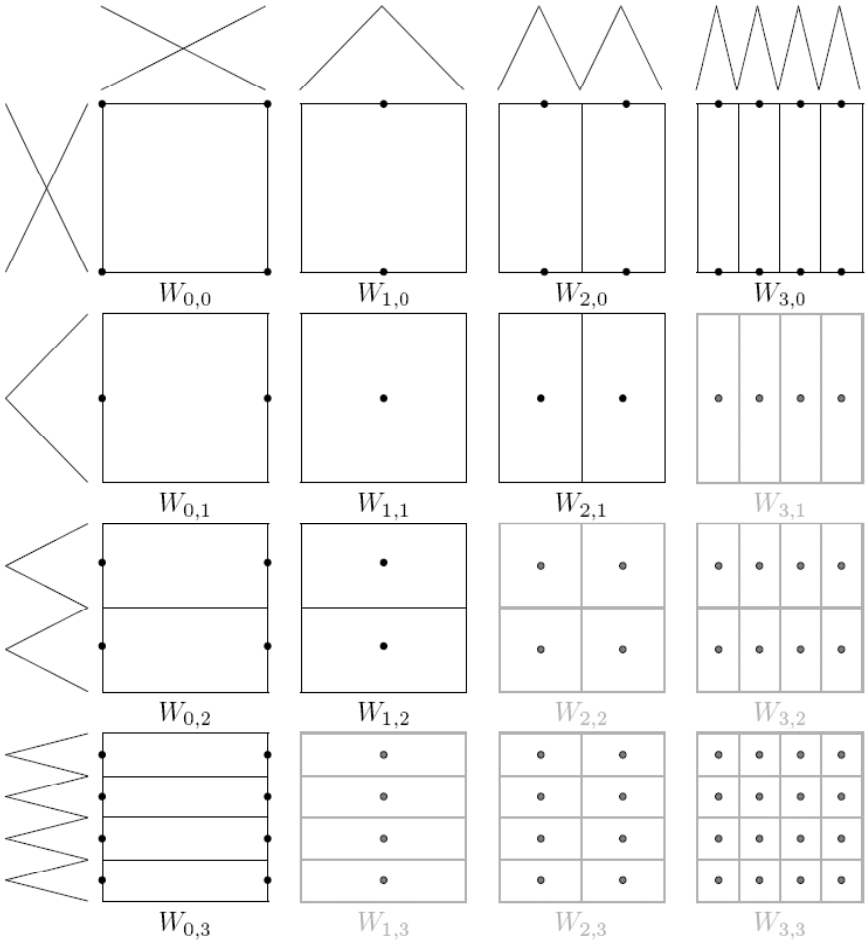

Figure 4.6: Supports of 2-D basis functions of hierarchical subspaces $W_{\boldsymbol{l}}$ of space V_3^s (in black colour) and of space V_3 (in black and in grey colours), from [38].

4.3.3 Linear basis functions for Gaussian domain

The above introduced sparse grid method has its basis functions defined on a finite domain $\Omega = [0,1]^d$. In this section two types of linear basis functions on infinite Gaussian domain $\Theta = [-\infty, \infty]^d$ are defined. One type adopts the standard hat function on a equally distanced grid within the range $[-4, 4]$ and linear extrapolations outside the range, the other type is equal to the conventional procedure of mapping Θ to $[0,1]^d$ and applying the standard SLFEM. The 1-D forms of the two types are given below.

4.3.3.1 Basis functions of type I

Consider a grid defined within $[-4, 4]$ with mesh size $h_l = 8/2^l$, the grid points are $\{x_{l,i} = -4 + i \cdot h_l\}$, with

$$i = \begin{cases} 0, 1 & \text{if } l = 0 \\ 1, \cdots, 2^l - 1, \ i \text{ odd}, & \text{if } l > 0 \end{cases}$$

The basis functions $\psi_{l,i}(x)$ on domain $[-\infty, \infty]$ are defined as below.

For $l = 0$,

$$\psi_{0,0}(x) = \frac{x - x_{0,0}}{h_0} = \frac{x+4}{8}$$

$$\psi_{0,1}(x) = \frac{x_{0,1} - x}{h_0} = \frac{4-x}{8}$$

For $l \geq 1$, standard hat basis function $\psi_{l,i}$ are defined with $1 < i < 2^l - 1$, i odd,

$$\psi_{l,i}(x) = \begin{cases} 1 - |\frac{x - x_{l,i}}{h_l}| & \text{if } x \in [x_{l,i} - h_l, \ x_{l,i} + h_l] \\ 0 & \text{otherwise} \end{cases}$$

and the basis function on the two boundary points, $\psi_{l,1}$ and $\psi_{l,2^l-1}$ are

$$\psi_{l,1}(x) = \begin{cases} 1 - |\frac{x - x_{l,1}}{h_l}| & \text{if } x \in [x_{l,1} - h_l, \ x_{l,1} + h_l] \\ 1 - \frac{x - x_{l,1}}{h_l} & \text{if } x < x_{l,1} - h_l \\ 0 & \text{otherwise} \end{cases}$$

$$\psi_{l,2^l-1}(x) = \begin{cases} 1 - |x - x_{l,2^l-1}|/h_l & \text{if } x \in [x_{l,2^l-1} - h_l, \ x_{l,2^l-1} + h_l] \\ 1 - (x - x_{l,2^l-1})/h_l & \text{if } x > x_{l,2^l-1} + h_l \\ 0 & \text{otherwise} \end{cases}$$

By increasing the level l, $\psi_{l,i}(x)$ defined above facilitates finer linear interpolation within the range $[-4, 4]$. The approximation outside the range is done by extrapolations from the basis function on the boundary of the grid. These basis functions of level 0 to 3 on the partial domain $[-5, 5]$ are graphed in the left column of Figure 4.7.

4.3.3.2 Basis functions of type II

Consider a grid defined within $[0,1]$ with mesh size $h'_l = 2^{-l},\ \ l \geq 1$, the grid points are $\{x'_{l,i} = i \cdot h_l,\ :\ i = 1, \ldots, 2^l - 1,\ i \text{ odd}\}$. Then map the $x'_{l,i} \in [0,1]$ to $x_{l,i} \in [-\infty, \infty]$ by Φ^{-1}, the inverse standard normal cumulative distribution function,

$$x_{l,i} = \Phi^{-1}(x'_{l,i})$$

and define

$$h^+_{l,i} = \Phi^{-1}(x'_{l,i} + h'_l) - \Phi^{-1}(x'_{l,i})$$

$$h^-_{l,i} = \Phi^{-1}(x'_{l,i}) - \Phi^{-1}(x'_{l,i} - h'_l)$$

The basis functions $\psi_{l,i}(x)$ with $x \in [-\infty, \infty]$ are defined as below. For $l \geq 1$,

$$\psi_{l,i}(x) = \begin{cases} 1 - |\frac{x - x_{l,i}}{h^-_{l,i}}| & \text{if } x \in [x_{l,i} - h^-_{l,i},\ \ x_{l,i}] \\ 1 - |\frac{x - x_{l,i}}{h^+_{l,i}}| & \text{if } x \in [x_{l,i},\ \ x_{l,i} + h^+_{l,i}] \\ 0 & \text{otherwise} \end{cases}$$

with $1 < i < 2^l - 1$, i odd.

Of this type there are no basis functions of level zero since one is not going to evaluate at the boundary $-\infty$ and ∞. $\psi_{l,i}$ is a non-symmetric hat function. In the two ends of the domain it turns out to be constant due to the infinite $h^-_{l,i}$ or $h^+_{l,i}$. Basis functions of level 1 to 4 of this type on the partial domain $[-2, 2]$ are also graphed in the right column of Figure 4.7.

4.3.4 Numerical results on the model

The SLFEM with basis function type I and type II are applied on the stochastic SWE model with 3, 6 and 9 random variables respectively for linear approximations. Target statistics are then estimated by numerical integrations of the approximations with 10^6 quasi-Monte Carlo (QMC) samples. The average errors of these estimations along the number of evaluations are displayed in Figure 4.8 to 4.16, contrast to those of direct QMC estimations based on Niederreiter sequence. The average is made over the three gauge points. SLFEM with basis function type I and type II are represented by SLFEM-1 and SLFEM-2 in these figures.

It is seen from the result that the performance of SLFEM deteriorates as the number of random variables increase. The type I variant has an advantage on estimating variance and exceedance probability, while the type II variant is better on estimating the mean. This is due to the centre-concentration property of the basis function type II. But generally both the two variants of SLFEM perform worse than QMC quadrature within the range of N used. The reason can be that the $(\log N)^{3(d-1)}$ term in their convergence rate tends to stagnate the convergence until N become very large and the stagnation is severer for larger d.

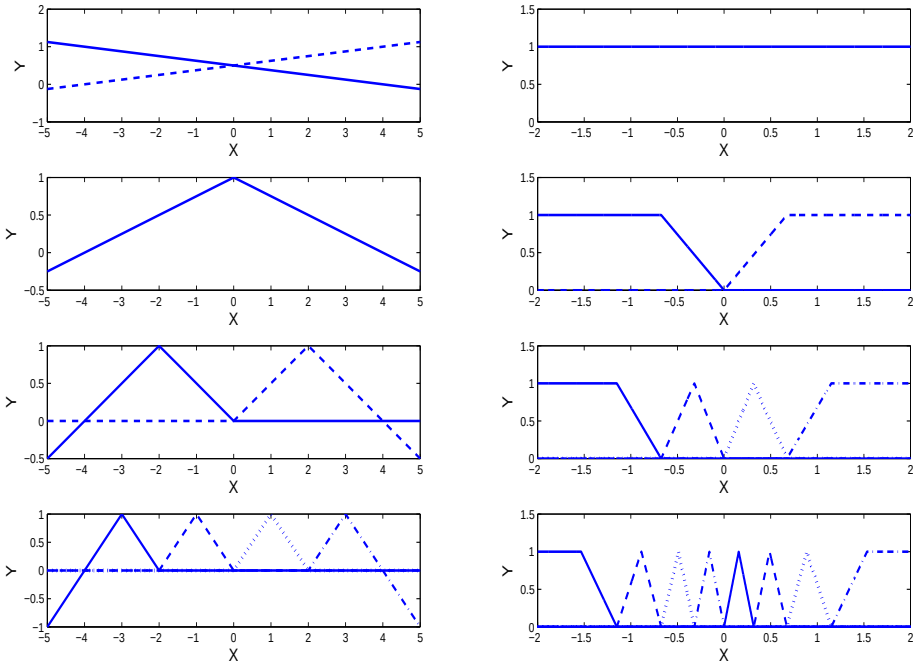

Figure 4.7: Piecewise linear hierarchical basis functions. Type I (left column), level 0 (top) to level 3 (bottom); type II (right column), level 1 (top) to level 4 (bottom).

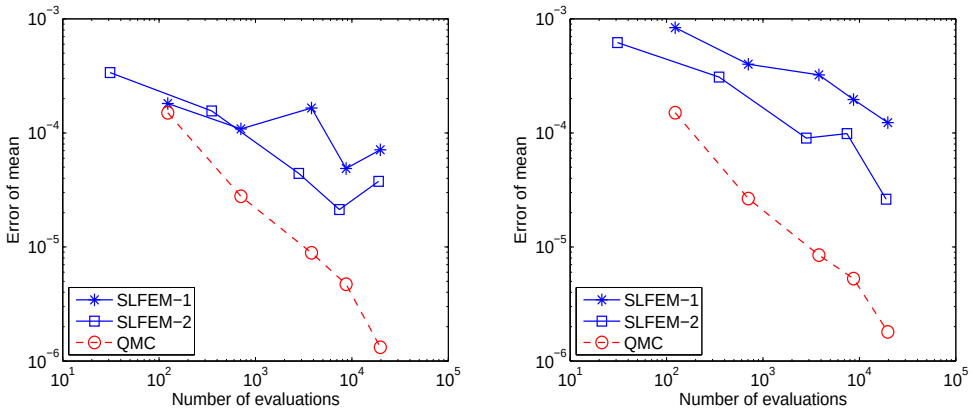

Figure 4.8: Average error of $\mu_{h_{\max}}$ (left) and $\mu_{h_{30}}$ (right), with $d = 3$

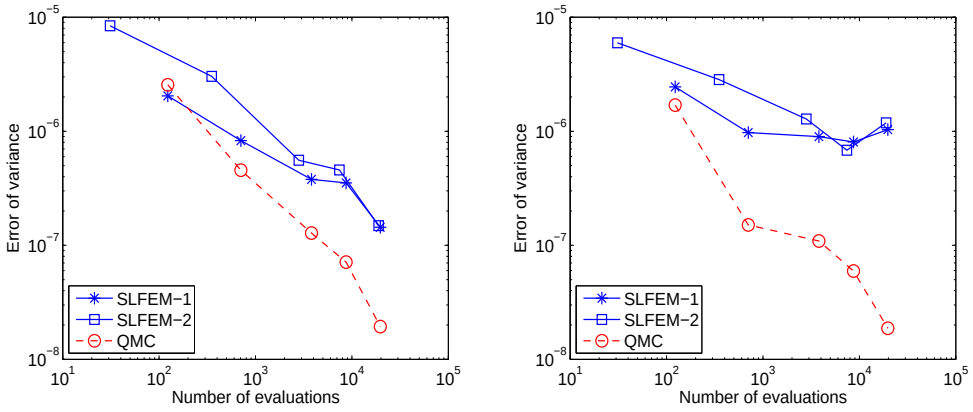

Figure 4.9: Average error of $\sigma^2_{h_{\max}}$ (left) and $\sigma^2_{h_{30}}$ (right), with $d = 3$

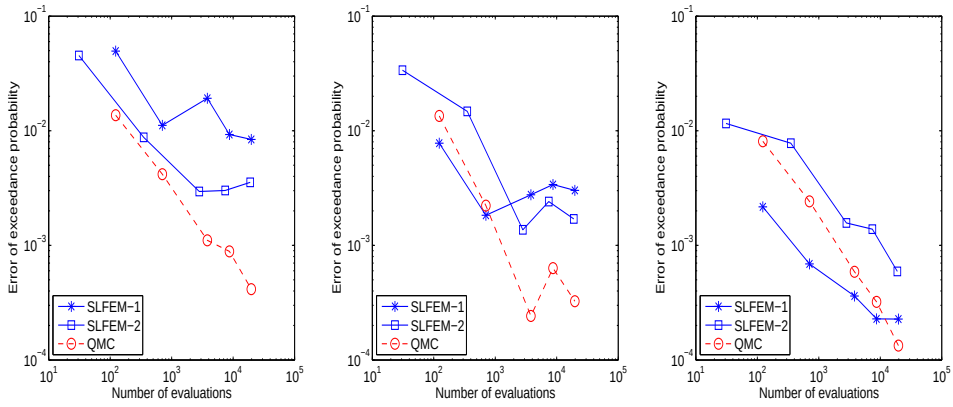

Figure 4.10: Average error of $P_{h_{\max},1}$, $P_{h_{\max},2}$ and $P_{h_{\max},3}$ with $d = 3$

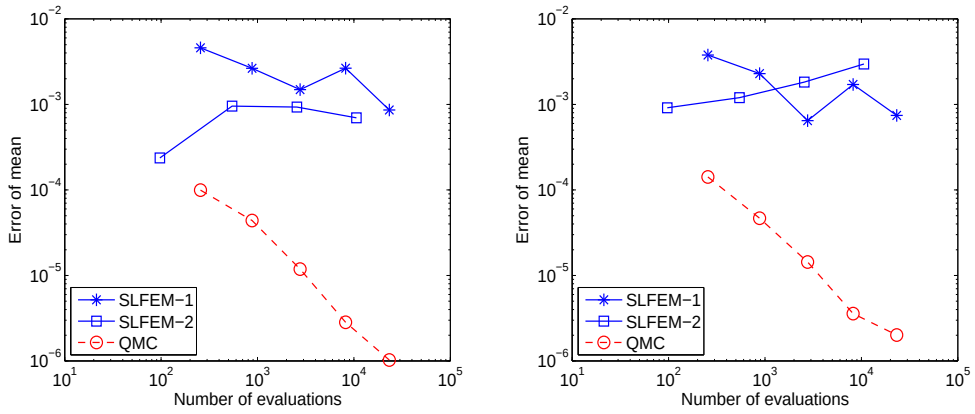

Figure 4.11: Average error of $\mu_{h_{\max}}$ (left) and $\mu_{h_{30}}$ (right), with $d = 6$

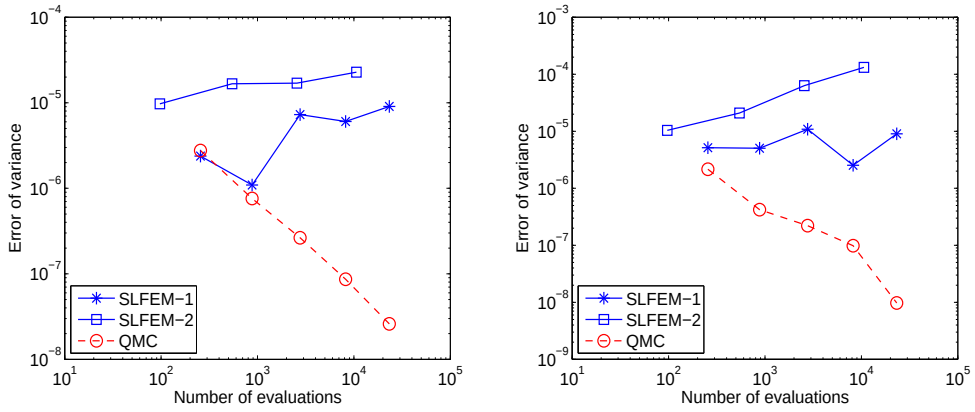

Figure 4.12: Average error of $\sigma^2_{h_{\max}}$ (left) and $\sigma^2_{h_{30}}$ (right), with $d = 6$

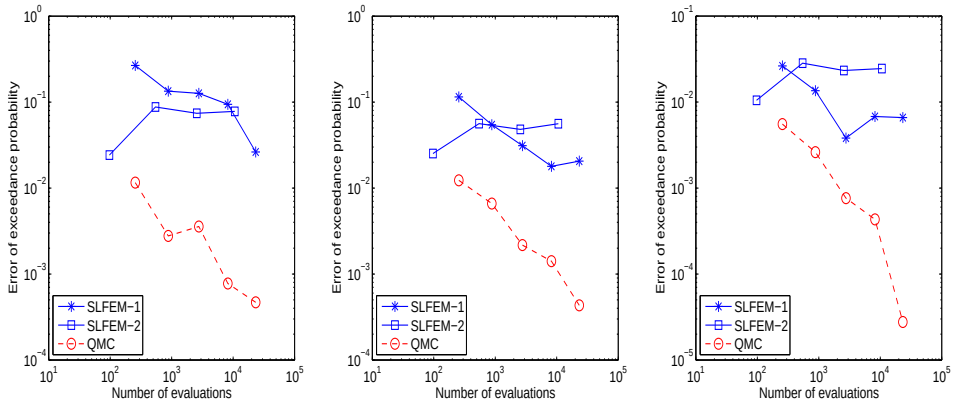

Figure 4.13: Average error of $P_{h_{\max},1}$, $P_{h_{\max},2}$ and $P_{h_{\max},3}$ with $d = 6$

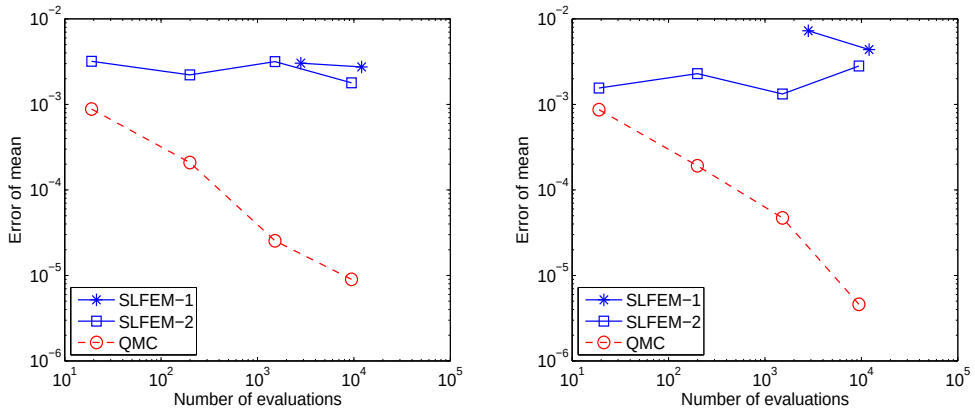

Figure 4.14: Average error of $\mu_{h_{\max}}$ (left) and $\mu_{h_{30}}$ (right), with $d = 9$

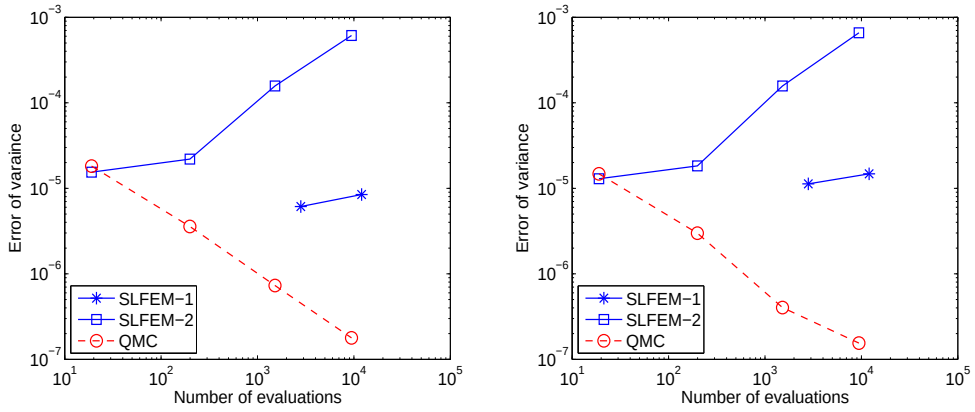

Figure 4.15: Average error of $\sigma^2_{h_{\max}}$ (left) and $\sigma^2_{h_{30}}$ (right), with $d = 9$

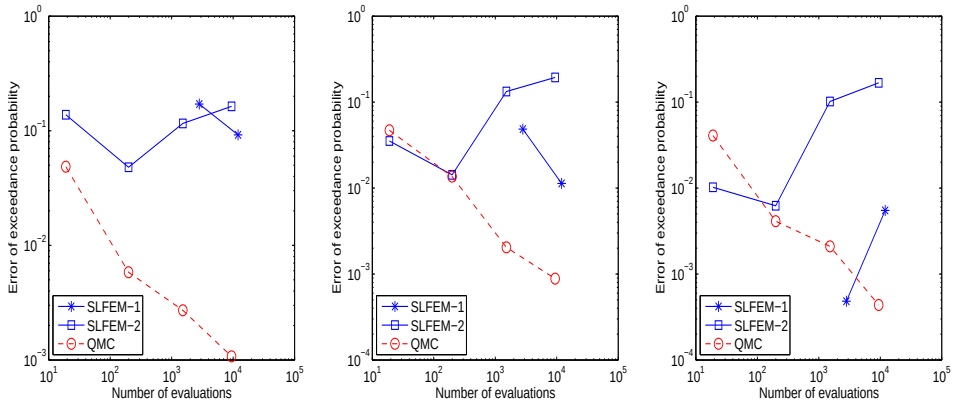

Figure 4.16: Average error of $P_{h_{\max},1}$, $P_{h_{\max},2}$ and $P_{h_{\max},3}$ with $d = 9$

4.4 Monte Carlo and quasi-Monte Carlo quadratures

Monte Carlo and and quasi-Monte Carlo quadratures are equal-weight quadrature rules whose convergence require the slightest smoothness assumptions on the integrands. In this section these two groups of quadrature rules are briefly introduced. Their performances on the stochastic SWE model are observed and discussed.

4.4.1 Monte Carlo quadrature

The Monte Carlo (MC) quadrature [35, 16] is relatively robust and versatile. It is based on the probabilistic interpretation of an integral. Suppose $\{\boldsymbol{\xi}^{(n)}\}_{n=1}^{N}$ are N random realisations of $\boldsymbol{\xi} \in \Omega = [0,1]^d$, MC quadrature approximates the integral by taking the average of $f(\boldsymbol{\xi}^{(n)})$,

$$\mathrm{Q}_N^{\mathcal{M}}[f] = \frac{1}{N}\sum_{n=1}^{N} f(\boldsymbol{\xi}^{(n)})$$

where $\mathrm{Q}_N^{\mathcal{M}}$ denotes the MC quadrature operator. Due to the Strong Law of Large Numbers [34], the estimate $\mathrm{Q}_N^{\mathcal{M}}[f]$ as a random variable, is an unbiased estimation of $I[f]$ and converges to $I[f]$ with probability one. The error of this estimation is

$$I[f] - \mathrm{Q}_N^{\mathcal{M}}[f] \approx \sigma_f N^{-\frac{1}{2}}\,\theta$$

in which θ is a standard normal random variable, σ_f is the standard deviation of f. This error bound is probabilistic, so the precision of MC quadrature can only be expressed together with a confidence level. To make sure the error is within size ϵ with a confidence level c, the required number of sample points is

$$N \geq 2\,\epsilon^{-2}\sigma_f^2\,(\mathrm{erf}^{-1}(c))^2$$

It is seen the error of MC quadrature is of order $\mathcal{O}(\sigma_f N^{-1/2})$ which is independent of the number of random variables presents in the problem. This convergence rate is considered slow. It may be sped up by reducing the standard deviation σ_f, which can be done by various variance reduction techniques including antithetic variables, control variates, matching moment methods, stratification, importance sampling, Russian roulette, etc. Detailed introduction of these techniques can be found in [35] and [16].

To generate random samples, MC quadrature requires a reliable pseudo-random number generator(PRNG). Though as finite state machines, any numerical PRNG can only produce a finite sequence of random numbers, it is not difficult to build PRNGs with periods long enough for many practical applications. Some numerical PRNG packages generate reliable long sequences of such pseudo-random numbers, see [16], [73], [85], [84] and [109]. The PRNG used in this work is due to [84] which is default in Matlab versions 5 and later. The period of it is approximately 2^{64}.

4.4.2 Quasi-Monte Carlo quadratures

Quasi-Monte Carlo (QMC) quadrature [97, 16] evaluates the integrand on abscissas consist of a *low discrepancy* point set which is generated by deterministic number-theoretic formulas and is more uniformly distributed than pseudo-random sequence. Suppose $P = \{\boldsymbol{x}_n\}_{n=1}^N$ is an N-point low discrepancy point set on $\Omega = [0,1]^d$. A N-points quasi-Monte Carlo quadrature formula $\mathrm{Q}_N^{\mathcal{Q}}$ is defined as,

$$\mathrm{Q}_N^{\mathcal{Q}}[f] = \frac{1}{N}\sum_{n=1}^{N} f(\boldsymbol{x}_n)$$

The upper bound of the error of $\mathrm{Q}_N^{\mathcal{Q}}$ can be obtained from the Koksma-Hlawka inequality [16], i.e., if f is of bounded total variation $V(f)$ in the sense of Hardy and Krause, then

$$|\mathrm{Q}_N^{\mathcal{Q}} f - \mathrm{I} f| \leq V(f) D^*(P) \tag{4.4}$$

with $D^*(P)$ the *star discrepancy* of point set P. A detailed definition of total variation can be found in [75], a definition of *star discrepancy* is given below.

For an arbitrary subset B of Ω, define the measure

$$A(B;P) = \sum_{n=1}^{N} c_B(\boldsymbol{x}_n)$$

where c_B is the characteristic function of B. Thus $A(B;P)$ is the counting function indicates the number of points $\boldsymbol{x}_n \in B$ in P. If $\mathcal{B}$ is a non-empty family of Lebesgue-measureable subsets of Ω, then a general notion of discrepancy of the point set P is

$$D_N(\mathcal{B};P) = \sup_{B\in\mathcal{B}} \left| \frac{A(B;P)}{N} - \lambda_d(B) \right|$$

where λ_d is a d-dimensional Lebesgue measure. The star discrepancy $D_N^*(P)$ is defined by $D_N^*(P) = D_N(\mathcal{J}^*;P)$, where $\mathcal{J}^*$ is the family of all subdomain of Ω in the form $\prod_{i=1}^d [0,u_i)$. The (extreme) discrepancy $D_N(P)$ is defined by $D_N(P) = D_N(\mathcal{J};P)$, where $\mathcal{J}$ is the family of all subdomain of Ω in the form $\prod_{i=1}^d [u_i,v_i)$. [97] shows the following inequality holds,

$$D_N^*(P) \leq D_N(P) \leq 2^d D_N^*(P)$$

A variety of different low discrepancy sequences exist, e.g. Van der Corput sequence, Halton sequence, Sobol sequence, Niederreitor sequence (also known as (t,s)-sequence) etc., see [97] for a detailed description of them. All of them satisfy the following bound of star discrepancy,

$$D_N^*(P) \leq c_d (\log N)^d N^{-1} \tag{4.5}$$

in which c_d is a constant depending on d. When d is large, c_d's of Niederreitor sequence is much smaller than that of the other low discrepancy sequences.

Good lattice points $\{\boldsymbol{x}_n\}_{n=1}^N$ are defined as points within $[0,1]^d$ as the fractional parts of a rational sequence, i.e.,

$$\boldsymbol{x}_n = \mathrm{rem}\left(\frac{n}{N}\mathbf{g},\ 1\right) \quad \text{for } n = 0, 1, \cdots, N-1$$

where $N \in \mathbb{N}$ is a common denominator, $\mathrm{rem}(a,b)$ is the remainder on division of a by b, $\mathbf{g} \in \mathbb{Z}^d$ is a d-dimensional integer vector. This points set also has the discrepancy bound (4.5). For some specially chosen $\mathbf{g}$, c_d is smaller. Such a $\mathbf{g}$ is informally called a *good lattice point* mod N, and they are tabulated in [62] for dimension up to 18.

For QMC quadrature using point sequences with the discrepancy bound (4.5), the Koksma-Hlawka inequality (4.4) implies that the integration error is

$$|\mathrm{Q}_N^{\mathcal{Q}} f - \mathrm{I} f| \leq c_d V(f) N^{-1} (\log N)^d \tag{4.6}$$

This shows the error of $\mathrm{Q}_N^{\mathcal{Q}}$ is of order $\mathcal{O}(N^{-1}(\log N)^d)$ which is better than that of MC quadrature $\mathrm{Q}_N^{\mathcal{M}}$. [72] investigates possible error estimators for QMC integration. According to [16], the advantage of $\mathrm{Q}_N^{\mathcal{Q}}$ over $\mathrm{Q}_N^{\mathcal{M}}$ reduces when the number of dimension of the integral become large or when the integrand is not smooth. Work in [94] shows QMC quadrature works better on smooth and continuous integrands while worse on discontinuous ones.

It should also be noticed that (4.6) is an upper bound of QMC quadrature's error but not an estimation. In many applications it turns out to be a quite loose upper bound.

In this work QMC quadratures that use Niederreiter sequence and good lattice points are applied on the stochastic SWE model. The Niederreiter sequence is generated by the program from [13], and the good lattice points are generated on the basis of [62].

4.4.3 Numerical results on the model

MC and QMC quadratures are applied on the stochastic SWE model with 3, 6 and 9 random variables respectively to estimate the target statistics. The average errors of these estimations along the number of model evaluations are graphed in Figure 4.17 to 4.25. QMC quadratures using Niederreiter sequence and good lattice points are represented by QMC-N and QMC-G respectively in these figures. The average is made over the three gauge points. The MC results are averages of 20 runs.

The results show that as expected QMC quadratures perform better than MC quadrature. But QMC quadratures's efficiency does not obviously deteriorate along increasing number of dimensions up to $d = 9$, even with relatively small N. This is an example reflecting the fact that $\mathcal{O}(N^{-1}(\log N)^d$ is an upper bound of its error but not an estimation.

There shows no significant difference in the performance of QMC with Niederreiter sequence and with good lattice points.

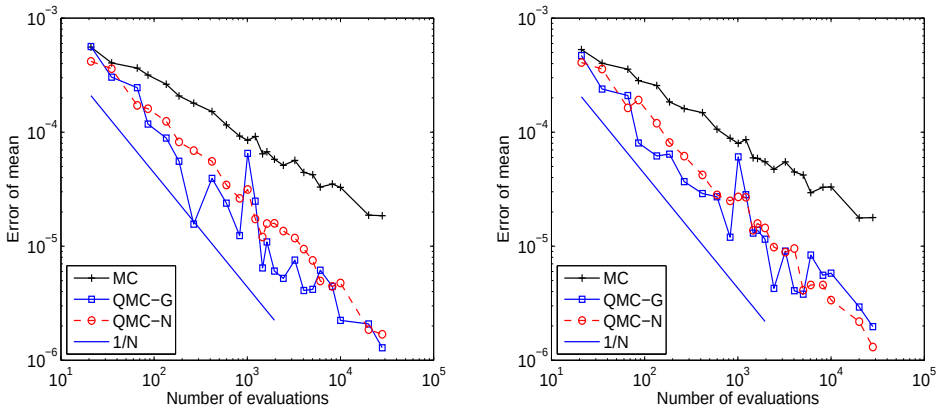

Figure 4.17: Average error of $\mu_{h_{\max}}$ (left) and $\mu_{h_{30}}$ (right), with $d = 3$

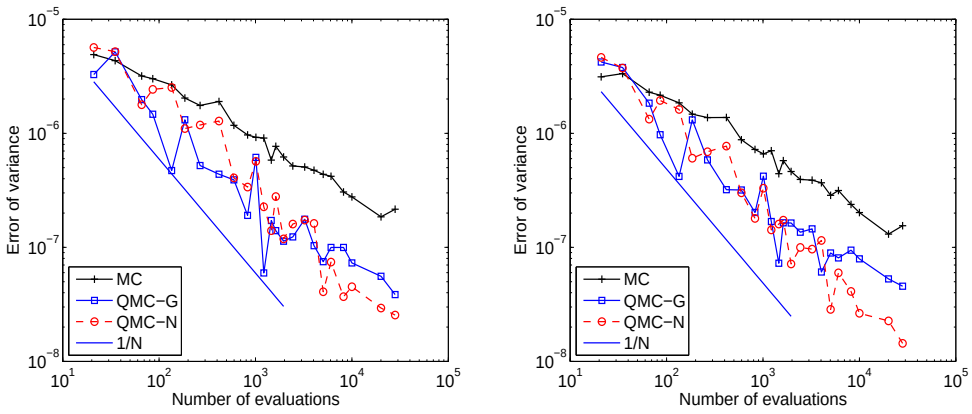

Figure 4.18: Average error of $\sigma^2_{h_{\max}}$ (left) and $\sigma^2_{h_{30}}$ (right), with $d = 3$

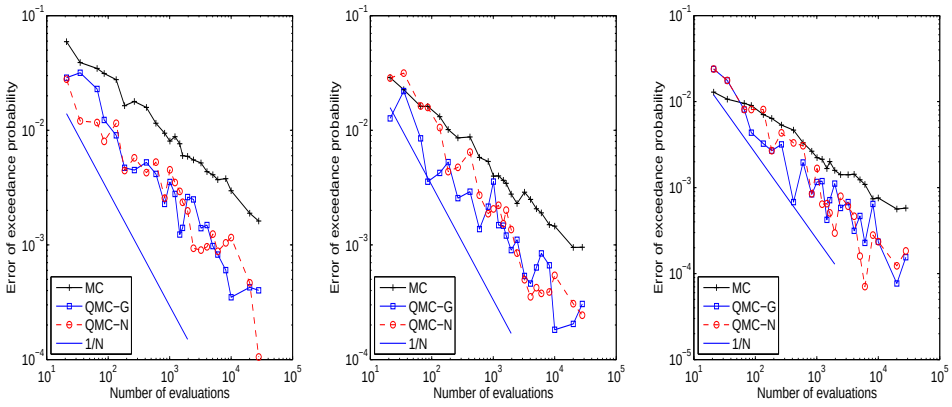

Figure 4.19: Average error of $P_{h_{\max},1}$, $P_{h_{\max},2}$ and $P_{h_{\max},3}$ with $d = 3$

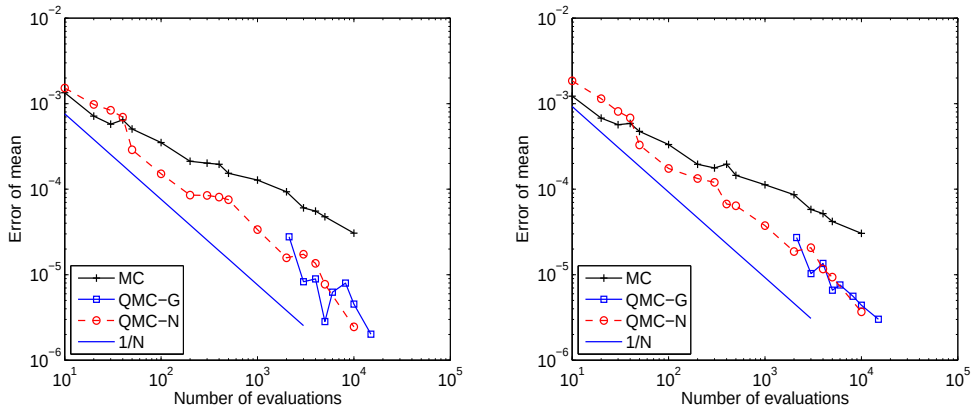

Figure 4.20: Average error of $\mu_{h_{\max}}$ (left) and $\mu_{h_{30}}$ (right), with $d = 6$

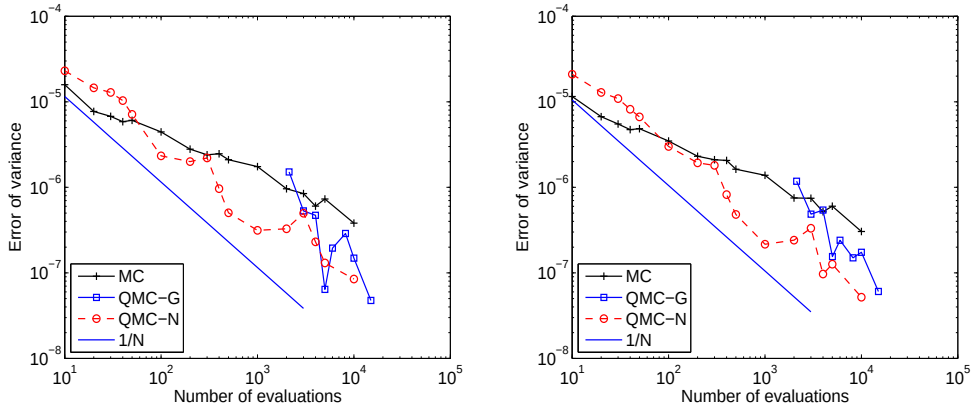

Figure 4.21: Average error of $\sigma^2_{h_{\max}}$ (left) and $\sigma^2_{h_{30}}$ (right), with $d = 6$

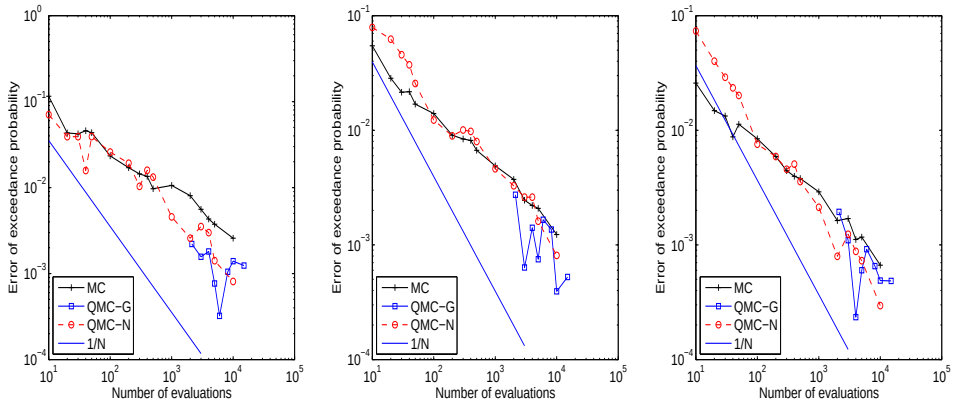

Figure 4.22: Average error of $P_{h_{\max},1}$, $P_{h_{\max},2}$ and $P_{h_{\max},3}$ with $d = 6$

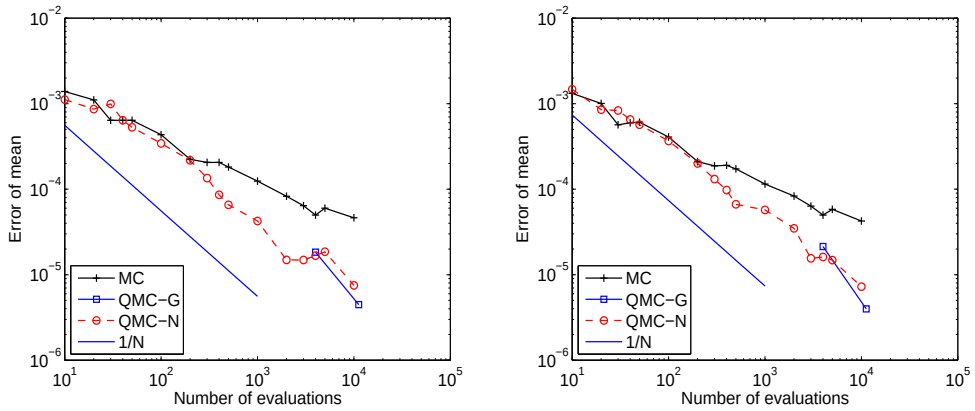

Figure 4.23: Average error of $\mu_{h_{\max}}$ (left) and $\mu_{h_{30}}$ (right), with $d = 9$

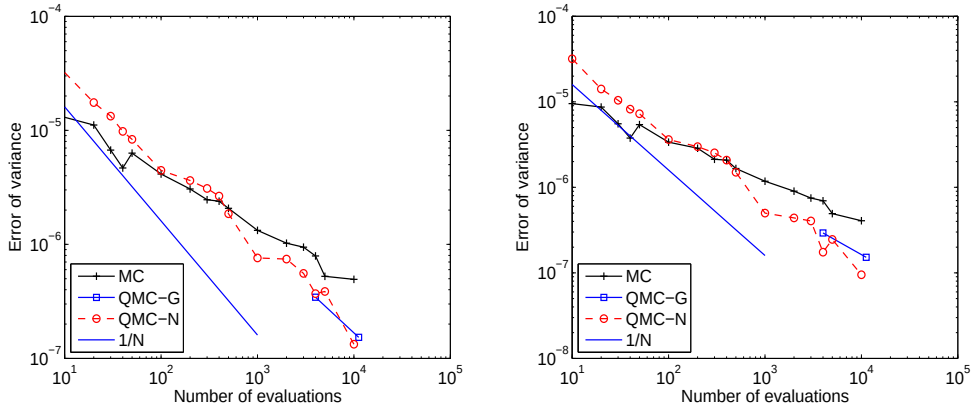

Figure 4.24: Average error of $\sigma^2_{h_{\max}}$ (left) and $\sigma^2_{h_{30}}$ (right), with $d = 9$

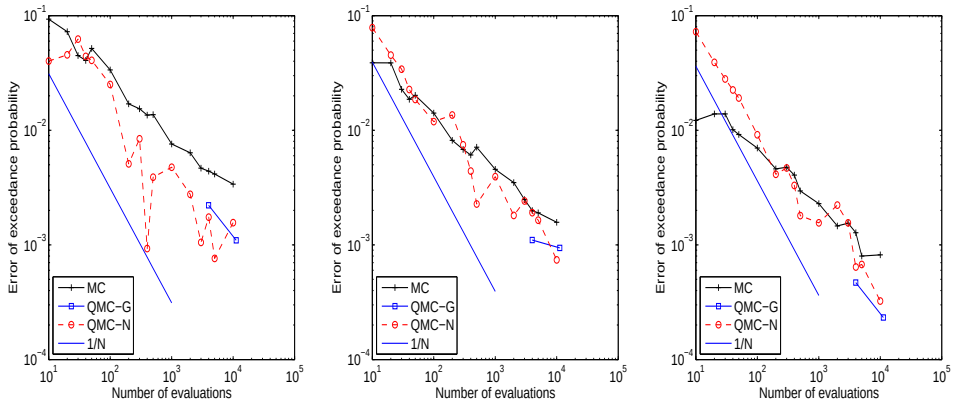

Figure 4.25: Average error of $P_{h_{\max},1}$, $P_{h_{\max},2}$ and $P_{h_{\max},3}$ with $d = 9$

4.5 Uncorrelated dimensions quadratures

Two novel quadrature rules, uncorrelated dimensions (UD) quadrature and compound uncorrelated dimensions (CUD) quadrature are introduced in this section. This starts from two exceptional examples that lead to the introducing of *splittable multidimensional integration* and *(compound) slash grid*, whereon the UD and CUD quadratures are subsequently described and analysed. It is proved that for integrands f that can be expressed in the form of multilinear functionals of any integrable functions, the convergence rate of CUD quadrature is $\mathcal{O}(N^{-2})$ for $f \in C^2$ with uniformly distributed variables, that of UD quadrature is $\mathcal{O}(N^{-1})$ for f with bounded variation. Both the two rates are dimension-independent. This is a break to the "curse of dimension". Numerical experiments on the two quadratures are also presented, the results of the experiments conform with the theoretical analysis.

4.5.1 Two exceptional examples

A significant portion of d-dimensional integration problems can be splitted into d 1-dimensional (1-D) integration problems, here are two 2-D examples with independent variables $x_1, x_2 \in \Omega = [0,1]^2$ in which this splitting is exceptionally easy. Let

$$f_1(x_1, x_2) = \phi_1(x_1) + \phi_2(x_2)$$

$$f_2(x_1, x_2) = \psi(x_1, x_2)$$

with ϕ_1 and ϕ_2 any integrable functions, and ψ a bilinear function. Their integrations on domain Ω are respectively the expectations

$$\begin{aligned} \mathbb{E}[f_1(x_1, x_2)] &= \mathbb{E}[\phi_1(x_1)] + \mathbb{E}[\phi_2(x_2)] \\ \mathbb{E}[f_2(x_1, x_2)] &= \psi[\mathbb{E}(x_1), \mathbb{E}(x_2)] + \upsilon[\mathrm{cov}(x_1, x_2)] \\ &= \psi[\mathbb{E}(x_1), \mathbb{E}(x_2)] + \upsilon[\mathbb{E}(x_1 - \mu_1)\mathbb{E}(x_2 - \mu_2)] \end{aligned}$$

with υ a linear function. It is seen the both integrations of the 2-D function f_1 and f_2 are readily splitted into 1-D integrations on variables x_1 and x_2 respectively due to the linearity of expectation operations and the independence of the variables. If the expression of ϕ_1, ϕ_2, ψ and υ are known, these 1-D integrations can be done separately. But these two examples are exceptional because even the expressions of those Greek letter functions are unknown, it is still very easy to integrate them in a 1-D way. E.g, it suffices to integrate f_1 on the diagonal of the domain $\Omega = [0,1]^2$, as shown in the (a) part of Figure 4.26, since uniform samples on the diagonal can provide uniform samples on x_1 and x_2 simultaneously. The integration of f_2 can be done along the two diagonals of Ω, as shown in the (b) part of Figure 4.26, because in addition to the simultaneous uniformity on both dimensions, such sampled $\mathrm{cov}(x_1, x_2)$ has the value zero, just happens to equal its exact value.

These two examples is a tip of an iceberg that is termed as *splittable multidimensional integration* in this work, to which a definition is given below.

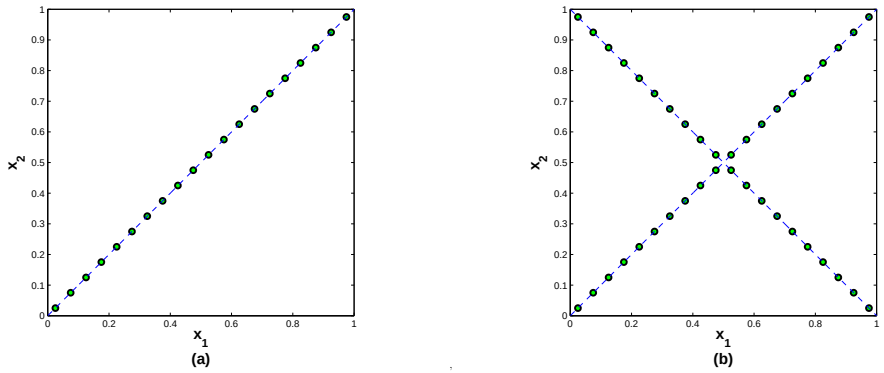

Figure 4.26: (a): Diagonal sampling for f_1. (b): Sampling for f_2 on two diagonals

4.5.2 Splittable multidimensional integration

Definition 1. *If a function $f(x_1, x_2, \cdots, x_d)$ with independent variables $\{x_i \in [a_i, b_i] : a_i, b_i \in \mathbb{R},\ i = 1, 2, \cdots, d\}$ can be expressed in the form*

$$f(x_1, x_2, \cdots, x_d) = \Psi(\phi_1(x_1), \phi_2(x_2), \cdots, \phi_d(x_d))$$

where ϕ_i's are any integrable functions, and Ψ is a multilinear function, then the integration of f on the domain $\Omega = \prod_{i=1}^{d}[a_i, b_i]$,

$$\mathbb{E}(f) = \int_{\Omega} \Psi(\phi_1(x_1), \phi_2(x_2), \cdots, \phi_d(x_d))\mathrm{d}x_1\mathrm{d}x_2\cdots\mathrm{d}x_d$$

is a splittable multidimensional integration. And f is a dimension-splittable function.

Example 1. *Integrations of all polynomials are splittable multidimensional integrations.*

Here also define some terms for later use. Let an integer set $S = \{1, 2, \cdots, d\}$, $B_t = \{b_1, b_2, \cdots, b_{z_t}\} \subseteq S$ is an arbitrary subset of S with $2 \le z_t \le d$, and $b_1 < b_2 < \cdots < b_{z_t}$. For a particular multilinear function Ψ, $\mathcal{B} = \cup B_t$ is the union of some certain B_t's so that every product of ϕ_i's in Ψ has a $B_t \in \mathcal{B}$ containing all the index i's involved in the product. E.g., for $\Psi = \phi_1\phi_2 + \phi_3\phi_5\phi_6 - \phi_4$, $\mathcal{B} = \{\{1, 2\}, \{3, 5, 6\}\}$.

A splittable d-dimensional integration can be approximated by a function of d 1-D integrations. To show this let's begin with the lemma below. In this lemma and thereafter $\mathbb{E}(f) = \int_{\Omega} f(\boldsymbol{x})\mathrm{d}\boldsymbol{x}$ with $\boldsymbol{x} \in \Omega = [0, 1]^d$.

Lemma 1. *Given an integer $z \ge 2$, and φ_i denotes an integrable function $\varphi_i(x_i)$,*

$$\mathbb{E}\left(\prod_{i=1}^{z}\varphi_i\right) = \prod_{i=1}^{z}\mathbb{E}(\varphi_i) + \sum_{i=1}^{z-1}\left[\mathrm{cov}\left(\varphi_i, \prod_{j=i+1}^{z}\varphi_j\right)\cdot\prod_{k=1}^{i-1}\mathbb{E}(\varphi_k)\right]$$

Proof. Since

$$\mathbb{E}(\varphi_1\varphi_2) = \mathbb{E}(\varphi_1)\mathbb{E}(\varphi_2) + \mathrm{cov}(\varphi_1,\ \varphi_2)$$

The proof is obtained by applying the below relation recursively,

$$\mathbb{E}\left(\prod_{i=1}^{z}\varphi_i\right)=\mathbb{E}(\varphi_1)\cdot\mathbb{E}\left(\prod_{i=2}^{z}\varphi_i\right)+\operatorname{cov}\left(\varphi_1,\ \prod_{i=2}^{z}\varphi_i\right)$$

□

Proposition 1. *A splittable integration as in Definition 1 can be expressed as,*

$$\begin{aligned}\mathbb{E}(f)=&\mathbb{E}\left[\Psi(\phi_1,\phi_2,\cdots,\phi_d)\right]\\ =&\Psi(\mathbb{E}(\phi_1),\mathbb{E}(\phi_2)\cdots,\mathbb{E}(\phi_d))+\sum_{B_t\in\mathcal{B}}\gamma_t\sum_{i=1}^{z_t-1}\alpha_{t,i}C_{t,i}\end{aligned}\tag{4.7}$$

where for a certain B_t, γ_t is a constant,

$$C_{t,i}=\operatorname{cov}(\phi_{b_i}\ ,\ \phi_{b_{i+1}}\phi_{b_{i+2}}\cdots\phi_{b_{z_t}})$$

and

$$\alpha_{t,i}=\prod_{k=1}^{i-1}\mathbb{E}(\phi_{b_k})$$

Proof. By linearity of expectations, for any $B_t\subseteq S$,

$$\mathbb{E}\left(\sum_{i=1}^{z_t}c_i\phi_{b_i}\right)=\sum_{i=1}^{z_t}c_i\mathbb{E}(\phi_{b_i})$$

with c_i's constants, and by Lemma 1,

$$\mathbb{E}\left(\prod_{i=1}^{z_t}c_i\phi_{b_i}\right)=\prod_{i=1}^{z_t}c_i\mathbb{E}(\phi_{b_i})+\prod_{i=1}^{z_t}c_i\sum_{i=1}^{z_t-1}\left[\operatorname{cov}(\phi_{b_i},\prod_{j=i+1}^{z_t}\phi_{b_j})\prod_{k=1}^{i-1}\mathbb{E}(\phi_{b_k})\right]$$

and the proof follows since Ψ is multilinear. □

Since $C_{t,i}$'s are all zero due to the mutual independence of x_i's, Proposition 1 actually says a splittable multidimensional integration (SMI) can be expressed by a function of 1-D integrations, regardless to the dimensionality of the SMI. But this dimensionality-independence does not directly apply to the quadrature approximation of the SMI, because the sampled $C_{t,i}$'s on the quadrature abscissas are not necessarily zeros.

Proposition 1 hints that an efficient quadrature rule for SMI should be simultaneously efficient on two tasks, i.e., 1-D numerical integrations on every individual dimensions, and the elimination of $C_{t,i}$'s. In the following sections the uncorrelated dimensions quadrature and its compound version are introduced which possess these properties. This starts with the definition of *slash grid* and *compound slash grid*.

4.5.3 Slash grid and compound slash grid

4.5.3.1 Definition

The 2-D *slash grids* (SG) are defined as

$$U^2_{J_1} = \{(x_1, x_2) : x_1 \in [0,1],\ x_2 = \lambda_1(x_1, m)\} \tag{4.8}$$
$$U^2_{J_2} = \{(x_1, x_2) : x_1 \in [0,1],\ x_2 = \lambda_2(x_1, m)\} \tag{4.9}$$

and the 2-D *compound slash grid* (CSG) is the union

$$U^2 = \bigcup_{i=1}^{2} U^2_{J_i} \tag{4.10}$$

λ_1, λ_2 are the *permuting functions* defined as

$$\lambda_1(x, m) = m \cdot \mathrm{rem}(x, 1/m)$$
$$\lambda_2(x, m) = 1 - \lambda_1(x, m)$$

where $\mathrm{rem}(a, b)$ is the remainder on division of a by b. Figure 4.27 shows an example of 2-D CSG with $m = 5$ and its corresponding SGs.

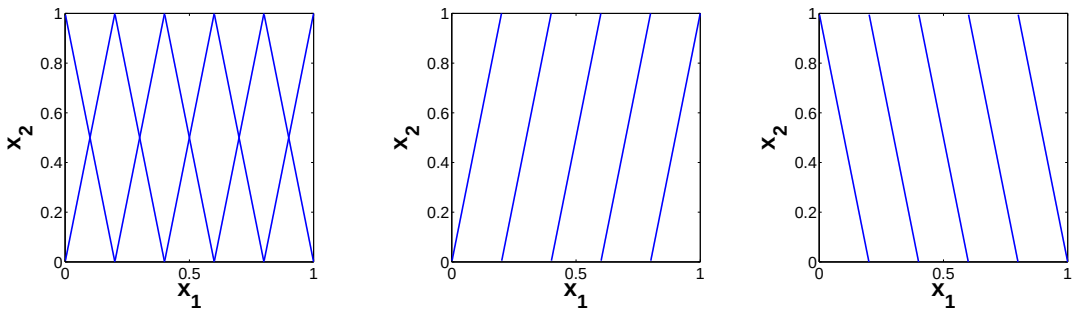

(a) $U^2 = U^2_{J_1} \cup U^2_{J_2}$ (b) $U^2_{J_1}$ (c) $U^2_{J_2}$

Figure 4.27: An example of 2-D CSG and SGs, with $m = 5$

To formulate the general expression of d-dimensional SG and CSG, define

$$\mathcal{J}^d = \{J_\alpha = (j_1^{(\alpha)}, j_2^{(\alpha)}, \cdots, j_{d-1}^{(\alpha)}) \ :\ j_i^{(\alpha)} = \mathfrak{B}_i(\alpha) + 1,\ i \in \mathbb{N}, i \le d-1, \\ \alpha \in \mathbb{N}, \alpha \le 2^{d-1}\}$$

where $\mathfrak{B}_i(\alpha)$ is the integer (either 0 or 1) on the i-th digit, counting from the leftmost, of the $(d-1)$-digit binary form representation of $\alpha - 1$.

For any $1 \le \alpha \le 2^{d-1}$, define the $\boldsymbol{m}$-level d-dimensional SG as,

$$U^d_{J_\alpha} = \{(x_1, x_2, \cdots, x_d) : x_1 \in [0,1],\ x_{i+1} = \lambda_{j_i^{(\alpha)}}(x_i, m_i), i \in \mathbb{N}, i \le d-1\} \tag{4.11}$$

It is seen from the above expression that on a SG, if $i > j$, x_i is a function of x_j, let it be expressed by $x_i = \boldsymbol{\lambda}_{J_\alpha, i \to j}(x_j, \boldsymbol{m})$ for later use.

The $\boldsymbol{m}$-level d-dimensional CSG is the union

$$U^d = \bigcup_{J_\alpha \in \mathcal{J}^d}^{\mathcal{J}^d} U^d_{J_\alpha} \tag{4.12}$$

4.5.3.2 Convergence of $C_{t,i}$ on SG and CSG

Both SG and CSG have the property that they have $C_{t,i}$ evaluated on them converge to zero as $\min(\boldsymbol{m}) \to \infty$. To show this let's start from the following proposition.

Proposition 2. *On a domain* $[0,1]$*, if* $\varphi(u)$ *has bounded variation and* $\chi(u)$ *is bounded and periodic with a period* $1/m$*,* $\operatorname{cov}[\varphi(u), \chi(u)]$ *converges to zero as* $m \to \infty$*, at a rate of order* $\mathcal{O}(m^{-1})$*.*

Proof. Let $\Delta = 1/m$, $u_i = \frac{i-1}{m}$, $i \leq m$, then

$$
\begin{aligned}
&\operatorname{cov}[\varphi(u), \chi(u)] \\
=&\int_0^1 \big[\varphi(u) - \mathbb{E}(\varphi)\big]\big[\chi(u) - \mathbb{E}(\chi)\big]\mathrm{d}u \\
=&\int_0^1 \big[\varphi(u) - \mathbb{E}(\varphi)\big]\chi(u)\mathrm{d}u \\
=&\sum_{i=1}^{m}\int_0^{\Delta} \big[\varphi(u_i + t) - \mathbb{E}(\varphi)\big]\chi(t)\mathrm{d}t \\
=&\sum_{i=1}^{m}\int_0^{\Delta} \big[\varphi(u_i) + v_i(t) - \mathbb{E}(\varphi)\big]\chi(t)\mathrm{d}t \\
=&\Big(\sum_{i=1}^{m}\varphi(u_i) - m\mathbb{E}(\varphi)\Big)\int_0^{\Delta}\chi(t)\mathrm{d}t + \sum_{i=1}^{m}\int_0^{\Delta} v_i(t)\chi(t)\mathrm{d}t
\end{aligned}
\tag{4.13}
$$

where $v_i(t) = \varphi(u_i + t) - \varphi(u_i)$. According to [97, Theorem 2.6], the star discrepancy of the point set $\{u_i\}$ is

$$D^*(\{u_i\}) = \frac{1}{m}$$

by Koksma-Hlawka inequality,

$$\left|\sum_{i=1}^{m}\varphi(u_i) - m\mathbb{E}(\varphi)\right| \leq m \cdot V(\varphi)D^*\big(\{u_i\}\big) = V(\varphi)$$

$V(\cdot)$ denotes the total variation. If set

$$c_1 = \max_{t\in[0,\Delta]}\big[\chi(t)\big]$$

The first term in equation (4.13) can be bounded by

$$\Big(\sum_{i=1}^{m}\varphi(u_i) - m\mathbb{E}(\varphi)\Big)\int_0^{\Delta}\chi(t)\mathrm{d}t \leq c_1 V(\varphi)m^{-1}$$

And since φ has bounded variation, there exists such a constant c_2

$$c_2 = \max_{\substack{m\in\mathbb{N}\\ t\in[0,\Delta]}}\left(\sum_{i=1}^{m} v_i(t)\right)$$

The second term in equation (4.13) can be bounded by

$$\sum_{i=1}^{m}\int_0^{\Delta} v_i(t)\chi(t)\mathrm{d}t \le c_1\int_0^{\Delta}\sum_{i=1}^{m} v_i(t)\mathrm{d}t \le c_1c_2\cdot m^{-1}$$

The above inequalities lead to the result that $\mathrm{cov}[\varphi(u),\chi(u)]$ converges to zero as $m\to\infty$, at a rate of order $\mathcal{O}(m^{-1})$. □

Corollary 1. *$\forall B_t\subseteq S$, if ϕ_{b_i} is of bounded variation, $C_{t,i}$ evaluated on an $\boldsymbol{m}$-level d-dimensional SG converges to zero as $\min(\boldsymbol{m})\to\infty$, at a rate of order $\mathcal{O}(\min(\boldsymbol{m})^{-1})$.*

Proof. Since on a SG, all x_{b_j} with $j>i$ are bounded periodic function of x_{b_i} with a period at most $1/m_{b_i}$, and so is the function $\prod_{j=i+1}^{z_t}\phi_{b_j}$. □

Corollary 2. *$\forall B_t\subseteq S$, if ϕ_{b_i} is of bounded variation, $C_{t,i}$ evaluated on an $\boldsymbol{m}$-level d-dimensional CSG converges to zero as $\min(\boldsymbol{m})\to\infty$, at a rate of order at most $\mathcal{O}(\min(\boldsymbol{m})^{-1})$.*

Proof. The proof follows the fact that $C_{t,i}|_{\boldsymbol{x}\in U^d}$ is an average of $C_{t,i}|_{\boldsymbol{x}\in U^d_{J_\alpha}}$'s with α ranges from 1 to 2^{d-1}, i.e.,

$$C_{t,i}|_{\boldsymbol{x}\in U^d} = \frac{1}{2^{d-1}}\sum^{J_\alpha\in\mathcal{J}^d} C_{t,i}|_{\boldsymbol{x}\in U^d_{J_\alpha}}$$

□

4.5.4 Uncorrelated dimensions quadratures

Uncorrelated dimensions (UD) quadrature and compound uncorrelated dimensions (CUD) quadrature are equal-weight quadrature rules that have their abscissas on SG and CSG respectively.

Definition 2. *A K-point uncorrelated dimensions quadrature $Q_K^{J_\alpha}$ is*

$$Q_K^{J_\alpha}[g(\boldsymbol{x})] = \frac{1}{K}\sum_{n=1}^{K} g(\boldsymbol{X}_{J_\alpha,K})$$

with the abscissas

$$\boldsymbol{X}_{J_\alpha,K} = \{(x_{1,n},x_{2,n},\cdots,x_{d,n})\in\Omega : x_{1,n}\in\mathcal{X}^K,\ x_{i+1,n}=\lambda_{j_i^{(\alpha)}}(x_{i,n},m_i),\\ n\in\mathbb{N},n\le K,\ \ i\in\mathbb{N},i\le d-1\} \quad (4.14)$$

in which $\Omega=[0,1]^d$, and $\mathcal{X}^K=\{\frac{2k-1}{2K}\ :\ k\in\mathbb{N},k\le K\}$ is the abscissas of a K-point 1-D mid-point rule.

It's worth mentioning that the UD quadrature with index J_1 is related to the quadrature of lattice rule. Since J_1 has all its elements 1, the abscissas of Q^{J_1} are

$$\boldsymbol{X}_{J_1,K} = \{(x_{1,n},x_{2,n},\cdots,x_{d,n})\in\Omega : x_{1,n}\in\mathcal{X}^K,\ x_{i+1,n}=\mathrm{rem}(m_ix_{i,n},1),\\ n\in\mathbb{N},n\le K,\ \ i\in\mathbb{N},i\le d-1\}$$

a part of which bear a resemblance to the expression of abscissas of a lattice rule. A significant difference of the two techniques is that for UD abscissas the x_d to x_1 are successively dependent, while for a lattice rule they are not.

Definition 3. *A N-point compound uncorrelated dimensions quadrature Q_N^C is*

$$Q_N^C[g(\boldsymbol{x})] = \frac{1}{N}\sum_{n=1}^{N} g(\boldsymbol{X}_{C,K})$$

with the abscissas

$$\boldsymbol{X}_{C,K} = \bigcup_{J_\alpha \in \mathcal{J}^d} \boldsymbol{X}_{J_\alpha,K} \tag{4.15}$$

Since $\mathcal{J}^d$ has 2^{d-1} elements, a K-order abscissas $\boldsymbol{X}_{C,K}$ consists of $N = 2^{d-1}K$ points.

4.5.4.1 Simultaneous uniformity of $\boldsymbol{X}_{J_\alpha,K}$ and $\boldsymbol{X}_{C,K}$

Figure 4.28 shows the mapping of $\mathcal{X}_1 = (\frac{1}{8}, \frac{3}{8}, \frac{5}{8}, \frac{7}{8})$ to $\mathcal{X}_2$ by λ_1 or λ_2, it is seen that $\mathcal{X}_2$ is a permutation of $\mathcal{X}_1$ in both cases. Actually the following rule holds,

Proposition 3. *Given $\mathcal{X}_1^K = \{x_{1,k} = \frac{2k-1}{2K} \ : \ k \in \mathbb{N}, k \le K\}$, $\mathcal{X}_2^K = \lambda_1(\mathcal{X}_1^K, m)$ or $\mathcal{X}_2^K = \lambda_2(\mathcal{X}_1^K, m)$ is a permutation of $\mathcal{X}_1^K$ if m is an odd prime number and $m \notin \{K/\hat{\boldsymbol{K}} \ : \ \hat{\boldsymbol{K}} = 1, 2, \cdots, K-1\}$.*

Proof. It suffices to prove the proposition for $\mathcal{X}_2^K = \lambda_1(\mathcal{X}_1^K, m)$ and that involves λ_2 follows straightforwardly.

Write $\mathcal{X}_2^K = \{x_{2,k} \ : \ k \in \mathbb{N}, k \le K\}$. Since $\mathcal{X}_2^K = \lambda_1(\mathcal{X}_1^K, m) = \mathrm{rem}(m\mathcal{X}_1^K, 1)$, $\mathcal{X}_2^K$ are fraction remainders of $m\mathcal{X}_1^K$, i.e., proper fraction numbers with the same denominator as that of $\mathcal{X}_1^K$ and with odd numerators due to the odd m. That is

$$x_{2,k} \in \{\frac{2k-1}{2K} \ : \ k \in \mathbb{N}, k \le K\} = \mathcal{X}_1^K \tag{4.16}$$

then since $\mathcal{X}_1^K$ and $\mathcal{X}_2^K$ have the same number of elements, it suffices to show that for any $\alpha \neq \beta$, $x_{2,\alpha} \neq x_{2,\beta}$.

For any pair of $x_{1,\alpha}$ and $x_{1,\beta}$, suppose $x_{1,\alpha} > x_{1,\beta}$,

$$m(x_{1,\alpha} - x_{1,\beta}) \in \{m\hat{\boldsymbol{K}}/K \ : \ \hat{\boldsymbol{K}} = 1, 2, \cdots, K-1\}$$

if m is a prime number and $m \notin \{K/\hat{\boldsymbol{K}}\}$, $m(x_{1,\alpha} - x_{1,\beta})$ would not be an integer, i.e., $x_{2,\alpha}$ and $x_{2,\beta}$, being fraction remainder of $mx_{1,\alpha}$ and $mx_{1,\beta}$ respectively, would not be identical. This together with (4.16) finish the proof. □

On the basis of Proposition 3, an important property of the abscissas of both SG and CSG can be shown. For a SG, denote the projection of $\boldsymbol{X}_{J_\alpha,K}$ on the i-th dimension as

$$\boldsymbol{X}_{J_\alpha,K}^{(i)} = \{x_{i,n} \ : \ n \in \mathbb{N}, n \le K\}, \quad i = 1, 2, \cdots, d$$

according to the definition of $\boldsymbol{X}_{J_\alpha,K}$, $\boldsymbol{X}_{J_\alpha,K}^{(1)} = \mathcal{X}^K$ is the abscissas of a K-point mid-point rule. Proposition 3 shows that in this case for every $1 < i \le d$, if $\{\cdot\}$ is an operator that transforms the subjected vector into a set in which the sequence

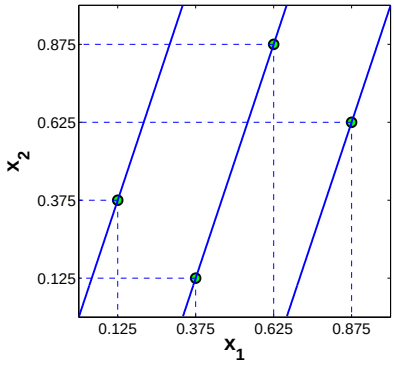

(a) $\boldsymbol{X}_{J_1,4} = \{(\mathcal{X}_1^4, \mathcal{X}_2^4) : \mathcal{X}_2^4 = \lambda_1(\mathcal{X}_1^4, 3)\}$

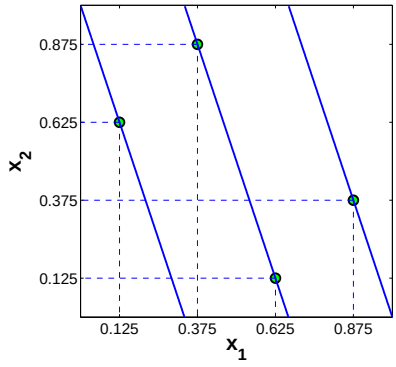

(b) $\boldsymbol{X}_{J_2,4} = \{(\mathcal{X}_1^4, \mathcal{X}_2^4) : \mathcal{X}_2^4 = \lambda_2(\mathcal{X}_1^4, 3)\}$

Figure 4.28: Mappings by permuting functions λ_1 and λ_2

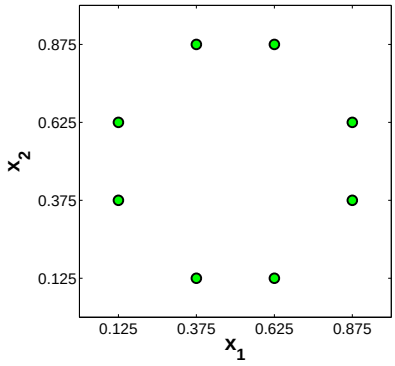

Figure 4.29: 2-D CUD quadrature abscissas $\boldsymbol{X}_{C,4} = \boldsymbol{X}_{J_1,4} \cup \boldsymbol{X}_{J_2,4}$, $m = 3$

of the elements does not count, then $\{\boldsymbol{X}_{J_\alpha,K}^{(i)}\} = \{\mathcal{X}^K\}$. In another words, $\boldsymbol{X}_{J_\alpha,K}$'s projection on every dimension is simultaneously the abscissas of a 1-D K-point mid-point rule if $\boldsymbol{m}$ is properly chosen according to K.

For a CSG, denote the projection of $\boldsymbol{X}_{C,K}$ on the i-th dimension as

$$\boldsymbol{X}_{C,K}^{(i)} = \{x_{i,n} \ : \ n \in \mathbb{N}, n \leq N, N = 2^{d-1}K\}, \quad i = 1, 2, \cdots, d$$

one has the relation

$$\boldsymbol{X}_{C,K}^{(i)} = \bigcup_{J_\alpha \in \mathcal{J}^d}^{\mathcal{J}^d} \boldsymbol{X}_{J_\alpha,K}^{(i)}$$

It is obvious that $\{\boldsymbol{X}_{C,K}^{(i)}\} = \{\mathcal{X}^K\} \times 2^{d-1}$, i.e., $\boldsymbol{X}_{C,K}^{(i)}$ is a multiset with the same set of elements as in $\mathcal{X}^K$, but every element in $\boldsymbol{X}_{C,K}^{(i)}$ has an multiplicity 2^{d-1}. This shows $\boldsymbol{X}_{C,K}^{(i)}$ is also a valid abscissas of a K-point mid-point rule, although every abscissa has 2^{d-1} repetitions. A 2-D example of this can be visualised as in Figure 4.29.

4.5.5 Convergence of UD and CUD quadratures

Lemma 2. *Let* M_K *denotes a* K*-point mid-point quadrature rule for 1-D functions. For integer* $z \geq 2$*,* φ_i *denotes an integrable function* $\varphi_i(x_i)$*, define*

$$\Lambda_K(\varphi_1, \prod_{j=2}^{z} \varphi_j) = (\varphi_1 - \mathrm{M}_K[\varphi_1]) \cdot \left(\prod_{j=2}^{z} \varphi_j - \prod_{j=2}^{z} \mathrm{M}_K[\varphi_j] \right)$$

then a UD quadrature rule on a product $\prod_{i=1}^{z} \varphi_i$ *can be expressed as*

$$\mathrm{Q}_K^{J_\alpha}\left[\prod_{i=1}^{z} \varphi_i\right] = \prod_{i=1}^{z} \mathrm{M}_K[\varphi_i] + \sum_{i=1}^{z-1} \left(\mathrm{Q}_K^{J_\alpha}\left[\Lambda_K(\varphi_i, \prod_{j=i+1}^{z} \varphi_j)\right] \prod_{j=1}^{i-1} \mathrm{M}_K[\varphi_j] \right)$$

Proof. By arithmetic re-arrangement, one has

$$\mathrm{Q}_K^{J_\alpha}[\varphi_1\varphi_2] = \mathrm{Q}_K^{J_\alpha}[\varphi_1]\mathrm{Q}_K^{J_\alpha}[\varphi_2] + \mathrm{Q}_K^{J_\alpha}[\Lambda_K(\varphi_1,\ \varphi_2)]$$

the proof is obtained by applying the below relation recursively for $s \geq 2$,

$$\mathrm{Q}_K^{J_\alpha}[\prod_{i=1}^{s} \varphi_i] = \mathrm{Q}_K^{J_\alpha}[\varphi_1] \cdot \mathrm{Q}_K^{J_\alpha}[\prod_{i=2}^{s} \varphi_i] + \mathrm{Q}_K^{J_\alpha}[\Lambda_K(\varphi_1,\ \prod_{i=2}^{s} \varphi_i)]$$

and the fact that for 1-D function φ_i,

$$\mathrm{Q}_K^{J_\alpha}[\varphi_i] = \mathrm{M}_K[\varphi_i]$$

□

Lemma 3. *For integer* $z \geq 2$*, a CUD quadrature rule on* $\prod_{i=1}^{z} \varphi_i$ *can be expressed as*

$$\mathrm{Q}_N^{C}\left[\prod_{i=1}^{z} \varphi_i\right] = \prod_{i=1}^{z} \mathrm{M}_K[\varphi_i] + \sum_{i=1}^{z-1} \left(\mathrm{Q}_N^{C}\left[\Lambda_K(\varphi_i, \prod_{j=i+1}^{z} \varphi_j)\right] \prod_{j=1}^{i-1} \mathrm{M}_K[\varphi_j] \right)$$

Proof. By the same reasoning as that for Lemma 2 □

Proposition 4. *A UD quadrature approximation of the splittable integration in Definition 1 can be expressed as*

$$\begin{aligned} \mathrm{Q}_K^{J_\alpha}[f] =& \mathrm{Q}_K^{J_\alpha}\left[\Psi(\phi_1, \phi_2, \cdots, \phi_d)\right] \\ =& \Psi(\mathrm{M}_K[\phi_1], \mathrm{M}_K[\phi_2] \cdots, \mathrm{M}_K[\phi_d]) + \sum_{B_t \in \mathcal{B}} \left[\gamma_t \sum_{i=1}^{z_t-1} \beta_{t,i}\ \mathrm{Q}_K^{J_\alpha}[\Lambda_K(\phi_{b_i}, \prod_{j=i+1}^{z_t} \phi_{b_j})] \right] \end{aligned} \tag{4.17}$$

where for every $B_t \in \mathcal{B}$*,* γ_t *is a constant,*

$$\beta_{t,i} = \prod_{k=1}^{i-1} \mathrm{M}_K[\phi_{b_k}]$$

Proof. Since for any $B_t \in \mathcal{B}$,

$$\mathrm{Q}_K^{J_\alpha}\left[\sum_{i=1}^{z_t} c_i \phi_{b_i}\right] = \sum_{i=1}^{z_t} c_i \mathrm{M}_K[\phi_{b_i}]$$

with c_i's constants, and by Lemma 2,

$$\mathrm{Q}_K^{J_\alpha}\left[\prod_{i=1}^{z_t} c_i \phi_{b_i}\right] = \prod_{i=1}^{z_t} c_i \mathrm{M}_K[\phi_{b_i}] + \prod_{i=1}^{z_t} c_i \sum_{i=1}^{z_t-1}\left(\mathrm{Q}_K^{J_\alpha}\left[\Lambda_K(\phi_{b_i}, \prod_{j=i+1}^{z_t} \phi_{b_j})\right]\prod_{k=1}^{i-1} \mathrm{M}_K[\phi_{b_k}]\right)$$

and the proof follows since Ψ is multilinear. □

Proposition 5. *A CUD quadrature approximation of the splittable integration in Definition 1 can be expressed as*

$$\begin{aligned}\mathrm{Q}_N^C[f] =& \mathrm{Q}_N^C\left[\Psi(\phi_1, \phi_2, \cdots, \phi_d)\right] \\ =& \Psi(\mathrm{M}_K[\phi_1], \mathrm{M}_K[\phi_2] \cdots, \mathrm{M}_K[\phi_d]) + \sum_{B_t \in \mathcal{B}}\left[\gamma_t \sum_{i=1}^{z_t-1} \beta_{t,i}\, \mathrm{Q}_K^C[\Lambda_K(\phi_{b_i}, \prod_{j=i+1}^{z_t} \phi_{b_j})]\right]\end{aligned} \tag{4.18}$$

Proof. By the same reasoning as that for Proposition 4 □

Lemma 4. *If $\varphi_i \in C^2[0,1]$ for $i = 1, 2, \cdots, d$, $z \le d$, $\mathbb{E}[\Lambda_K(\varphi_1, \prod_{i=2}^{z} \varphi_i)]|_{\boldsymbol{x} \in U_{J_\alpha}^d}$ converges to $\mathrm{cov}(\varphi_1, \prod_{i=2}^{z} \varphi_i)|_{\boldsymbol{x} \in U_{J_\alpha}^d}$ at a rate of order $\mathcal{O}(K^{-2})$.*

Proof.

$$\begin{aligned}&\mathbb{E}\left[\Lambda_K(\varphi_1, \prod_{i=2}^{z} \varphi_i)\right]\Big|_{\boldsymbol{x} \in U_{J_\alpha}^d} \\ &= \mathbb{E}\left[(\varphi_1 - \mathrm{M}_K[\varphi_1]) \cdot \left(\prod_{i=2}^{z} \varphi_i - \prod_{i=2}^{z} \mathrm{M}_K[\varphi_i]\right)\right]\Big|_{\boldsymbol{x} \in U_{J_\alpha}^d} \\ &= \mathrm{cov}(\varphi_1, \prod_{i=2}^{z} \varphi_i)|_{\boldsymbol{x} \in U_{J_\alpha}^d} + \sum_{i=1}^{z} c_i\, \epsilon_{M_K}(\varphi_i)\end{aligned} \tag{4.19}$$

where c_i's are constants with respect to K, and $\epsilon_{M_K}(\varphi_i) = \mathrm{M}_K[\varphi_i] - \mathbb{E}(\varphi_i)$. In the above derivation the relation $\mathbb{E}(\prod_{i=2}^{z} \varphi_i) = \prod_{i=2}^{z} \mathbb{E}(\varphi_i)$ is used due to the mutual independence of φ_i's. If $\varphi_i \in C^2[0,1]$, $\epsilon_{M_K}(\varphi_i)$ converges to zero at a rate of order $\mathcal{O}(K^{-2})$, and the proof follows.

□

Lemma 5. *If φ_i is of bounded variation for $i = 1, 2, \cdots, d$, $z \le d$, $\mathbb{E}[\Lambda_K(\varphi_1, \prod_{i=2}^{z} \varphi_i)]|_{\boldsymbol{x} \in U_{J_\alpha}^d}$ converges to $\mathrm{cov}(\varphi_1, \prod_{i=2}^{z} \varphi_i)|_{\boldsymbol{x} \in U_{J_\alpha}^d}$ at a rate of order $\mathcal{O}(K^{-1})$.*

Proof. The proof is the same as in Lemma 4 till equation (4.19). $\epsilon_{M_K}(\varphi_i)$ in this case can be bounded by Koksma-Hlawka inequality,

$$\epsilon_{M_K}(\varphi_i) \le V(\varphi_i) D^*(\boldsymbol{X}_{J_\alpha,K}^{(i)})$$

with $D^*(\cdot)$ denotes the star discrepancy and $V(\cdot)$ denotes the total variation. Since $\boldsymbol{X}^{(i)}_{J_\alpha,K} = \{\frac{2k-1}{2K} : k \in \mathbb{N}, k \leq K\}$, according to [97, Theorem 2.6],

$$D^*(\boldsymbol{X}^{(i)}_{J_\alpha,K}) = \frac{1}{2K}$$

This finishes the proof. □

Lemma 6. *If $\varphi_i \in C^2[0,1]$ for $i = 1, 2, \cdots, d$, $z \leq d$, $\mathbb{E}[\Lambda_K(\varphi_1, \prod_{i=2}^z \varphi_i]|_{\boldsymbol{x}\in U^d}$ converges to $\mathrm{cov}(\varphi_1, \prod_{i=2}^z \varphi_i)|_{\boldsymbol{x}\in U^d}$ at a rate of order $\mathcal{O}(K^{-2})$.*

Proof. Since

$$\mathbb{E}[\Lambda_K(\varphi_1, \prod_{i=2}^{z} \varphi_i)]|_{\boldsymbol{x}\in U^d} = \frac{1}{2^{d-1}} \sum^{J_\alpha \in \mathcal{J}^d} \mathbb{E}[\Lambda_K(\varphi_1, \prod_{i=2}^{z} \varphi_i)]|_{\boldsymbol{x}\in U^d_{J_\alpha}}$$

and

$$\mathrm{cov}(\varphi_1, \prod_{i=2}^{z} \varphi_i)|_{\boldsymbol{x}\in U^d} = \frac{1}{2^{d-1}} \sum^{J_\alpha \in \mathcal{J}^d} \mathrm{cov}(\varphi_1, \prod_{i=2}^{z} \varphi_i)|_{\boldsymbol{x}\in U^d_{J_\alpha}}$$

the proof directly follows Lemma 4. □

Lemma 7. *If φ_i is of bounded variation for $i = 1, 2, \cdots, d$, $z \leq d$, $\mathrm{Q}_K^{J_\alpha}[\Lambda_K(\varphi_1, \prod_{i=2}^z \varphi_i)]$ converges to $\mathbb{E}[\Lambda_K(\varphi_1, \prod_{i=2}^z \varphi_i)]|_{\boldsymbol{x}\in U^d_{J_\alpha}}$ at a rate of order $\mathcal{O}(K^{-1})$.*

Proof. On a SG, x_i's are functions of x_1, so one can write

$$\Lambda_K[\varphi_1(x_1), \prod_{i=2}^{z} \varphi_i(x_i)]|_{\boldsymbol{x}\in U^d_{J_\alpha}} = \Upsilon(x_1)$$

and

$$\mathrm{Q}_K^{J_\alpha}[\Upsilon(x_1)] = \mathrm{M}_K[\Upsilon(x_1)]$$

The error of $\mathrm{M}_K[\Upsilon]$ can be bounded by Koksma-Hlawka inequality,

$$|\mathrm{M}_K[\Upsilon] - \mathbb{E}[\Upsilon]| \leq V(\Upsilon) D^*(\boldsymbol{X}^{(1)}_{J_\alpha,K})$$

According to [97, Theorem 2.6],

$$D^*(\boldsymbol{X}^{(1)}_{J_\alpha,K}) = \frac{1}{2K}$$

This finishes the proof. □

Lemma 8. *If $\{\phi_i\}_{i=1}^d$ are all linear on $[0,1]$, $\mathrm{Q}_N^C[\Lambda_K(\phi_1(x_1), \prod_{i=2}^d \phi_i(x_i))] = 0$.*

Proof. Set $\phi_i(x_i) = a_i x_i + b_i$, $\mu_1 = \mathrm{M}_K[\phi_1]$ and $\mu_2 = \prod_{i=2}^d \mathrm{M}_K[\phi_i]$. Since mid-point rule integrates linear function exactly, $\mu_1 = \frac{a_1}{2} + b_1$, $\mu_2 = \prod_{i=2}^d (\frac{a_i}{2} + b_i)$, then

$$
\begin{aligned}
&\mathrm{Q}_N^C[\Lambda_K(\phi_1(x_1), \prod_{i=2}^d \phi_i(x_i))] \\
&= \frac{1}{2^{d-1}} \sum^{J_\alpha \in \mathcal{J}^d} \mathrm{Q}_K^{J_\alpha}[\Lambda_K(\phi_1(x_1), \prod_{i=2}^d \phi_i(x_i))] \\
&= \frac{1}{2^{d-1}} \sum^{J_\alpha \in \mathcal{J}^d} \frac{1}{K} \sum_{n=1}^K \Lambda_K(\phi_1(x_{1,n}), \prod_{i=2}^d \phi_i(x_{i,n})) \\
&= \frac{1}{2^{d-1}K} \sum^{J_\alpha \in \mathcal{J}^d} \sum_{n=1}^K \Big[(\phi_1(x_{1,n}) - \mu_1) \Big(\prod_{i=2}^d \phi_i(x_{i,n}) - \mu_2 \Big) \Big] \\
&= \frac{1}{2^{d-1}K} \sum_{n=1}^K \sum^{J_\alpha \in \mathcal{J}^d} \Big[(\phi_1(x_{1,n}) - \mu_1) \Big(\prod_{i=2}^d \phi_i(\lambda_{j_{i-1}^{(\alpha)}}(x_{i-1,n}, m_{i-1})) - \mu_2 \Big) \Big] \\
&= \frac{1}{2^{d-1}K} \sum_{n=1}^K \Big[(\phi_1(x_{1,n}) - \mu_1) \Big(\prod_{i=2}^d [\phi_i(\lambda_1(x_{i-1,n}, m_{i-1})) \\
&\qquad\qquad + \phi_i(\lambda_2(x_{i-1,n}, m_{i-1}))] - 2^{d-1}\mu_2 \Big) \Big] \\
&= \frac{1}{2^{d-1}K} \sum_{n=1}^K \Big[(\phi_1(x_{1,n}) - \mu_1) \Big(\prod_{i=2}^d [a_i + 2b_i] - 2^{d-1}\mu_2 \Big) \Big] \\
&= 0
\end{aligned}
$$

In the above derivation, the relation $\lambda_2(x, m) = 1 - \lambda_1(x, m)$ is used. □

Let $W^{k,p}$ denotes a Sobolev space, i.e,

$$W^{k,p} = \{f \in L^p[0,1] : \forall\, i \leq k, f^{(i)} \in L^p[0,1]\}$$

where $f^{(i)}$ is the i-th order derivative in a weak sense. One has the below lemmas involve $f \in W^{k,2}$.

Lemma 9. [15, Theorem 4.1.10] *For $k \in \mathbb{N}$ a continuous function f of period 1 belongs to $W^{k,2}$ if and only if*

$$\sum_{v=-\infty}^{\infty} |v|^{2k} \cdot |\mathfrak{c}_v|^2 \leq \infty$$

where $\{\mathfrak{c}_v\}_{v \in \mathbb{Z}}$ are the Fourier coefficients of f,

$$\mathfrak{c}_v = \int_0^1 f(x) e^{-\mathfrak{i} 2\pi v x} \mathrm{d}x, \quad \mathfrak{i} = \sqrt{-1}, \quad v \in \mathbb{Z}$$

Lemma 10. [110, Lemma 4] *The transformation*

$$d'_v = \sum_{j=1}^{\infty} \frac{d_{v\cdot j}}{j^k} \quad (k > 1/2)$$

maps every sequence $\{d_v\}_{v\in\mathbb{N}} \in l^2$ *into a sequence* $\{d'_v\}_{v\in\mathbb{N}} \in l^2$ *if and only if* $k > 1$.

Lemma 11. *For a continuous function* $f \in W^{k,2}$ *defined on* $[0,1]$ *and be of period 1, if* $k > 1$, *then*

$$\sum_{j=-\infty, j\neq 0}^{\infty} \mathfrak{c}_{v\cdot j} \sim \mathcal{O}(v^{-k})$$

Proof. Define

$$\mathfrak{a}_v = 2\int_0^1 f(x)\cos(2\pi vx)\mathrm{d}x$$

$$\mathfrak{b}_v = 2\int_0^1 f(x)\sin(2\pi vx)\mathrm{d}x$$

then it is clear $\mathfrak{c}_v = (\mathfrak{a}_v - \mathfrak{i}\mathfrak{b}_v)/2$ and $\mathfrak{c}_{-v} = (\mathfrak{a}_v + \mathfrak{i}\mathfrak{b}_v)/2$, by Lemma 9 one has $\mathfrak{a}_v = d_v \cdot v^{-k}$, with $\{d_v\}_{v\in\mathbb{N}} \in l^2$, then

$$\begin{aligned}\sum_{j=-\infty, j\neq 0}^{\infty} \mathfrak{c}_{v\cdot j} =& \sum_{j=1}^{\infty} \mathfrak{a}_{v\cdot j} \\ =& \sum_{j=1}^{\infty} \frac{d_{v\cdot j}}{j^k} v^{-k} \\ =& d'_v v^{-k}\end{aligned}$$

The proof follows that by Lemma 10 $\{d'_v\}_{v\in\mathbb{N}} \in l^2$. □

Lemma 12. [134, p. 31] *If the series*

$$f(x) = \sum_{v=-\infty}^{\infty} \mathfrak{c}_v e^{\mathrm{i}2\pi vx}$$

converges for $x \in [0,1]$, *then the error of a* K*-point mid-point rule quadrature approximation of* f *is*

$$|\mathbb{E}[f] - \mathrm{M}_K[f]| = \sum_{j=-\infty, j\neq 0}^{\infty} (-1)^j \mathfrak{c}_{j\cdot K}$$

Lemma 13. *For any* $J_\alpha \in \mathcal{J}^d$, *if* $\varphi \in C^2[0,1]$, $\chi(x_i) = \varphi(\lambda_1(x_i, m)) + \varphi(\lambda_2(x_i, m))$, *and* $\hat{\chi}(x_1) = \chi\big(\boldsymbol{\lambda}_{J_\alpha, 1\to i}(x_1, \boldsymbol{m})\big)$, *then* $\hat{\chi}(x_1) \in W^{2,p}$.

Proof.

$$\chi'(x_i) = \frac{\partial \lambda_1}{\partial x_i}[\varphi'(\lambda_1) - \varphi'(1-\lambda_1)] \tag{4.20}$$

By its definition it is easy to see $\chi(x_i)$ is continuous with respect to x_i, and by (4.20) its first derivative, $\chi'(x_i)$, has discontinuities only at $x_i = j/m, j \in \mathbb{N}, j \leq m$, and is piece-wise continuous. In turn it can be seen that $\hat{\chi}(x_1)$ is also continuous with respect to x_1, and $\hat{\chi}'(x_1)$ has discontinuities only at $x_1 = x_1^*$, with $j/m = \boldsymbol{\lambda}_{J_\alpha, 1\to i}(x_1^*, \boldsymbol{m})$, and $\hat{\chi}'(x_1)$ is piece-wise continuous. So $\hat{\chi}''(x_1)$ is bounded almost everywhere except at x_*'s. This proves $\hat{\chi}(x_1) \in W^{2,p}$.

□

Lemma 14. *If $\phi_i \in C^2[0,1]$ for $i = 1, 2, \cdots, d$, $\mathrm{Q}_N^C[\Lambda_K(\phi_1(x_1), \prod_{t=2}^d \phi_t(x_t))]$ converges to $\mathbb{E}[\Lambda_K(\phi_1(x_1), \prod_{t=2}^d \phi_t(x_t))]|_{\boldsymbol{x}\in U^d}$ at a rate of order $\mathcal{O}(K^{-2})$.*

Proof. Write $\mu_1 = \mathrm{M}_K[\phi_1]$ and $\mu_2 = \prod_{t=2}^d \mathrm{M}_K[\phi_t]$, define

$$\begin{aligned}
G(x_1) &= \Lambda_K(\phi_1(x_1), \prod_{t=2}^d \phi_t(x_t))|_{\boldsymbol{x}\in U^d} \\
&= \frac{1}{2^{d-1}} \sum^{J_\alpha \in \mathcal{J}^d} \Lambda_K(\phi_1(x_1), \prod_{t=2}^d \phi_t(x_t))|_{\boldsymbol{x}\in U^d_{J_\alpha}} \\
&= \frac{1}{2^{d-1}} \sum^{J_\alpha \in \mathcal{J}^d} (\phi_1(x_1) - \mu_1)(\prod_{t=2}^d \phi_t(\lambda_{j_{t-1}^{(\alpha)}}(x_{t-1}, m_t)) - \mu_2) \\
&= \frac{1}{2^{d-1}} (\phi_1(x_1) - \mu_1)(\prod_{t=2}^d [\phi_t(\lambda_1(x_{t-1}, m_t)) + \phi_t(\lambda_2(x_{t-1}, m_t))] - 2^{d-1}\mu_2) \\
&= \frac{1}{2^{d-1}} (\phi_1(x_1) - \mu_1)(\prod_{t=2}^d \chi_t(x_{t-1}) - 2^{d-1}\mu_2) \\
&= \frac{1}{2^{d-1}} (\phi_1(x_1) - \mu_1)(\prod_{t=2}^d \hat{\chi}_t(x_1) - 2^{d-1}\mu_2) \\
&= g_1(x_1) g_2(x_1)
\end{aligned}$$

where $g_1(x_1) = \frac{1}{2^{d-1}}(\phi_1(x_1) - \mu_1)$ and $g_2(x_1) = \prod_{t=2}^d \hat{\chi}_t(x_1) - 2^{d-1}\mu_2$. One has $g_1 \in C^2$, and by Lemma 13, $g_2 \in W^{2,2}$, also notice that g_2 is a periodic function on $[0,1]$ with $g_2(0) = g_2(1)$.

Define $\{\mathfrak{c}_\nu^G\}_{\nu\in\mathbb{Z}}$ and $\{\mathfrak{c}_\nu^{g_2}\}_{\nu\in\mathbb{Z}}$ as the Fourier coefficients of $G(x_1)$ and $g_2(x_1)$ respectively. Since both $G(x_1)$ and $g_2(x_1)$ are continuous, $\{\mathfrak{c}_\nu^G\}_{\nu\in\mathbb{Z}}$ and $\{\mathfrak{c}_\nu^{g_2}\}_{\nu\in\mathbb{Z}}$ are convergent, and

$$\mathfrak{c}_\nu^G \leq \mathfrak{c}_\nu^{g_2} \int_0^1 \max_{x\in[0,1]}[g_1(x)]\mathrm{d}x \tag{4.21}$$

Since $g_2 \in W^{2,2}$ and is periodic on $[0,1]$, according to Lemma 11, $\mathfrak{c}_\nu^{g_2} \sim \mathcal{O}(\nu^{-2})$, and (4.21) shows so is $\mathfrak{c}_\nu^G$, i.e.,

$$\mathfrak{c}_\nu^G \sim \mathcal{O}(\nu^{-2}) \tag{4.22}$$

By the definition and properties of Q_N^C, one has

$$\mathrm{Q}_N^C[\Lambda_K(\phi_1(x_1), \prod_{t=2}^{d} \phi_t(x_t))] = \mathrm{M}_K[G(x_1)]$$

and by Lemma 12, one has

$$|\mathbb{E}[G(x_1)] - \mathrm{M}_K[G(x_1)]| = \sum_{j=-\infty, j\neq 0}^{\infty} (-1)^j \mathfrak{c}_{j\cdot K}^G$$

this together with (4.22) finish the proof. □

Finally, these lemmas are combined into propositions about the convergence rate of UD and CUD quadratures.

Proposition 6. *If f is dimension-splittable and for $i = 1, 2, \cdots, d$, ϕ_i is of bounded variation, $\mathrm{Q}_K^{J_\alpha}[f]$ converges to $\mathbb{E}[f]$ at a rate of order $\mathcal{O}(K^{-1} + \min(\boldsymbol{m})^{-1})$.*

Proof. By comparing Proposition 1 and Proposition 4 it is clear $|\mathrm{Q}_K^{J_\alpha}[f] - \mathbb{E}[f]|$ is a linear combination of the errors of $\mathrm{M}_K[\phi_i]$ and $\mathrm{Q}_K^{J_\alpha}[\Lambda_K]$. Similar to the argument in Lemma 7,

$$|\mathrm{M}_K[\phi_i] - \mathbb{E}[\phi_i]| \leq V(\phi_i) D^*(\mathcal{X}_{J_\alpha, K}^{(i)}) = V(\phi_i) \cdot \frac{1}{2K}$$

And for any $B_t \in \mathcal{B}$, based on Lemma 5 and Lemma 7,

$$|\mathrm{Q}_K^{J_\alpha}[\Lambda_K(\phi_{b_i}, \prod_{j=i+1}^{z_t} \phi_{b_j})] - \mathrm{cov}(\phi_{b_i}, \prod_{j=i+1}^{z_t} \phi_j)|_{\boldsymbol{x}\in U_{J_\alpha}^d} \sim \mathcal{O}(K^{-1})$$

while by Corollary 1,

$$\mathrm{cov}(\phi_{b_i}, \prod_{j=1+1}^{z_t} \phi_j)|_{\boldsymbol{x}\in U_{J_\alpha}^d} \sim \mathcal{O}(\min(\boldsymbol{m})^{-1})$$

These together with Proposition 1 and Proposition 4 finish the proof. □

Proposition 7. *If f is dimension-splittable and for $i = 1, 2, \cdots, d$, $\phi_i \in C^2[0,1]$, $\mathrm{Q}_N^C[f]$ converges to $\mathbb{E}[f]$ at a rate of order $\mathcal{O}(K^{-2} + \min(\boldsymbol{m})^{-1})$*

Proof. By comparing Proposition 1 and Proposition 5 it is clear $|\mathrm{Q}_N^C[f] - \mathbb{E}[f]|$ is a linear combination of the errors of $\mathrm{M}_K[\phi_i]$ and $\mathrm{Q}_N^C[\Lambda_K]$. For $i = 1, 2, \cdots, d$, one has

$$|\mathrm{M}_K[\phi_i] - \mathbb{E}[\phi_i]| \sim \mathcal{O}(K^{-2})$$

And for any $B_t \in \mathcal{B}$, based on Lemma 6 and Lemma 14,

$$|\mathrm{Q}_N^C[\Lambda_K(\phi_{b_i}, \prod_{j=i+1}^{z_t} \phi_{b_j})] - \mathrm{cov}(\phi_{b_i}, \prod_{j=i+1}^{z_t} \phi_j)|_{\boldsymbol{x}\in U^d} \sim \mathcal{O}(K^{-2})$$

while by Corollary 2,

$$\mathrm{cov}(\phi_{b_i}, \prod_{j=i+1}^{z_t} \phi_j)|_{\boldsymbol{x}\in U^d} \sim \mathcal{O}(\min(\boldsymbol{m})^{-1})$$

These together with Proposition 1 and Proposition 5 finish the proof. □

Proposition 8. *If f is dimension-splittable and $\{\phi_i\}_{i=1}^d$ are all linear, $\mathrm{Q}_N^C[f] = \mathbb{E}[f]$.*

Proof. If $\{\phi_i\}_{i=1}^d$ are all linear, for $i = 1, 2, \cdots, d$,

$$\mathrm{M}_K[\phi_i] = \mathbb{E}[\phi_i]$$

and for any $B_t \in \mathcal{B}$, by Lemma 8,

$$\mathrm{Q}_N^C[\Lambda_K(\phi_{b_i}, \prod_{j=i+1}^{z} \phi_{b_j})] = 0 = C_{t,i}$$

These together with Proposition 1 and Proposition 5 finish the proof. □

4.5.6 Good $\boldsymbol{m}$ values

$\boldsymbol{m}$ values need more detailed discussion at this stage. Good $\boldsymbol{m}$ values should possess such properties:

1. Making abscissas simultaneously uniform on each dimension.
2. Minimising the sampled $C_{t,i}$.
3. Being large so that $\min(\boldsymbol{m})^{-1}$ is of at most the same order of the error of $\mathrm{M}_K[\phi_i]$.

Proposition 3 gives a sufficient condition of $\boldsymbol{m}$ for the first property, but not a necessary condition, i.e., good $\boldsymbol{m}$'s are not confined to prime numbers.

To illustrate the necessity of the second property, Figure 4.30 shows the error of $\mathrm{Q}_{30}^{J_1}[\sin(x_1)\exp(x_2)]$, $K = 30$ using different m_1 values all of which are prime numbers inbetween 10000 and 10500 fulfilling the condition requested in Proposition 3, each label beside a data point indicates the associated m_1 value. It can be seen these m_1 values result in very different accuracies for the same K number. A *good* m_1 value minimises the integration error by making $\boldsymbol{X}_{J_1,30}$ well scattered so that $\boldsymbol{X}_{J_1,30}^{(1)}$ and $\boldsymbol{X}_{J_1,30}^{(2)}$ are less correlated, as shown in Figure 4.31, while a *bad* m_1 value makes an otherwise scenario, as shown in Figure 4.32.

The third property is easy to make, prescribing a large $\boldsymbol{m}$ costs no extra effort. By Proposition 6 and Proposition 7, it is clear if such an $\boldsymbol{m}$ is prescribed, the convergence rate of UD and CUD quadratures are virtually $\mathcal{O}(N^{-1})$ and $\mathcal{O}(N^{-2})$ respectively.

Good $\boldsymbol{m}$ values in this work are obtained for each K by exhaustive searches in the range $[10^8, 10^8 + 2K]$ for the $\boldsymbol{m}$ that minimises the average normalised error of integrations of the below 3 functions,

$$f_1 = \prod_{i=1}^{d} x_i \ , \qquad f_2 = \prod_{i=1}^{d} x_i^2 \ , \qquad f_3 = \prod_{i=1}^{d} \sin(x_i)$$

Since minimising error of integrations implies the first two properties, and 10^{-8} is considered smaller than the order of tolerated errors in this work. These good $\boldsymbol{m}$ values for a selected sequence of K numbers for UD or CUD quadrature are tabulated in Appendix B.

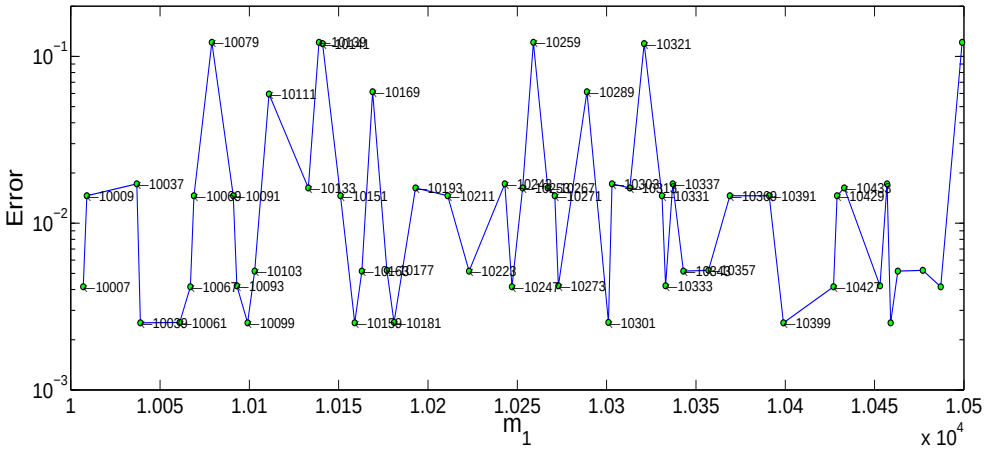

Figure 4.30: Error along m_1 values

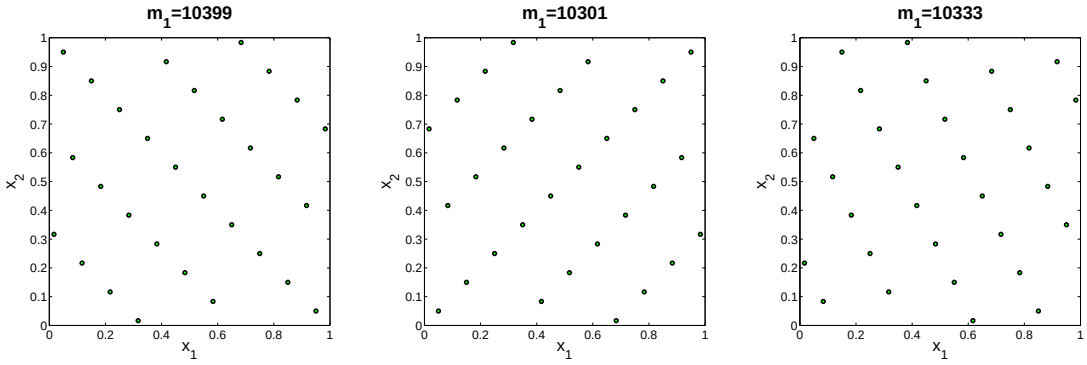

Figure 4.31: $\boldsymbol{X}_{J_1,30}$ from three good m_1 values

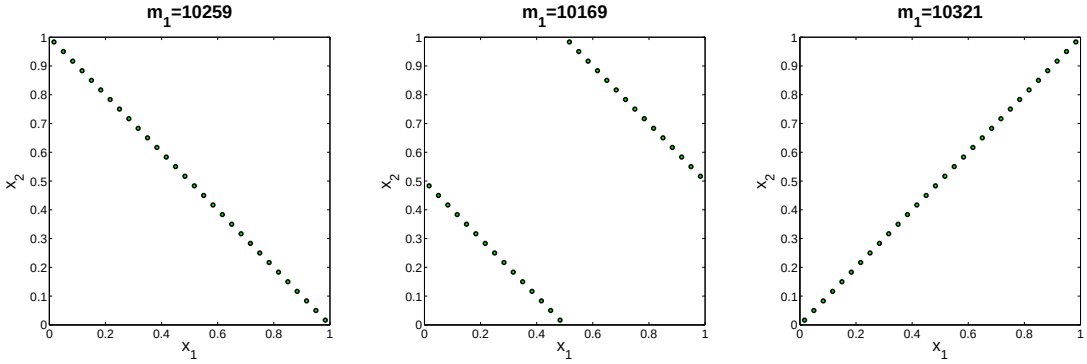

Figure 4.32: $\boldsymbol{X}_{J_1,30}$ from three bad m_1 values

4.5.7 Discussion

As discussed in the last section, if $\boldsymbol{m}$ is prescribed large enough, the convergence rate of UD and CUD quadratures are virtually $\mathcal{O}(N^{-1})$ and $\mathcal{O}(N^{-2})$ respectively, regardless to the number of dimensions. This is a significant improvement to the numerical integration techniques whose convergence rate more or less deteriorate at higher number of dimensions. Besides the exploitation of the special property of splittable multidimensional integrations, what is the rationale for this superiority?

Proposition 1 provides a new viewing angle to watch the behaviours of some numerical integration techniques, and can bring new understandings of them. If $\boldsymbol{X}$ denotes the abscissas of the sample points,

$$\boldsymbol{X} = \{(x_{1,n}, \cdots, x_{d,n}) \ : \ n \in \mathbb{N}, n \leq N\}$$

and $\boldsymbol{X}^{(i)}$ denotes the projection of $\boldsymbol{X}$ on the i-th dimension,

$$\boldsymbol{X}^{(i)} = \{x_{i,n} \ : \ n \in \mathbb{N}, n \leq N\}, \ \text{ for } i = 1, 2, \cdots, d$$

From there it is seen the sample points of a *good* integration technique should be such arranged that the following two aims are achieved,

1. $\boldsymbol{X}^{(i)}$'s should be simultaneously unbiased samples on each dimension.

2. The sampled $C_{t,i}$ should converge to zero, i.e. the correlationship of the sampled $\phi_{b_i}(\boldsymbol{X}^{(b_i)})$ and $\prod_{j=i+1}^{z_t} \phi_{b_j}(\boldsymbol{X}^{(b_j)})$ should be minimised.

Some existing techniques persue the aim 2 by persuing mutual independence of $\boldsymbol{X}^{(i)}$'s, i.e., for any (i, j) pair, mutual independence of $\boldsymbol{X}^{(i)}$ and $\boldsymbol{X}^{(j)}$ yields independence of $\phi_i(\boldsymbol{X}^{(i)})$ and $\phi_j(\boldsymbol{X}^{(j)})$ which in turn generates uncorrelatedness of ϕ_{b_i} and $\prod_{j=i+1}^{z_t} \phi_{b_j}$.

Tensor product quadratures work on aim 2 much better than on aim 1, their way of sampling makes $\boldsymbol{X}^{(i)}$ and $\boldsymbol{X}^{(j)}$ achieve a sampled independence for any sample number $N = k^d, \ k \in \mathbb{N}, k \geq 2$. This is efficient to make $C_{t,i}$ converge, but sacrifices the efficiency on aim 1, since N such samples has only $N^{\frac{1}{d}}$ projections on each dimension. Sparse grid quadratures are linear combinations of sparser tensor product quadratures, by compromising its efficiency on aim 2 to the one on aim 1, it has a better balance in its effort on the two aims. QMC method tries to lower the discrepancy of samples, while zero discrepancy by its definition equals mutual independence of $\boldsymbol{X}^{(i)}$'s. MC methods achieve both the two aims by the Law of Large Numbers.

Persuing independence for the mere aim of uncorrelatedness perhaps undermine the efficiency of some techniques. The CUD and UD quadratures persue directly uncorrelatedness, this seems the major source of its advantage.

4.5.8 Numerical experiments on test functions

Numerical tests are performed for UD and CUD quadratures for dimension number 3, 6 and 9, using the test functions proposed by Genz [41] together with a multilinear test function. This package includes 8 functions defined on $[0,1]^d$ as tabulated in Table 4.1. For each function, 20 instances are created by independently generating uniform distributed random unaffective and affective parameters u_i and a_i in $[0,1]^d$. The vector $\boldsymbol{a} = (a_1, \cdots, a_d)$ of affective parameters is then scaled such that $\|\boldsymbol{a}\|_1$ meets the required difficulty specified in Table 4.1.

Integrands	$\|\boldsymbol{a}\|_1$	Attribute
$f_1(\boldsymbol{x}) = \cos\left(2\pi u_1 + \sum_{i=1}^{d} a_i x_i\right)$	$\frac{110}{\sqrt{d^3}}$	Oscillatory
$f_2(\boldsymbol{x}) = \prod_{i=1}^{d} \frac{1}{a_i^{-2} + (x_i - u_i)^2}$	$\frac{600}{d^2}$	Product peak
$f_3(\boldsymbol{x}) = \left(1 + \sum_{i=1}^{d} a_i x_i\right)^{-(d+1)}$	$\frac{600}{d^2}$	Corner peak
$f_3'(\boldsymbol{x}) = f_3(\boldsymbol{x})$	$\frac{10}{d^2}$	Corner peak
$f_4(\boldsymbol{x}) = \exp\left(-\sum_{i=1}^{d} a_i^2 (x_i - u_i)^2\right)$	$\frac{100}{d}$	Gaussian
$f_5(\boldsymbol{x}) = \exp\left(-\sum_{i=1}^{d} a_i \lvert x_i - u_i\rvert\right)$	$\frac{150}{d^2}$	C^0 function
$f_6(\boldsymbol{x}) = \begin{cases} 0 & \text{if } x_1 > u_1 \vee x_2 > u_2 \\ \exp\left(\sum_{i=1}^{d} a_i x_i\right) & \text{otherwise} \end{cases}$	$\frac{100}{d^2}$	Discontinuous
$f_7(\boldsymbol{x}) = \sum_{i=1}^{d} x_i + \prod_{i=1}^{d} x_i$	–	Multilinear

Table 4.1: Test integrands (f_1–f_6 from Genz's test integrand families)

For each instance $k = 1, \cdots, 20$ of an integrand $j = 1, \cdots, 8$, the normalised error $\epsilon_{j,k}$ is calculated by the formula

$$\epsilon_{j,k} = \frac{|\mathbb{E}[f_{j,k}] - \mathrm{Q}[f_{j,k}]|}{\frac{1}{20}\sum_{i=1}^{20} |\mathbb{E}[f_{j,i}]|}$$

Then the normalised mean error ϵ_j is obtained by

$$\epsilon_j = \frac{1}{20} \sum_{k=1}^{20} \epsilon_{j,k}$$

Results of the experiments are shown in Figure 4.33 to Figure 4.40.

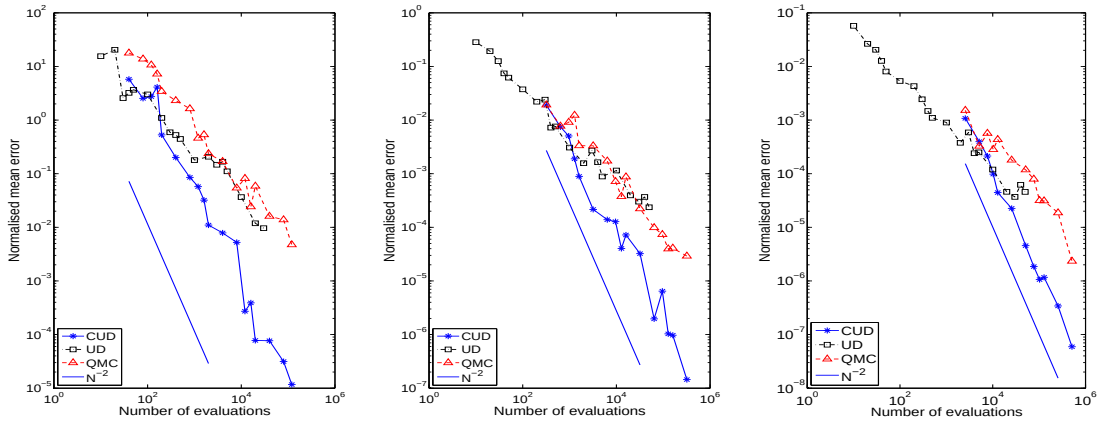

Figure 4.33: On integrand f_1 with $d = 3$ (left), $d = 6$ (middle), $d = 9$ (right)

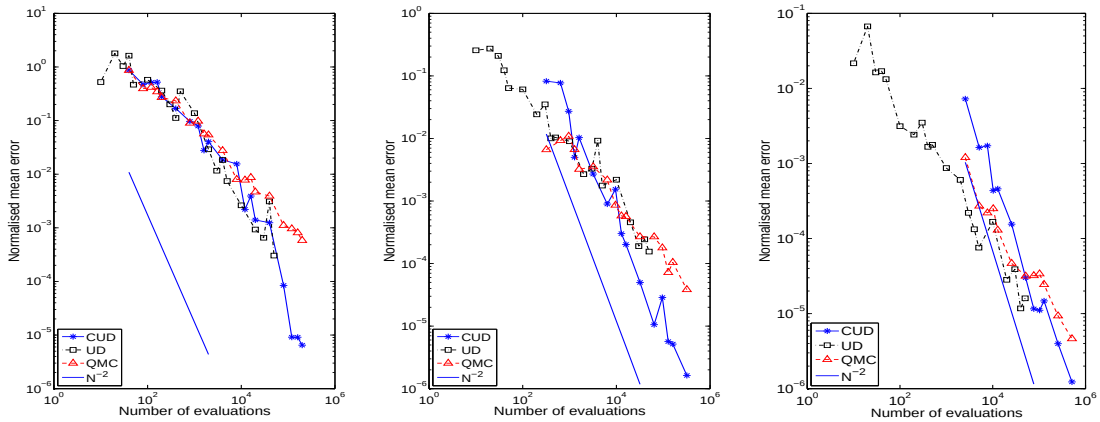

Figure 4.34: On integrand f_2 with $d = 3$ (left), $d = 6$ (middle), $d = 9$ (right)

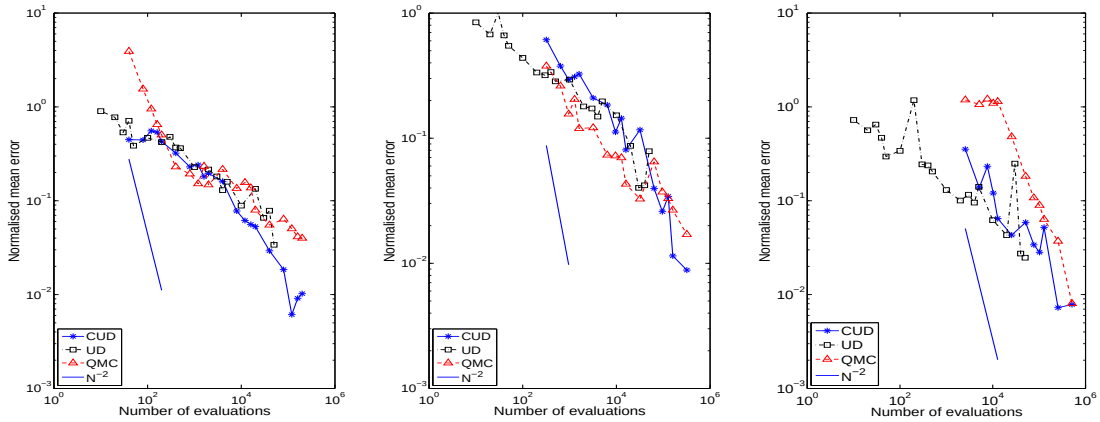

Figure 4.35: On integrand f_3 with $d = 3$ (left), $d = 6$ (middle), $d = 9$ (right)

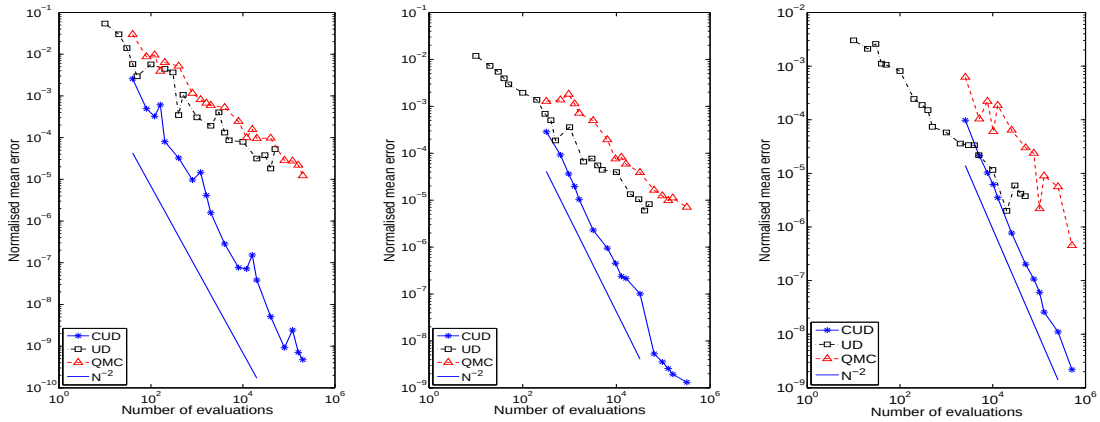

Figure 4.36: On integrand f_3' with $d = 3$ (left), $d = 6$ (middle), $d = 9$ (right)

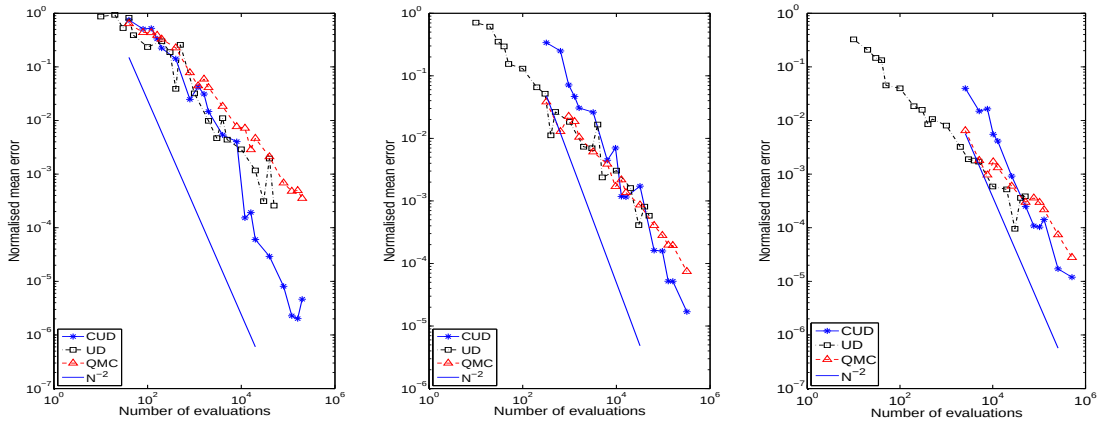

Figure 4.37: On integrand f_4 with $d = 3$ (left), $d = 6$ (middle), $d = 9$ (right)

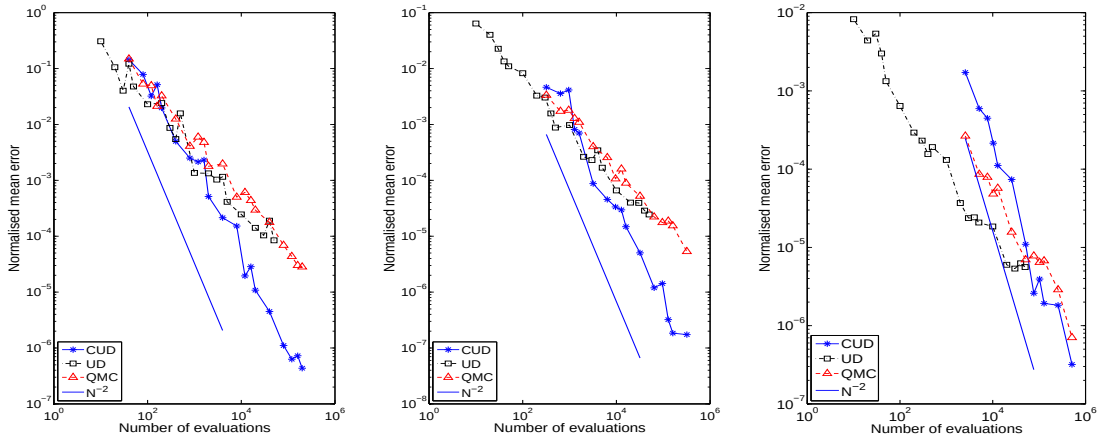

Figure 4.38: On integrand f_5 with $d = 3$ (left), $d = 6$ (middle), $d = 9$ (right)

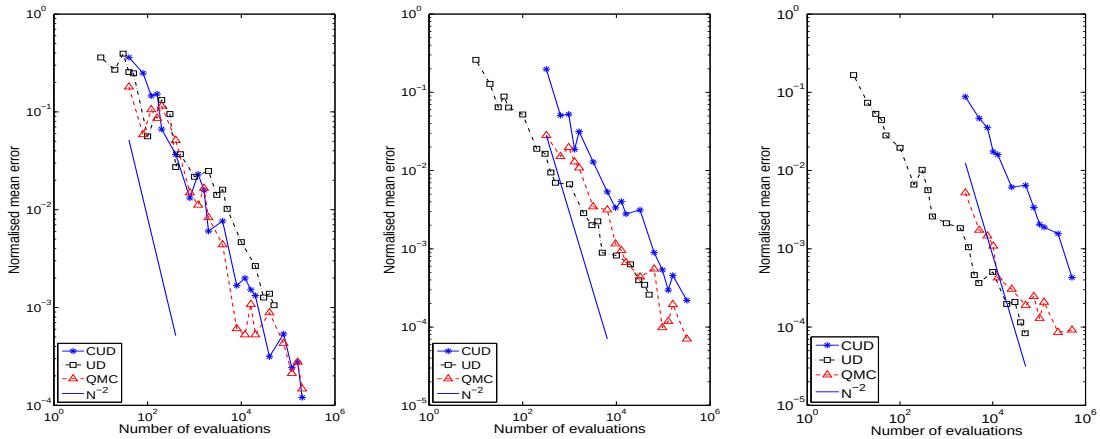

Figure 4.39: On integrand f_6 with $d = 3$ (left), $d = 6$ (middle), $d = 9$ (right)

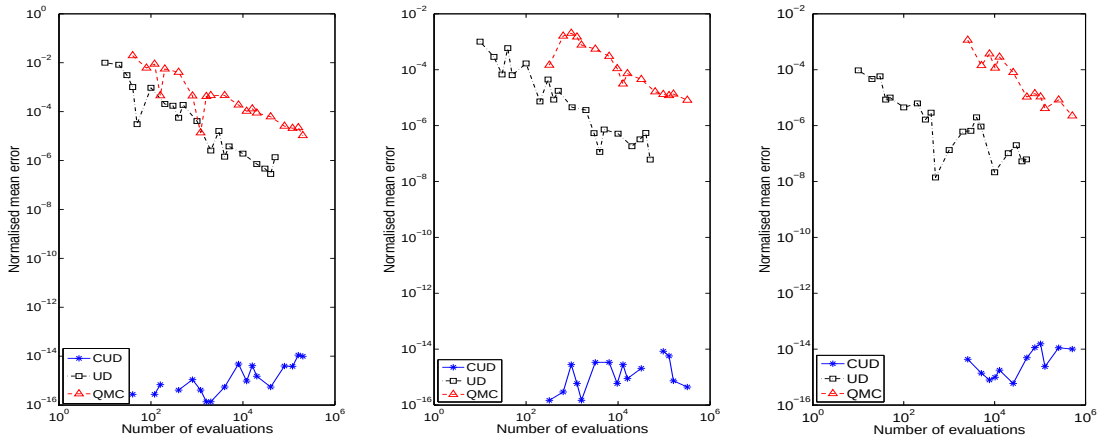

Figure 4.40: On integrand f_7 with $d = 3$ (left), $d = 6$ (middle), $d = 9$ (right)

The results show that on continuous integrands f_1, f_2, f_3', f_4 and f_5, CUD quadrature displays a $\mathcal{O}(N^{-2})$ convergence rate, seems irrelevant to the d number. This hints the condition $f \in C^2$ required in Proposition 7 is sufficient but not necessary and can be released to some degree. The integrand f_3 has sharp peaks so that requires larger N to display the asymptotic convergence rate. On discontinuous integrands f_6 CUD quadrature shows a $\mathcal{O}(N^{-1})$ convergence rate, and performs worse than UD and QMC, especially on higher dimension cases. This is because it loses its advantage on eliminating Λ term in this case and its 2^{d-1} repetitions of 1-D abscissas makes it inferior to UD quadrature in the 1-D integrations. The results also show that on multilinear integrands the CUD quadrature's error is at the same order of the round-off error of the machine, which conforms with the theoretical analysis about its exactness in this situation.

UD quadrature presents a $\mathcal{O}(N^{-1})$ convergence rate on most integrands except f_3 which has sharp peaks, again seems irrelevant to the d number. It is believed by the author that if larger N was used, $\mathcal{O}(N^{-1})$ rates would also show up on f_3. UD quadrature outperforms CUD one on the 9-D continuous integrands when N is relatively small, this is due to the 2^{d-1} repetitions of abscissas of CUD quadrature. UD quadrature shows an advantage over QMC quadrature and it seems the advantage is larger in higher dimensional cases.

4.5.9 For Integrand with Gaussian distributed variables

Up to now the integrands involved are all with uniformly distributed variables. On a domain with a Gaussian weight function, an equal-weight mid-point quadrature produces abscissas that are not equally distanced, and the intervals inbetween the abscissas do not converge at the rate $\mathcal{O}(N^{-1})$ as they do on integrands with uniform weight functions, so this quadrature on integrands with Gaussian variables does not converge at the rate $\mathcal{O}(N^{-2})$, neither does CUD quadrature. Numerical experiments show in this case the convergence rate of CUD quadrature for integrands belongs to C^2 is $\mathcal{O}(N^{-a})$ with a slightly larger than 1.

The convergence rate of UD quadrature is still $\mathcal{O}(N^{-1})$ for integrands in Gaussian variables and with bounded variations, since UD quadrature exploits the 1-D low discrepancy of its abscissas which is not altered by the change in the distribution of variables. Taking the 2^{d-1} repetitions of CUD quadrature's abscissas into consideration, UD quadrature is more favoured on integrands with Gaussian distributed variables.

4.5.10 Numerical results on the model

Because the stochastic SWE model has its variables Gaussian distributed, UD quadrature is chosen for the numerical integration. The $\boldsymbol{m}$ is prescribed for each K number according to Appendix B with all its elements larger than 10^8. The average errors of these integrations along the number of model evaluations, together with those of a QMC quadrature using Niederreiter sequence, are shown in Figure 4.41 to 4.49. The average is made over the three gauge points.

The results show UD quadrature outperforms QMC quadrature on estimating mean values, but on estimating variance and exceedance probabilities its advantage

is slight or not obvious. It seems UD quadrature converges at a rate slightly worse than $\mathcal{O}(N^{-1})$, the reason might be that the integration of this model cannot be categorised as a SMI.

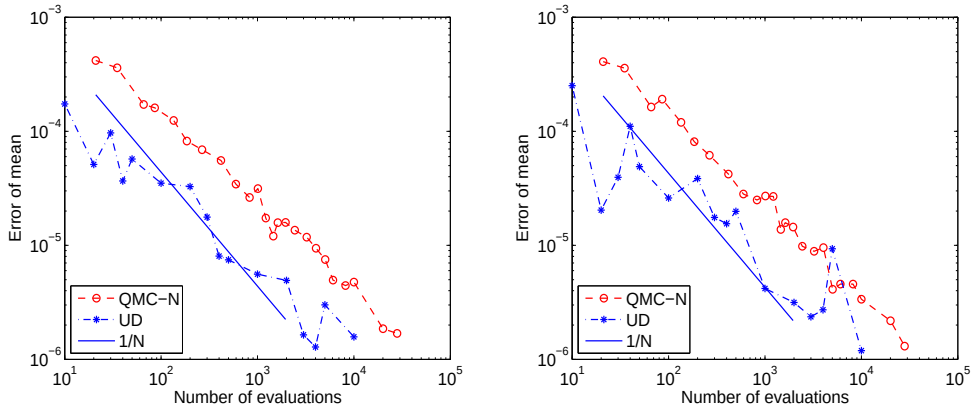

Figure 4.41: Average error of $\mu_{h_{\max}}$ (left) and $\mu_{h_{30}}$ (right), with $d = 3$

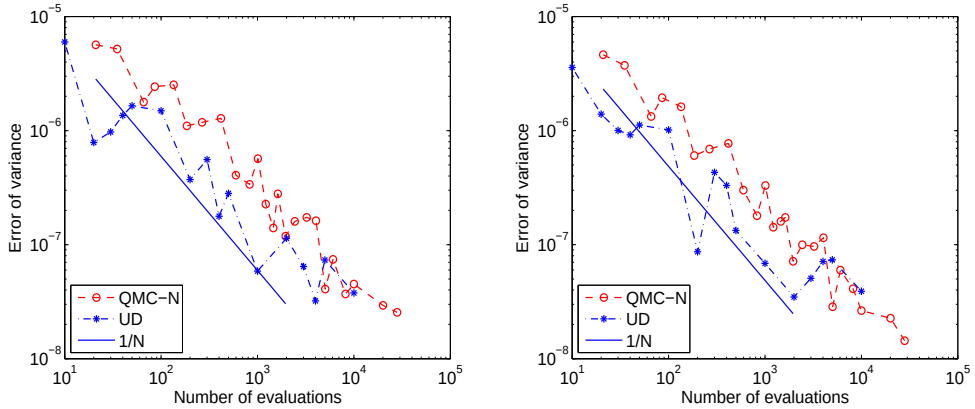

Figure 4.42: Average error of $\sigma^2_{h_{\max}}$ (left) and $\sigma^2_{h_{30}}$ (right), with $d = 3$

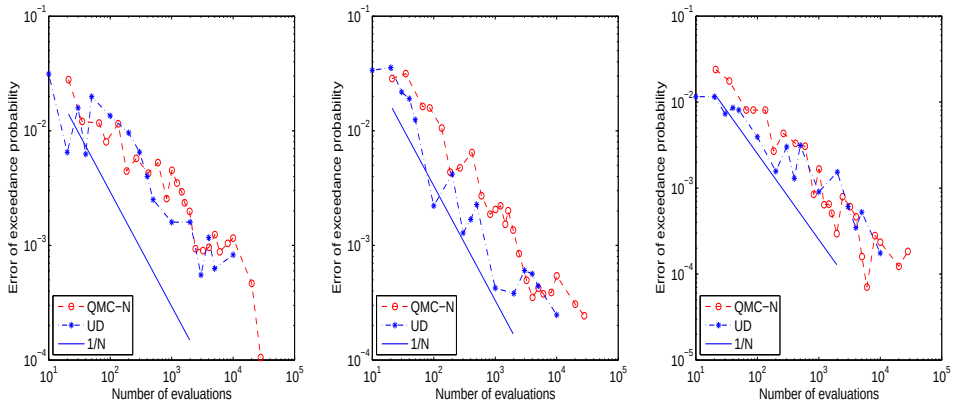

Figure 4.43: Average error of $P_{h_{\max},1}$, $P_{h_{\max},2}$ and $P_{h_{\max},3}$ with $d = 3$

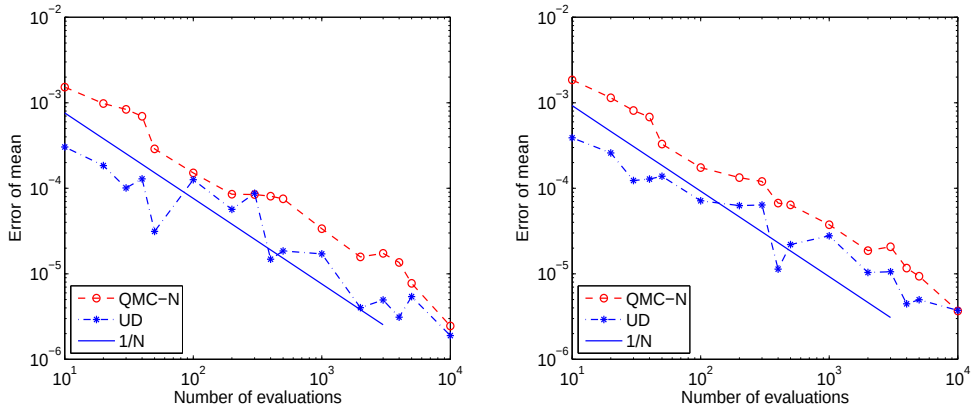

Figure 4.44: Average error of $\mu_{h_{\max}}$ (left) and $\mu_{h_{30}}$ (right), with $d = 6$

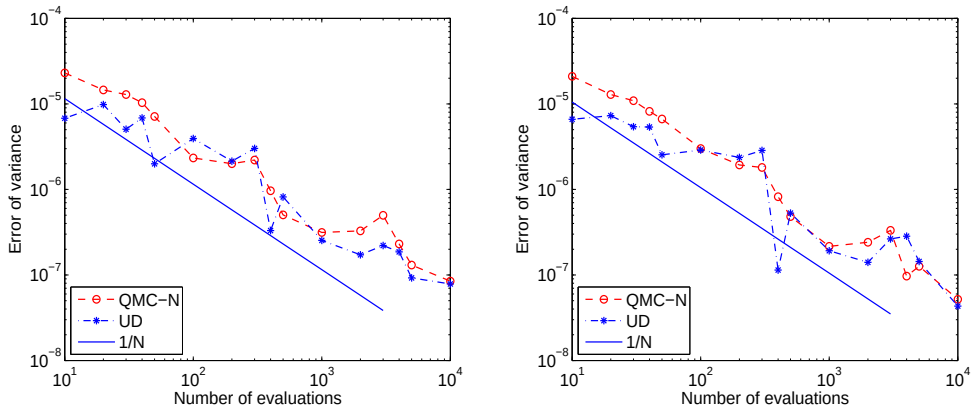

Figure 4.45: Average error of $\sigma^2_{h_{\max}}$ (left) and $\sigma^2_{h_{30}}$ (right), with $d = 6$

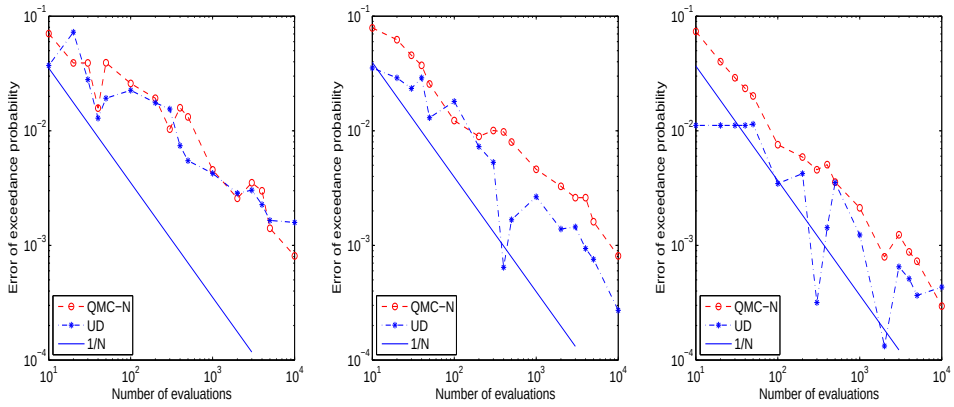

Figure 4.46: Average error of $P_{h_{\max},1}$, $P_{h_{\max},2}$ and $P_{h_{\max},3}$ with $d = 6$

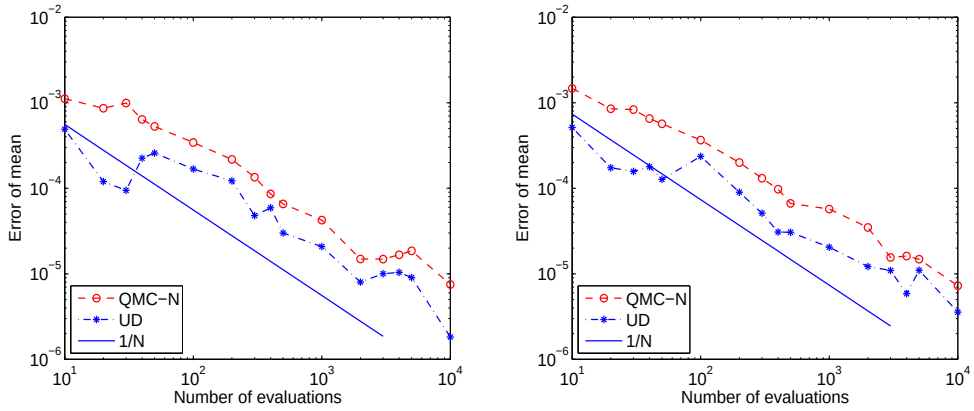

Figure 4.47: Average error of $\mu_{h_{\max}}$ (left) and $\mu_{h_{30}}$ (right), with $d = 9$

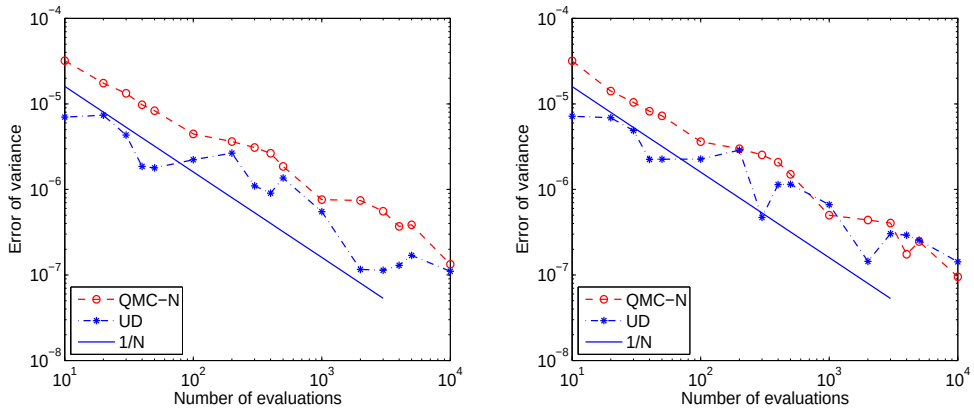

Figure 4.48: Average error of $\sigma^2_{h_{\max}}$ (left) and $\sigma^2_{h_{30}}$ (right), with $d = 9$

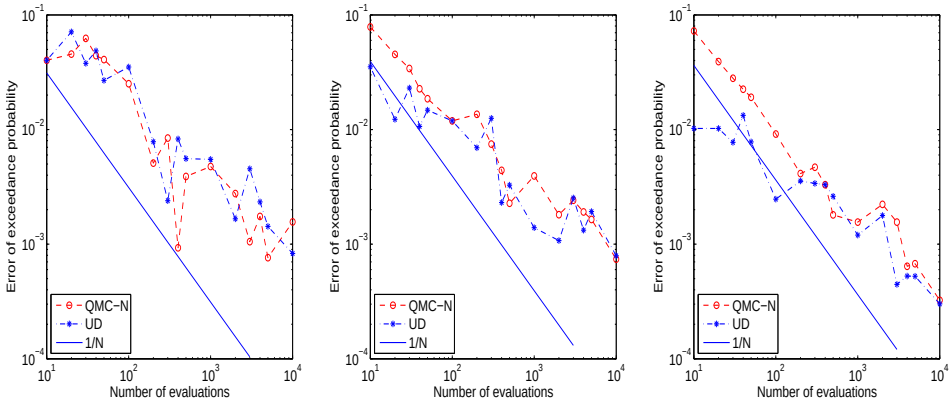

Figure 4.49: Average error of $P_{h_{\max},1}$, $P_{h_{\max},2}$ and $P_{h_{\max},3}$ with $d = 9$

4.6 Conclusions

In this chapter, some numerical integration techniques are compared in term of efficiency, and two novel techniques are introduced.

Uncorrelated dimensions (UD) quadrature and compound uncorrelated dimensions (CUD) quadrature are new techniques originally developped in this work. These techniques pursue uncorrelatedness in the sampled contributions from each dimension, for an integrand f that can be expressed in a multilinear functional of any integrable functions, they have convergence rate independent of the number of dimensions. I.e., if a such f is with bounded variation, UD quadrature has a convergence rate $\mathcal{O}(N^{-1})$; if $f \in C^2$ with uniformly distributed variables, CUD quadrature converges at a rate $\mathcal{O}(N^{-2})$; if $f \in C^2$ with Gaussian variables the convergence rate of CUD is slightly better than $\mathcal{O}(N^{-1})$.

Five numerical integration techniques, i.e. sparse Gauss-Hermite (SGH) quadrature, sparse linear finite element method (SLFEM), Monte Carlo (MC), quasi-Monte Carlo (QMC) and UD quadrature, are applied on the integrations for statistics of the stochastic SWE model. UD and QMC quadratures outperform others in term of efficiency. SGH quadrature shows no convergence due to the low regularity of the model. SLFEM provides a linear approximation of the model, integrations based on it is less efficient than that of UD, QMC and MC quadratures.

Chapter 5

Stochastic Spectral Approximation

There are many reasons to approximate a complex model by a simpler analytical representation, e.g., for data compressions, for faster evaluations or exploration of the model. In this chapter polynomial chaos and KLE approximations of the stochastic SWE model are presented and the accuracy estimated.

5.1 Polynomial chaos approximation

Consider a probability space $(\mathbf{\Omega}, \mathcal{A}, \mathcal{P})$ where $\mathbf{\Omega}$ is the event space, $\mathcal{A}$ is the σ-algebra of events and $\mathcal{P}$ is the probability measure. $\omega \in \mathbf{\Omega}$ is an elementary event in $\mathbf{\Omega}$. As suggested by Wiener [137], any random variable $f(\omega) \in L_2(\mathbf{\Omega})$ may be represented as the sum of a series of polynomials in independent Gaussian variables $\boldsymbol{\xi}(\omega) = (\xi_1(\omega), \cdots, \xi_d(\omega))$ [42, 88]. This is an example of *polynomial chaos expansion* (PCE),

$$f(\boldsymbol{\xi}) = \sum_{\alpha \in \mathcal{J}} f^{(\alpha)} H_\alpha(\boldsymbol{\xi}) \tag{5.1}$$

where $\alpha = (\alpha_1, \cdots, \alpha_d)$ is a multi-index, H_α is a d-variate, $|\alpha|_1$-order Hermite polynomial chaos (PC) detailed description of which can be found in, e.g. [86]. Such an expansion forms a complete basis in Hilbert space [64] and converges to any continuous L_2 functions in the L_2 sense [17]. The expansion is generalised by [142] to use polynomials from the Askey scheme [4] in non-Gaussian random variables.

For computational purpose the series in (5.1) is truncated in order to retain only a finite number of terms. One usually keeps those polynomials whose total degree $|\alpha|_1$ does not exceed a given integer p,

$$\hat{f}(\boldsymbol{\xi}) = \sum_{|\alpha|_1 \leq p} f^{(\alpha)} H_\alpha(\boldsymbol{\xi}) \tag{5.2}$$

The total number of terms in this truncated series is $M = (p+d)!/(p!d!)$.

Due to the orthogonality of H_α's with respect to Gaussian measure, the coefficient $f^{(\alpha)}$ of the PCE can be calculated by a Galerkin projection:

$$f^{(\alpha)} = \frac{\mathbb{E}[f(\boldsymbol{\xi}) \cdot H_\alpha(\boldsymbol{\xi})]}{\mathbb{E}[H_\alpha^2(\boldsymbol{\xi})]} \tag{5.3}$$

This is known as a "non-intrusive" approach.

The coefficients of the PC expansion contain the complete probabilistic information of the model. They may be post-processed in order to estimate the statistics. For example, an estimate of the variance of $f(\boldsymbol{\xi})$ can be obtained directly from its p-order PC approximation by

$$\sigma_{f,p}^2 = \sum_{0<|\alpha|_1 \leq p} (f^{(\alpha)})^2 \cdot \mathbb{E}[H_\alpha^2(\boldsymbol{\xi})] \tag{5.4}$$

5.2 Approximation of stochastic SWE model

A numerical approximation of a complex model facilitates the exploration of its behaviours by representing the model in a simpler analytical form. This section presents PC and KLE approximations of the stochastic SWE model, which also serve as data compression techniques.

5.2.1 PC approximation

Let the vector $\mathcal{U} = (h, u_x, u_y)^T$ denotes the result of the stochastic SWE model in which h specifies water level and $(u_x, u_y)^T$ velocity. The form $\mathcal{U}(\boldsymbol{x}, t, \boldsymbol{\xi})$ emphasises that $\mathcal{U}$ is a function of spatial, temporal variables and random variables. On making the assumption that $\mathcal{U} \in L_2$ and continuous, $\mathcal{U}$ has such a PC approximation,

$$\hat{\mathcal{U}}(\boldsymbol{x}, t, \boldsymbol{\xi}) = \sum_{|\alpha|_1 \leq p} \mathcal{U}^{(\alpha)}(\boldsymbol{x}, t) H_\alpha(\boldsymbol{\xi}) \tag{5.5}$$

where

$$\mathcal{U}^{(\alpha)}(\boldsymbol{x}, t) = \frac{\mathbb{E}[\mathcal{U}(\boldsymbol{x}, t, \boldsymbol{\xi}) \cdot H_\alpha(\boldsymbol{\xi})]}{\mathbb{E}[H_\alpha^2(\boldsymbol{\xi})]} \tag{5.6}$$

The estimation of the right-hand side of (5.6) has to be done by numerical integrations.

The approximation in equation (5.5) is fully represented by the M coefficients, which is most likely a much smaller data than those required by a population of collocation points of $\mathcal{U}$.

5.2.2 Further approximation by KLE

$\hat{\mathcal{U}}(\boldsymbol{x}, t, \boldsymbol{\xi})$ can be further approximated by using Karhunen-Loève expansion (KLE). Since the spatial covariance function can be obtained from the PC coefficients,

$$\mathsf{C}(\boldsymbol{x}_1, \boldsymbol{x}_2, t) = \operatorname{cov}\big[\hat{\mathcal{U}}(\boldsymbol{x}_1, t),\, \hat{\mathcal{U}}(\boldsymbol{x}_2, t)\big] = \sum_{0<|\alpha|_1 \leq p} \mathcal{U}^{(\alpha)}(\boldsymbol{x}_1, t) \cdot \mathcal{U}^{(\alpha)}(\boldsymbol{x}_2, t) \cdot \mathbb{E}[H_\alpha^2(\boldsymbol{\xi})]$$

an $\mathcal{M}$-term KLE approximation of $\hat{\mathcal{U}}(\boldsymbol{x}, t, \boldsymbol{\xi})$ is

$$\hat{\hat{\mathcal{U}}}(\boldsymbol{x}, t, \boldsymbol{\xi}) = \mathcal{U}^{(0)}(\boldsymbol{x}, t) + \sum_{i=1}^{\mathcal{M}} \sqrt{\lambda_i(t)}\, \theta_i(t, \omega) \phi_i(\boldsymbol{x}, t) \tag{5.7}$$

where $\mathcal{U}^{(0)}(\boldsymbol{x},t)$ denotes $\mathcal{U}^{(\alpha)}(\boldsymbol{x},t)$ with $|\alpha|_1 = 0$, i.e. the mean of $\mathcal{U}(\boldsymbol{x},t,\xi)$. For every fixed t value, $\{\theta_i(t,\omega)\}$ is a set of random variables, $\{\lambda_i(t)\}$ and $\{\phi_i(\boldsymbol{x},t)\}$ are the eigenvalues and the eigenfunctions of $\mathsf{C}(\boldsymbol{x}_1,\boldsymbol{x}_2,t)$, i.e., they are the solutions of the Fredholm integral equation,

$$\int_{\mathbf{D}} \mathsf{C}(\boldsymbol{x}_1,\boldsymbol{x}_2,t)\varphi_i(\boldsymbol{x}_1,t)\mathrm{d}\boldsymbol{x}_1 = \lambda_i(t)\phi_i(\boldsymbol{x}_2,t) \quad \forall\, i = 1,2,\ldots \tag{5.8}$$

where $\mathbf{D}$ is the spatial domain of the model. The random variable $\theta_i(t,\omega)$ is given by

$$\theta_i(t,\omega) = \frac{1}{\sqrt{\lambda_i(t)}} \int_{\mathbf{D}} \left[\hat{\mathcal{U}}(\boldsymbol{x},t,\xi) - \mathcal{U}^{(0)}(\boldsymbol{x},t)\right]\phi_i(\boldsymbol{x},t)\mathrm{d}\boldsymbol{x} \quad \forall\, i = 1,2,\ldots \tag{5.9}$$

If again approximate $\theta_i(t,\omega)$ by a truncated PC series,

$$\hat{\theta}_i(t,\omega) = \sum_{|\alpha|\le p} \theta_i^{(\alpha)}(t) H_\alpha(\boldsymbol{\xi}(\omega)) \tag{5.10}$$

its coefficients can be obtained by projecting equation (5.9) onto each $H_\alpha(\xi)$ basis, which yields

$$\theta_i^{(\alpha)}(t) = \begin{cases} 0, & |\alpha|_1 = 0 \\ \frac{1}{\sqrt{\lambda_i(t)}} \int_{\mathbf{D}} \mathcal{U}^{(\alpha)}(\boldsymbol{x},t)\phi_i(\boldsymbol{x},t)\mathrm{d}\boldsymbol{x}, & 0 < |\alpha|_1 \le p \end{cases} \tag{5.11}$$

5.2.3 Numerical result

Applying the approximation (5.5) and (5.7) subsequently to the stochastic SWE model, with $p = 3$ in (5.5) and $\mathcal{M} = 30$ in (5.7), each of the three random fields $h(\boldsymbol{x},t,\boldsymbol{\xi})$, $u_x(\boldsymbol{x},t,\boldsymbol{\xi})$ and $u_y(\boldsymbol{x},t,\boldsymbol{\xi})$ can have a truncated KLE representation $\hat{\hat{h}}(\boldsymbol{x},t,\boldsymbol{\xi})$, $\hat{\hat{u}}_x(\boldsymbol{x},t,\boldsymbol{\xi})$ and $\hat{\hat{u}}_y(\boldsymbol{x},t,\boldsymbol{\xi})$ in the form of (5.7), the random variables θ_i for each of h, u_x and u_y can be obtained by (5.10) and (5.11).

Figure 5.1 displays the probability density function of some θ_i for $\hat{\hat{h}}(\boldsymbol{x},60,\boldsymbol{\xi})$ estimated by 10^5 QMC realisations of $\hat{\theta}_i$. Figure 5.2 displays the corresponding eigenfunctions $\phi_i(\boldsymbol{x},60)$. Figure 5.3 shows the declining of the eigenfunctions $\lambda_i(60)$ for $\hat{\hat{h}}(\boldsymbol{x},60,\boldsymbol{\xi})$.

Figure 5.4 to 5.9 shows the statistics fields concluded from the PC approximation $\hat{\mathcal{U}}(\boldsymbol{x},t,\boldsymbol{\xi})$.

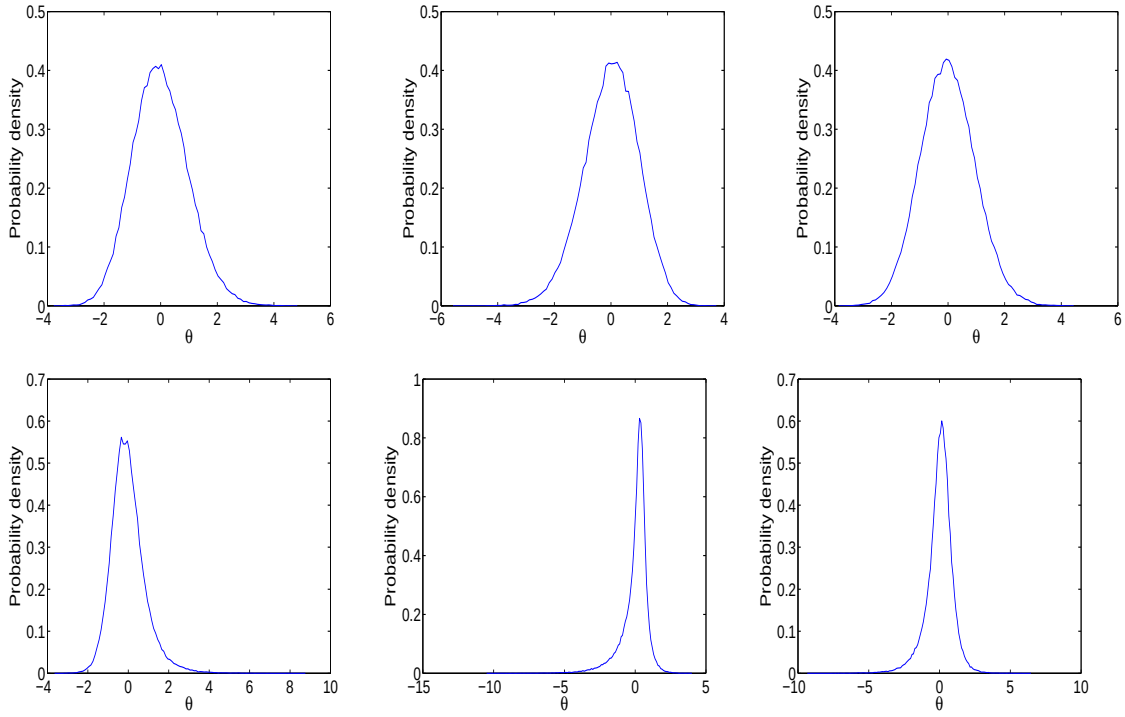

Figure 5.1: Approximated pdf of θ_1, θ_2, θ_3 (1st row), θ_5, θ_{10} and θ_{20} (2nd row), for $\hat{\hat{h}}(\boldsymbol{x}, 60, \boldsymbol{\xi})$

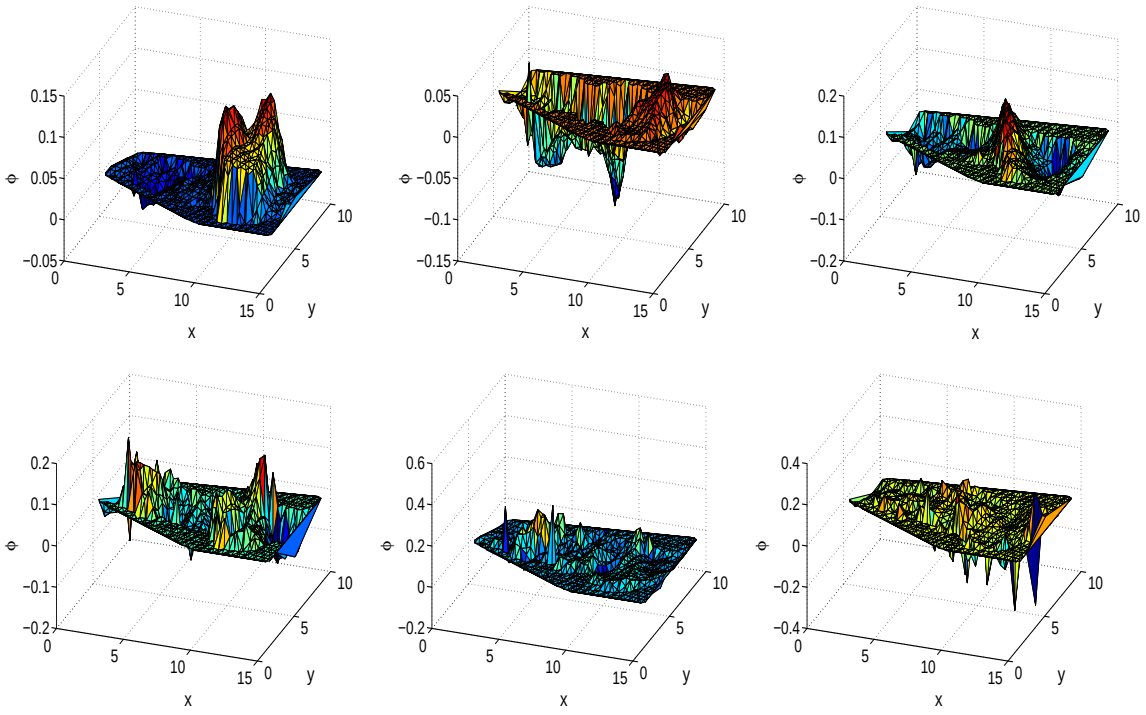

Figure 5.2: Eigenfunctions ϕ_1, ϕ_2, ϕ_3 (1st row), ϕ_5, ϕ_{10} and ϕ_{20} (2nd row), for $\hat{\hat{h}}(\boldsymbol{x}, 60, \boldsymbol{\xi})$

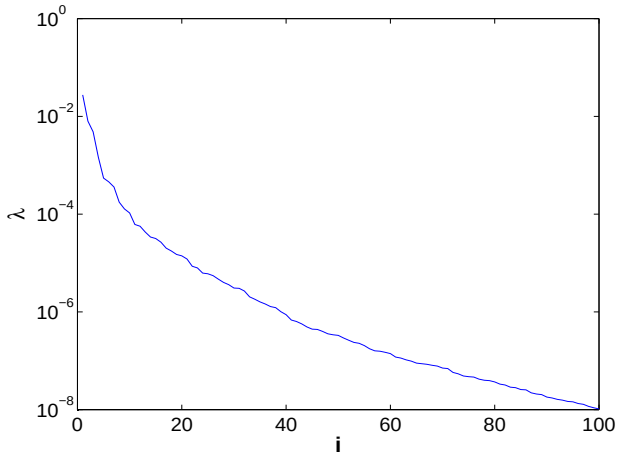

Figure 5.3: Declining eigenvalues for $\hat{\hat{h}}(\boldsymbol{x}, 30, \boldsymbol{\xi})$

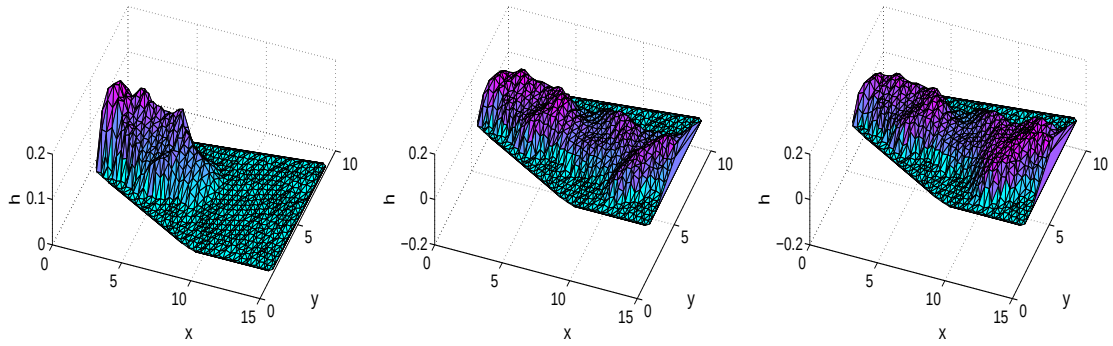

Figure 5.4: Mean values of $h(\boldsymbol{x}, 10)$, $h(\boldsymbol{x}, 20)$ and $h(\boldsymbol{x}, 40)$

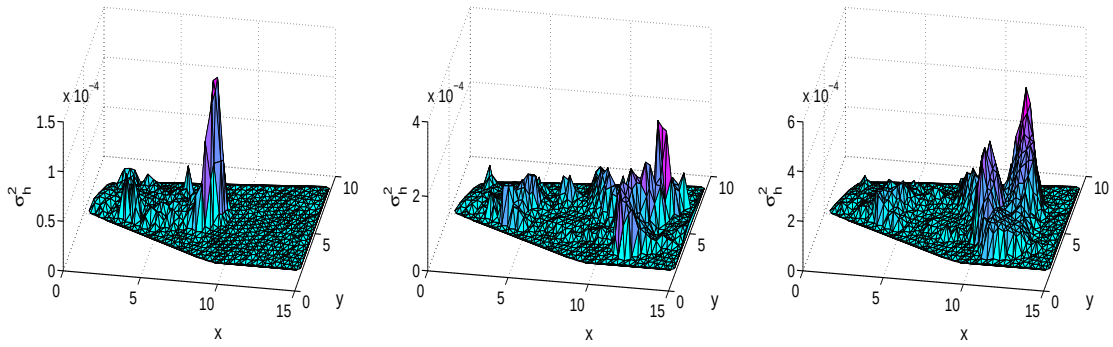

Figure 5.5: Variances of $h(\boldsymbol{x}, 10)$, $h(\boldsymbol{x}, 20)$ and $h(\boldsymbol{x}, 40)$

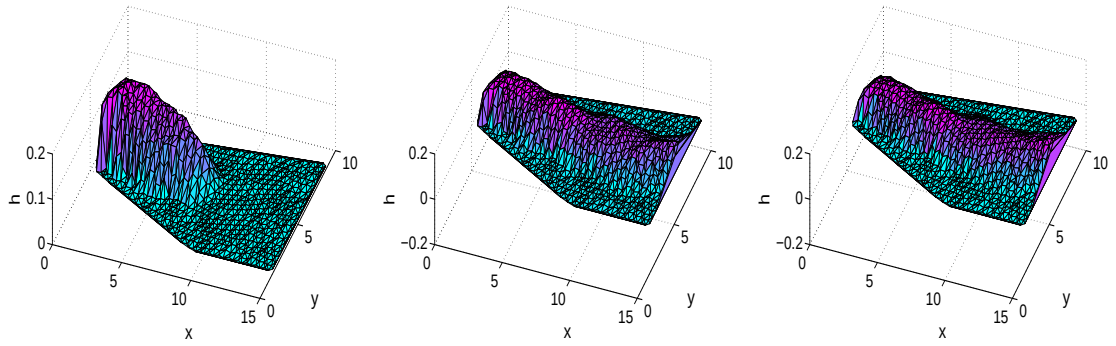

Figure 5.6: Mean values of $u_x(\boldsymbol{x}, 10)$, $u_x(\boldsymbol{x}, 20)$ and $u_x(\boldsymbol{x}, 40)$

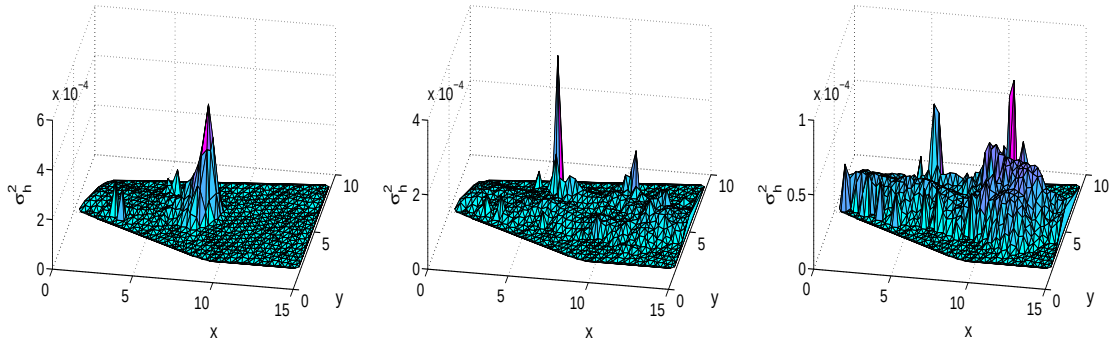

Figure 5.7: Variances of $u_x(\boldsymbol{x}, 10)$, $u_x(\boldsymbol{x}, 20)$ and $u_x(\boldsymbol{x}, 40)$

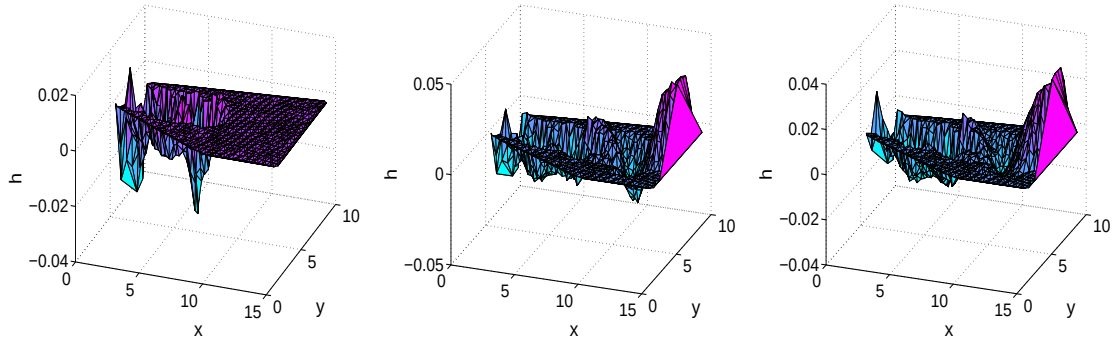

Figure 5.8: Mean values of $u_y(\boldsymbol{x}, 10)$, $u_y(\boldsymbol{x}, 20)$ and $u_y(\boldsymbol{x}, 40)$

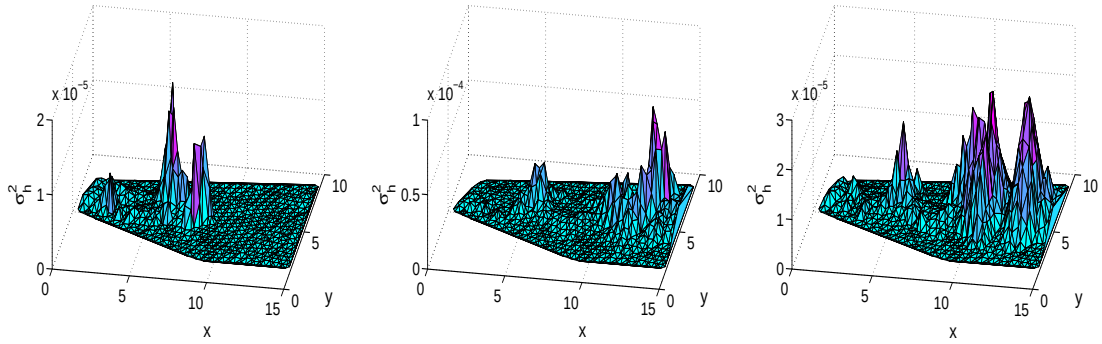

Figure 5.9: Variances of $u_y(\boldsymbol{x}, 10)$, $u_y(\boldsymbol{x}, 20)$ and $u_y(\boldsymbol{x}, 40)$

5.2.4 Data compression

Comparing to a collocation representation of $\mathcal{U}(\boldsymbol{x}, t, \boldsymbol{\xi})$, the PC and PC/KLE approximations need to store less data. They condense the information of collocation points into PC coefficients and KLE terms which are much smaller in number. Table 5.1 shows the difference of data size demanded by three types of model representation. The PC approximation is made with $p = 3$ which generates $M = 220$ terms, the KLE approximation keeps $\mathcal{M} = 30$ terms. Collocation points on t has an interval $2s$.

Numb. collocation points	Collocation representation	PC approximation	PC/KLE approximation
10^2	1.2×10^2	380	67
10^4	1.2×10^4	380	67
10^6	1.2×10^6	380	67

Table 5.1: Data size demanded by model representations (unit: MB)

5.3 Accuracy of PC approximation

The PC approximation $\hat{f}$ in (5.2) approaches to f in a mean square sense as p increases, however this is only an asymptotic property while in most of the cases p is small. It is important to access the error of this approximation for every particular application.

The error of the PC approximation comes majorly from two sources, one is the truncation of terms as in (5.2), the other is the estimation of coefficient $f^{(\alpha)}$ in (5.3) which involves numerical integrations if the explicit close-form expression of f is not known.

The error caused by truncation of terms depends on the smoothness of f [11]. In [69] this error is observed on univariate functions which have explicit close-form expressions so that the coefficient $f^{(\alpha)}$ can be derived exactly to exclude the second source of error. The results show that the rate of convergence is problem-dependent.

It is also observed that in some cases the convergence is slow, or not improved by adding terms, or even diverging within the range of p observed.

In [21] and [103] 2-D random flow approximations by Hermite PC are shown to be failures. However, Micro-channel flow with random boundary conditions is successfully approximated by Hermite PC in [143] with an assumption of large covariance length for the random field.

To assess the accuracy of a PC approximation, a cross-validation technique [124, 40] can be used. This method divides the sampled data set into two subsets, an approximation is built from one subset, i.e. the training set, and its accuracy is assessed by comparing it to the other subset, i.e. the test set. Let $\mathcal{U}$ be the stochastic SWE model, $\hat{\mathcal{U}}(\boldsymbol{\xi})$ be its truncated PC approximation based on a training set and $\mathcal{Y} = \{\mathcal{U}(\boldsymbol{\xi}_i)\}_{i=1}^N$ be the test set, the *normalised empirical mean-square error* is,

$$\epsilon^*[\hat{\mathcal{U}}] = \frac{1}{N \cdot \mathrm{var}(\mathcal{Y})} \sum_{i=1}^{N} (\hat{\mathcal{U}}(\boldsymbol{\xi}_i) - \mathcal{U}(\boldsymbol{\xi}_i))^2 \tag{5.12}$$

where $\mathrm{var}(\mathcal{Y})$ is the empirical variance of $\mathcal{Y}$. The *determination coefficient* is

$$\mathscr{Q}^2[\hat{\mathcal{U}}] = 1 - \epsilon^*[\hat{\mathcal{U}}]$$

which is a measure of quality of the approximation.

The error of the PC approximation of $\mathcal{U}(\boldsymbol{x}, t, \boldsymbol{\xi})$ is believed to vary along $\boldsymbol{x}$ and t. To investigate this error field is difficult because of the lack of reference measure for $\mathcal{U}$ in the full spatial and temporal domain. Since $\{h_{30}^{(i)}\}_{i=1}^3$ have their reference measures readily available, they are chosen to be approximated by PCE for the purpose of error investigation.

The $\{h_{30}^{(i)}\}_{i=1}^3$ are approximated by their PCE representation $\{\hat{h}_{30}^{(i)}\}_{i=1}^3$ with polynomials in 9 independent Gaussian random variables, up to order 6. The coefficients of the PCE are estimated by a QMC integration with 10^6 sample points.

Let $\widehat{\mathrm{var}}[h_{30}^{(i)}]$ be the estimated variance obtained from $\hat{h}_{30}^{(i)}$ as in (5.4), and $\mathrm{var}[h_{30}^{(i)}]$ be the reference measure of the variance obtained by 10^6 QMC samples of the stochastic SWE model. Then the normalised empirical errors of variance in these approximations are defined as

$$\epsilon_{\sigma^2}^{(i)} = \frac{|\widehat{\mathrm{var}}[h_{30}^{(i)}] - \mathrm{var}[h_{30}^{(i)}]|}{\mathrm{var}[h_{30}^{(i)}]}$$

whose values are tabulated in Table 5.2. The normalised empirical mean square error $\epsilon_*^{(i)} = \epsilon^*[\hat{h}_{30}^{(i)}]$ is obtained by (5.12) with a test set consist of 10^4 points, and is tabulated in Table 5.3.

The numerical results show the error of the PC approximations for the stochastic SWE model is not negligible, The error magnitudes on the three spatial point differ significantly. Since all the measures approximated is at the same temporal point, it is not clear whether the error magnitudes also differ significantly along temporal dimension. The results also show the error is not monotonically reducing with increasing number of terms. This non-monotonicity is probably caused by the integration error in the estimation of PC coefficients, or may also be ascribed to the discontinuities in the model which violate the condition whereon the convergence of PCE is assumed.

PC order	Numb. of terms	$\epsilon_{\sigma^2}^{(1)}$	$\epsilon_{\sigma^2}^{(2)}$	$\epsilon_{\sigma^2}^{(3)}$
$p = 1$	10	0.2581	0.2449	0.0460
$p = 2$	55	0.0608	0.1382	0.0162
$p = 3$	220	0.0198	0.1068	0.0129
$p = 4$	715	0.0163	0.0947	0.0087
$p = 5$	2002	0.0067	0.0541	0.0647
$p = 6$	5005	0.1198	1.0808	0.5655

Table 5.2: Normalised empirical error of variance of PC approximations

PC order	Numb. of terms	$\epsilon_{*}^{(1)}$	$\epsilon_{*}^{(2)}$	$\epsilon_{*}^{(3)}$
$p = 1$	10	0.2589	0.2464	0.0461
$p = 2$	55	0.0613	0.1345	0.0160
$p = 3$	220	0.0192	0.1054	0.0133
$p = 4$	715	0.0176	0.1073	0.0161
$p = 5$	2002	0.0275	0.2305	0.0860
$p = 6$	5005	0.1490	1.2555	0.5861

Table 5.3: Normalised empirical mean-square error of PC approximations

5.4 Conclusion

The PC and KLE approximations of the stochastic SWE model are presented. These approximations facilitate faster evaluations of the model, and generate much smaller size of data than a collocation representation. A preliminarily accuracy assessment shows the error of the PC approximations is not negligible and not easy to predict which might be due to the low regularity of the model.

Chapter 6

Conclusions

The findings and contributions of the present thesis are summarised below.

Uncorrelated Dimensions Quadratures Two novel numerical integration techniques, uncorrelated dimensions (UD) quadrature and compound uncorrelated dimensions (CUD) quadrature, are originally developped in this work. Theoretical analysis and numerical experiments agree on that for an integrand that can be expressed in a multilinear functional of any integrable functions, UD quadrature has a convergence rate $\mathcal{O}(N^{-1})$ if the integrand is of bounded variation, the rate for CUD quadrature is $\mathcal{O}(N^{-2})$ if the integrand belongs to C^2 space and with uniformly distributed variables, N is the number of evaluations. Both the two rates are independent of the number of dimensions. This is a break to the "curse of dimensions". UD and CUD quadratures implicitly split multidimensional integrations into functions of 1-D integrations. This is achieved by so arrange the abscissas that the sampled correlation among the contributions from all dimensions is minimised.

Numerical Integrations for Statistics Five numerical techniques are compared on their efficiency of integration, namely sparse grid Gauss-Hermite (SGH) quadrature, sparse grid linear finite element method (SLFEM), Monte Carlo (MC) quadrature, quasi-Monte Carlo (QMC) quadrature, and UD quadrature. The comparison shows that UD and QMC quadrature are the best choices for the purpose and the techniques based on polynomial interpolations do not perform well, which can be ascribed to the low regularity of the model.

Spectral Approximation of the Model Polynomial chaos (PC) and Karhunen-Loève expansion (KLE) approximations of the stochastic SWE model are implemented in this work. This constructs response surface representations of the model in term of Hermite polynomial chaos of independent Gaussian variables. The approximations are shown to be effective approaches for data compression and fast exploration, though a preliminary estimation shows the error is not negligible which can be ascribed to the low regularity of the stochastic SWE model.

Appendix A

Symbols and Abbreviations

A.1 Latin Symbols

B_t	An arbitrary subset of $\{1, 2, \ldots, d\}$
$\mathcal{B}$	A union of certain B_t's
$\mathbf{C}$	Covariance matrix of random fields
C^2	Functions with continuous derivatives up to second order
$C_{t,i}$	$\mathrm{cov}(\phi_{b_i}\ ,\ \phi_{b_{i+1}}\phi_{b_{i+2}}\cdots\phi_{b_{z_t}})$ for $B_t \subseteq S$
$\mathbf{D}$	Spatial domain of a random field
d	Number of dimensions
$H_\alpha(\xi)$	Hermite polynomial chaos
$h^{(i)}_{\max}$	Maximum water level at the i-th gauge point during the 120s period
$h^{(i)}_{30}$	Water level at the i-th gauge point at the time 30th second
$\mathcal{J}^d$	Union of all J_α with $\alpha \in \mathbb{N}, \alpha \leq 2^{d-1}$
K	Number of sample points of a 1-D mid-point quadrature
M	Number of retained KLE terms
m	Level of slash grid
$\boldsymbol{m}$	A vector containing m_i each for the i-th dimension
N	Number of sample points of a multidimensional quadrature
$\mathrm{Q}^{\mathcal{M}}_N$	Monte Carlo quadrature with N samples
$\mathrm{Q}^{\mathcal{Q}}_N$	Quasi-Monte Carlo quadrature with N samples
$\mathrm{Q}^{J_\alpha}_K$	Uncorrelated dimensions quadrature with K samples
Q^{C}_N	Compound uncorrelated dimensions quadrature with N samples
$\mathrm{r}(\boldsymbol{x}, \omega)$	A random field
$\mathbf{r}(\omega)$	A spatially discretised random field
S	The integer set $\{1, 2, \ldots, d\}$
$U^d_{J_\alpha}$	D-dimensional slash grid
U^d	D-dimensional compound slash grid
$W^{q,p}$	Sobolev space. $f \in W^{q,p}$ has derivatives up to order $q-1$ continuous and $f^{(q)} \in L^p$
$\mathcal{X}^K$	Abscissas of a K-point mid-point rule
$\boldsymbol{X}$	Abscissas of a quadrature
$\boldsymbol{X}_{J_\alpha,K}$	Abscissas of a uncorrelated dimensions quadrature
$\boldsymbol{X}_{C,K}$	Abscissas of a compound uncorrelated dimensions quadrature

A.2 Greek Symbols

Θ	$[-\infty, \infty]^d$, domain of random variables
λ_1, λ_2	Two permuting functions for slash grid
ξ	Independent Gaussian random variables
ϕ, φ	1-D integrable functions
Ψ	A multilinear function
Ω	$[0, 1]^d$, domain of random variables
$\mathbf{\Omega}$	Event space of random variables

A.3 Abbreviations

CSG	Compound slash grid
CUD	Compound uncorrelated dimensions
DEM	Digital elevation model
DRH	Direct runoff hydrograph
ERH	Excess rainfall hyetograph
IUH	Instantaneous unit hydrograph
KLE	Karhunen-Loève expansion
MC	Monte Carlo
NSE	Navier-Stokes equations
PC	Polynomial chaos
PCE	Polynomial chaos expansion
PDF	Probability density function
PRNG	Pseudo-random number generator
QMC	Quasi-Monte Carlo
SG	Slash grid
SGH	Sparse grid Gauss-Hermite quadrature
SLFEM	Sparse grid linear finite element method
SMI	Splitable multidimensional integration
SWE	Shallow water equations
UD	Uncorrelated dimensions
UH	Unit hydrograph

Appendix B

Tables of $\boldsymbol{m}$ values

$\boldsymbol{m} = (m_1, \ldots, m_{d-1})$ used for UD or CUD quadratures are values in the below tables **plus** 10^8 element-wise. E.g., if $d = 3$, $\boldsymbol{m}$ for UD quadrature with $K = 10$ is $\boldsymbol{m} = (100000009, 100000017)$.

$\boldsymbol{m}$ values for UD quadrature

K	m_1	m_2	m_3	m_4	m_5	m_6	m_7	m_8
10	9	17	11	9	19	19	1	19
20	11	27	29	21	19	9	31	39
30	57	31	3	7	7	27	1	39
40	11	31	29	39	33	51	51	59
50	91	91	41	57	9	19	3	19
100	17	63	9	107	93	19	151	33
200	339	37	77	263	213	383	11	227
300	277	561	177	163	399	403	411	261
400	471	437	161	273	427	633	597	237
500	183	843	677	313	723	627	61	699
1000	1219	79	377	929	343	93	427	1739
2000	427	699	2119	3769	119	711	2961	1507
3000	5413	3537	1627	2259	1821	2577	3007	4611
4000	2841	1511	7147	6817	6593	7061	6129	4599
5000	1221	5289	1711	7433	3183	1983	8093	8879
10000	18137	6441	269	7707	529	17577	6233	4741
20000	23877	24099	6349	28949	2843	22479	22889	21287
30000	39117	45291	13437	8367	21549	40627	42337	54619
40000	11863	11931	13711	20771	58881	70621	47219	4907
50000	64083	59321	46507	60183	51183	28717	68561	79869

m values for CUD quadrature

K	m_1	m_2	m_3	m_4	m_5	m_6	m_7	m_8
10	13	17	3	11	1	11	9	3
20	9	3	31	21	17	13	7	33
30	27	1	37	1	37	19	31	39
40	51	27	61	7	7	67	63	19
50	7	89	43	69	17	79	13	41
100	161	169	169	193	31	187	71	137
200	259	53	291	269	9	329	251	263
300	361	297	241	43	319	337	141	579
400	683	381	437	39	629	737	229	471
500	891	651	467	93	809	929	467	781
1000	1519	1821	1153	87	89	297	1063	731
2000	3239	3097	3267	1139	63	1017	2551	3461
3000	2467	2673	1417	73	5197	2893	4851	5427
4000	1449	4903	1903	6191	7837	6831	7089	6641
5000	1949	4123	2629	1339	437	9141	4387	1377
10000	6223	16183	13389	3953	4687	7011	9441	9323
20000	7847	1223	38559	35401	22201			
30000	3367	14581	54319	34761	1219			
40000	6201	37057	9243	16227	26341			
50000	59627	10319	14839	26881				

List of Figures

List of Tables

Bibliography

[1] M. B. Abbott. *Computational hydraulics : elements of the theory of free surface flows*. Ashgate, Aldershot, Hants, 1992.

[2] G. Acrement Jr. and V. Schneider. Guide for selecting Manning's roughness coefficients for natural channel and floodplains. Technical report, 1989. Technical Report WSP2339, USGS, Prepared in cooperation with the U.S. Department of Transportation, Federal Highway Administration.

[3] R. J. Adler and J. E. Taylor. *Random Fields and Geometry*. Springer-Verlag, Berlin, 2007.

[4] R. Askey and J. Wilson. *Some basic hypergeometric orthogonal polynomials that generalize Jacobi polynomials*. Number 319 in Memoirs of the American Mathematics Society. Providence, Rhode Island, 1985.

[5] G. Augusti, C. Borri, and H.-J. Niemann. Is aeolian risk as significant as other environmental risks? *Reliability engineering & system safety*, 74:227–238, 2001.

[6] D. Avnir, O. Biham, D. Lidar, and O. Malcai. Is the geometry of nature fractal? *Science*, 279:39–40, 1998.

[7] Harry H. Barnes Jr. Roughness characteristics of natural channels. U. S. Geological Survey, Water Supply Paper 1849, Washington DC, 1967.

[8] J. I. Barredo. Normalised flood losses in Europe: 1970–2006. *Nat. Hazards Earth Syst. Sci.*, 9:97–104, 2009.

[9] G. K. Batchelor. *An introduction to fluid dynamics*. Cambridge Univ., Cambridge, 1967.

[10] G. Berz. Flood disaster: Lessons from the past-worries for the future. *Water and Maritime Engineering*, 142(1):1–10, 2000.

[11] G. Blatman and B. Sudret. Sparse polynomial chaos expansions and adaptive stochastic finite elements using a regression approach. *Comptes Rendus Mécanique*, 336(6):518–523, 2008.

[12] Rafael L. Bras. *Hydrology: An Introduction to Hydrologic Science*. Addison-Wesley series in civil engineering. Addison-Wesley, 1989.

[13] Paul Bratley, Bennett L. Fox, and Harald Niederreiter. Programs to generate Niederreiter's low-discrepancy sequences. *ACM Trans. Math. Softw.*, 20(4):494–495, 1994.

[14] H-J. Bungartz and M. Griebel. Sparse grids. *Acta Numerica*, 13:147–269, 2004.

[15] P. L. Butzer and R. J. Nessel. *Fourier analysis and approximation*, volume 1. Basel, Birkhäuser, 1971.

[16] R. E. Caflisch. Monte Carlo and quasi-Monte Carlo methods. *Acta Numerica*, 7:1–49, 1998.

[17] R. H. Cameron and W. T. Martin. The orthogonal development of nonlinear functionals in series of Fourier-Hermite functionals. *Ann. Math.*, 48, 1947.

[18] Hydraulic Engineering Center. Accuracy of computed water surface profiles. Technical report, Hydraulic engineering Center, Davis, Calif., 1986.

[19] M. A. Cesare. First order analysis of open-channel flow. *Journal of Hydraulic Engineering*, 117(2):242–247, 1991.

[20] Alexandre Joel Chorin. Hermite expansions in Monte-Carlo computation. *Journal of Computational Physics*, 8(3):472–482, 1971.

[21] Alexandre Joel Chorin. Gaussian fields and random flow. *Journal of Fluid Mechanics*, 63:21–32, 1974.

[22] Ven Te Chow. *Open-channel Hydraulics*. McGraw-Hill, New York, 1959.

[23] Ven Te Chow, David R. Maidment, and Larry W. Mays. *Applied hydrology*. McGraw-Hill, New York, 1988.

[24] N. J. Clifford, A. Robert, and K. S. Richards. Estimation of flow resistance in gravel-bedded rivers: A physical explanation of the multiplier of roughness length. *Earth Surface Processes and Landforms*, 17:111–126, 1992.

[25] Ronald Cools and Philip Rabinowitz. Monomial cubature rules since "Stroud": a compilation. *Journal of Computational and Applied Mathematics.*, 48:309–326, 1993.

[26] R. Courant and D. Hilbert. *Methods of mathematical physics*. Interscience Publ., New York, 1962.

[27] W. L. Cowan. Estimating hydraulic roughness coefficients. *Agric. Engrg.*, 37:473–475, 1956.

[28] W. E. H. Culling. The characterization of regular/irregular surfaces in the soil-covered landscape by Gaussian random-fields. *Comput. Geosci.*, 15(2):219–, 1989.

[29] W. E. H. Culling and M. Datko. The fractal geometry of the soil covered landscape. *Earth Surf. Proc. Landforms*, 12:369–, 1987.

[30] Richard Dawson, Jim Hall, Paul Sayers, Paul Bates, and Corina Rosu. Sampling-based flood risk analysis for fluvial dike system. *Stoch. Environ. Res. Risk Assess.*, 19:388–402, 2005.

[31] A. Defina, L. D'Alpaos, and B. Matticchio. A new set of equations for very shallow water and partially dry areas suitable to 2D numerical models. In P. Molinaro and L. Natale, editors, *Modelling Flood Propagation over Initially Dry Areas*, pages 72–81, New York, 1994. American Society of Civil Engineers.

[32] J. J. Dronkers. *Tidal computations in rivers and coastal waters*. North-Holland Publ., Amsterdam, 1964.

[33] B. Engquist and A. Majda. Absorbing boundary conditions for the numerical simulation of waves. *Math. Comp.*, 31:629–651, 1977.

[34] W. Feller. *An introduction to probability theory and its applications*, volume 2. Wiley, 2nd edition, 1971.

[35] G. S. Fishman. *Monte Carlo: concepts, algorithms, and applications*. Springer series in operation research. Springer Verlag, 1995.

[36] R. French. *Open Channel Hydraulics*. McGraw-Hill, New York, 1986.

[37] Humberto A. Gallegos, Jochen E. Schubert, and Brett F. Sanders. Two-dimensional, high-resolution modeling of urban dam-break flooding: A case study of Baldwin Hills, California. *Advances in Water Resources*, 2009. In press.

[38] Jochen Garcke. Sparse grid tutorial. `http://www.math.tu-berlin.de/~garcke/paper/sparseGridTutorial.pdf`, 2008.

[39] J. R. Garratt. Review of drag coefficients over oceans and continents. *Monthly Weather review*, 105(7):915–929, 1977.

[40] S. Geisser. The predictive sample reuse method with applications. *J. Amer. Stat. Assoc.*, 70:320–328, 1975.

[41] A. C. Genz. Testing multidimensional integration routines. In *Tools, Methods and Languages for Scientific and Engineering Computation*, pages 81–94, 1984.

[42] Roger G. Ghanem and Pol D. Spanos. *Stochastic finite elements : a spectral approach*. Springer, New York, 1991.

[43] A. E. Gill. *Atmosphere-Ocean Dynamics*. Acad. Press, 1982.

[44] J.A. Gonçalves and A.M. Oliveira. Accuracy Analysis of DEMs Derived from ASTER Imagery. In *Geo-Imagery Bridging Continents*, volume XXXV, pages 389–, Istanbul, Turkey, July 2004. XXth ISPRS Congress.

[45] M. Griebel. A parallelizable and vectorizable multi-level algorithm on sparse grids. In W. Hackbusch, editor, *Parallel algorithms for partial differential equations, Proceedings of the sixth GAMM-seminar, Notes on Numerical Fluid Mechanics*, volume 31, pages 94–100, 1991.

[46] P. Groen and G. W. Groves. Surges. In M. N. Hill, editor, *The Sea*, volume 1. Interscience, 1962.

[47] V. M. Gupta, E. Waymire, and C. T. Wang. A representation of an IUH from geomorphology. *Water Resources Research*, 16(5):855–862, 1980.

[48] C. T. Haan. *Statistical Methods in Hydrology*. Iowa State Univ. Pr., Ames, Iowa, 1979.

[49] G. J. Haltiner and R. T. Williams. *Numerical prediction and dynamic meteorology*. Wiley, New York, 1980.

[50] S. M. Hashemian, A. Abootalebi, and F. Kianifar. Accuracy Evaluation of DEM Generated From SPOT5-HRS Imageries. In *Geo-Imagery Bridging Continents*, volume XXXV, pages 389–, Istanbul, Turkey, July 2004. XXth ISPRS Congress.

[51] M. C. Hendershott. *Evolution of physical oceanography*, chapter Long waves and ocean tides. MIT Press, 1981.

[52] F. M. Henderson. *Open Channel Flow*. Macmillan, New York, 1966.

[53] R. W. Herschey. *Streamflow Measurement*. E & FN Spon, London, 1995.

[54] R. W. Herschey. The uncertainty in a current meter measurement. *Flow Measurement and Instrumentation*, 13:281–284, 2002.

[55] R. L. Higdon. Absorbing boundary conditions for difference approximations to the multi-dimensional wave equations. *Math. Comp.*, 47(176):437–459, 1986.

[56] R. L. Higdon. Absorbing boundary conditions for the wave equation. *Math. Comp.*, 49(179):65–90, 1987.

[57] Michael Hilden. *Extensions of shallow water equations*. PhD thesis, Univ. of Kaiserslautern, Kaiserslautern, 2003.

[58] A. Hjelmfelt and M. Wang. General stochastic unit hydrographs. *Journal of irrigation and drainage engineering, ASCE*, 120(1):138–148, 1994.

[59] M. S. Horritt. Development of physically based meshes for two-dimensional models of meandering channel flow. *International Journal of Numerical Methods in Engineering*, 47:2109–2137, 2000.

[60] M. S. Horritt. Stochastic modelling of 1-D shallow water flows over uncertain topography. *Journal of Computational Physics*, 180:327–338, 2002.

[61] M. S. Horritt. A linearized approach to flow resistance uncertainty in a 2-D finite volume model of flood flow. *Journal of Hydrology*, 316:13–27, 2006.

[62] L. K. Hua and Y. Wang. *Applications of Number Theory to Numerical Analysis*. Science Press, Beijing, 1981.

[63] N. M. Hunter, P. D. Bates, M. S. Horritt, and M. D. Wilson. Simple spatially-distributed models for predicting flood inundation: A review. *Geomorphology*, 90:208–225, 2007.

[64] Svante Janson. *Gaussian Hilbert spaces*. Cambridge Univ. Press, 1997.

[65] R. D. Jarret. Hydraulics of high-gradient streams. *Journal of Hydraulic Engineering*, 110:1519–1539, 1984.

[66] E. T. Jaynes. *Probability theory : The logic of science*. Cambridge Univ. Press, Cambridge, 2003.

[67] C. X. Jin. A deterministic Gamma-type geomorphologic instantaneous unit hydrograph based on path types. *Water Resources Research*, 28(2):479–486, 1992.

[68] Peggy A. Johnson. Uncertainty of Hydraulic Parameters. *Journal of Hydraulic Engineering*, 122(2):112–114, 1996.

[69] R. V. Field Jr. and M. Grigoriub. On the accuracy of the polynomial chaos approximation. *Probabilistic Engineering Mechanics*, 19:65–80, 2004.

[70] Andreas Keese. A Review of Recent Developments in the Numerical Solution of Stochastic Partial Differential Equations (Stochastic Finite Elements). Technical report, Institute of Scientific Computing, Technical University Braunschweig, 2003. Informatikbericht Nr.: 2003-06.

[71] J. W. Kirchner, W. E. Dietrich, F. Iseya, and H. Ikeda. The variability of critical shear stress,friction angle, and grain protrusion in water-worked sediments. *Sedimentology*, 37:647–672, 1990.

[72] Ronald Kleiss and Achilleas Lazopoulos. Error in Monte Carlo, quasi-error in quasi-Monte Carlo. *Computer Physics Communications*, 175(2):93–115, 2006.

[73] D. E. Knuth. *The Art of Computer Programming*, volume 2. Addison Wesley, 3rd edition, 1998. Seminumerical Algorithms.

[74] W. Kornus, R. Alamús, A. Ruiz, and J. Talaya. Assessment of DEM Accuracy Derived From Spot-5 High Resolution Stereoscopic Imagery. In *Geo-Imagery Bridging Continents*, volume XXXV, pages 445–, Istanbul, Turkey, July 2004. XXth ISPRS Congress.

[75] Arnold R. Krommer and Christoph W. Ueberhuber. *Numerical integration on advanced computer systems*. Springer, Berlin, 1994.

[76] Martin Krosche. Statistische auswertung numerischer simulationen. Master's thesis, Institute of Scientific Computing, Technical University of Braunschweig, 2005.

[77] Z. W. Kundzewicz. Non-structural Flood Protection and Sustainability. *IWRA, Water International*, 27(1):3–13, 2002.

[78] B. Le Méhauté. *An introduction to hydrodynamics and water waves*. Springer, New York, 1976.

[79] Jonathan K. Lee and David C. Froehlich. *Review of literature on the finite-element solution of the equations of two-dimensional surface-water flow in the horizontal plane : A review of computational approaches to implementing finite-element solutions of the shallow-water equations*. U. S. Geological Survey, Denver, Colo., 1987.

[80] L. B. Leopold, M. G. Wolman, and J. P. Miller. *Fluvial processes in geomorphology*. W. H. Freeman, San Francisco, 1964.

[81] Jason K. Levy and Jim Hall. Advances in flood risk management under uncertainty. *Stoch. Environ. Res. Risk Assess.*, 19:375–377, 2005.

[82] J. T. Limerinos. Determination of the manning coefficient from measured bed roughness in natural channels. U. S. Geological Survey, Water Supply Paper 1898-B, Federal Center, Colo., 1970.

[83] Benoit B. Mandelbrot. *The fractal geometry of nature*. Freeman, New York, 1983.

[84] G. Marsaglia and W. W Tsang. The ziggurat method for generating random variables. *Journal of Statistical Software*, 5(8), 2000.

[85] M. Mascagni et al. *SPRNG 2.0, scalable parallel pseudo-random number generator library version 2.0*. Florida State University, Tallahassee, 1999.

[86] Hermann G. Matthies. Uncertainty quantification with stochastic finite elements. In E. Stein, R. de Borst, and T. R. J. Hughes, editors, *Encyclopedia of Computational Mechanics*. John Wiley & Sons, Chichester, 2007.

[87] Hermann G. Matthies, Christoph E. Brenner, Christian G. Bucher, and C. Guedes Soares. Uncertainties in probabilistic numerical analysis of structures and solids– stochastic finite elements. *Structual Safety*, 19(3):283–336, 1997.

[88] Hermann G. Matthies and Andreas Keese. Galerkin methods for linear and nonlinear elliptic stochastic partial differential equations. *Comp. Meth. Appl. Mech. Engrg.*, 194:1295–1331, 2005.

[89] L. W. Mays and L. Coles. Optimization of unit hydrographs determination. *Journal of the Hydraulics Division, American Society of Civil Engineers*, 106(HY1):85–97, 1980.

[90] L. W. Mays and C. K. Taur. Unit hydrographs via nonlinear programming. *Water Resources Research*, 18(4):744–752, 1982.

[91] L. W. Mays and Y. K. Tung. *Hydrosystems engineering and management*. McGraw-Hill, New York, 1992.

[92] Bryan Mercer. DEMs Created from Airborne IFSAR, an Update. In *Geo-Imagery Bridging Continents*, volume XXXV, pages 841–, Istanbul, Turkey, July 2004. XXth ISPRS Congress.

[93] E. Mignot, A. Paquier, and S. Haider. Modeling floods in a dense urban area using 2D shallow water equations. *Journal of Hydrology*, 237(1-2):186–199, 2006.

[94] William J. Morokoff and Russel E. Caflisch. Quasi-Monte Carlo integration. *Journal of Computational Physics*, 122:218–230, 1995.

[95] J. E. Nash. The form of instantaneous unit hydrograph. *International Association of Scientific Hydrology Publication*, 45(3):114–121, 1957.

[96] Jeffrey C. Neal, Paul D. Bates, Timothy J. Fewtrell, Neil M. Hunter, Matthew D. Wilson, and Matthew S. Horritt. Distributed whole city water level measurements from the carlisle 2005 urban flood event and comparison with hydraulic model simulations. *Journal of Hydrology*, 368:42–55, 2009.

[97] Harald Niederreiter. *Random Number Generation and Quasi-Monte Carlo Methods*. SIAM, Philadelphia, 1992.

[98] J. C. J. Nihoul. *Modelling of Marine Systems*. Elsevier, Amsterdam, 1975.

[99] V. L. Nikora, D. G. Goring, and B. J. F. Biggs. On gravel-bed roughness characterisation. *Water Resources Research*, 34:517–527, 1998.

[100] Erich Novak and Klaus Ritter. High dimensional integration of smooth functions over cubes. *Numerische Mathematik*, 75:79–97, 1996.

[101] U. S. Army Corps of Engineers. Risk-analysis for flood damage reduction studies. Technical Report Rep. No. EM 1110-2-1619, Washington D.C., 1996.

[102] H. J. M. Ogink, J. G. Grijsen, and A. J. H. Wijbenga. Aspects of flood level computations. In *Flood Frequency and Risk Analysis*. Baton Rouge, USA, 1986.

[103] Steven A. Orszag and L. R. Bissonnette. Dynamical properties of truncated Wiener-Hermite expansions. *Phys. Fluids*, 10:2603–2613, 1967.

[104] F. Pappenberger, P. Matgen, K. J. Beven, J. B. Henry, L. Pfister, and P. De Fraipont. The influence of rating curve uncertainty on flood inundation predictions. In D. Reeve, editor, *Flood Risk Assessment*, pages 107–116. Institute of Mathematics and its Applications, 2004.

[105] P. M. Pelletier. Uncertainties in the single determination of river discharge: A literature review. *Canadian Journal of Civil Engineering*, 15:834–850, 1988.

[106] O. M. Phillips. *The dynamics of upper ocean*. Combridge University Press, London, 2nd edition, 1977.

[107] T. Pliefke, S. Sperbeck, U. Peil, and H. Budelmann. A standardized methodology for managing disaster risk - An attempt to remove ambiguity. In Luc Taerwe and Dirk Proske, editors, *Proceedings of the 5th International Probabilistic Workshop*, Ghent, Belgium, 2007.

[108] Nikolaas Praagman. *Numerical solution of the shallow water equations by a finite element method*. PhD thesis, Techn. Hochschule. Delft, Delft, 1979.

[109] W. H. Press, S. A. Teukolsky, W. T. Vetterling, and B. P. Flannery. *Numerical Recipes in Fortran 90*. Cambridge University Press, 2002.

[110] Qazi I. Rahman and G. Schmeisser. Characterization of the Speed of Convergence of the Trapezoidal Rule. *Numerical mathematik*, 57:123–138, 1990.

[111] I. Rodriguez-Iturbe and J. B. Valdes. The geomorphologic structure of hydrologic response. *Water Resource Research*, 15(5):1409–1420, 1979.

[112] E. Rosenblueth. Two-points estimates in probabilities. *Applied Mathematical Modelling*, 5:329–335, 1981.

[113] J. C. Russ. *Fractal surfaces*. Plenum Press, London, 1994.

[114] Sarino and S. E. Serrano. Development of the instantaneous unit hydrograph using stochastic differential equations. *Stochastic Hydrology and Hydraulics*, 4(2):151–160, 1990.

[115] R. Schürer. A Comparison between (Quasi-)Monte Carlo and Cubature Rule Based Methods for Solving High-dimensional Integration Problems. *Computers in Simulation*, 62(3–6):509–517, 2003.

[116] S. E. Serrano, H. R. Whitley, and R. W. Irwin. Effects of agricultural drainage on streamflow in the Middle Thames River, Ontario, 1949-1980. *Canadian Journal of Civil engineering*, 12:875–885, 1985.

[117] L. K. Sherman. Streamflow from rainfall by the unit-graph method. *Engineering News Records*, 108:501–505, 1932.

[118] Y. I. Shokin and L. B. Chubarow. *Theoretical and experimental fluid mechanics*, chapter Finite-difference simulation of tsunami propagation. Springer, Berlin, 1981.

[119] Vijay P. Singh. *Hydrologic systems: Rainfall-runoff modeling*, volume 1. Prentice Hall, Englewood Cliffs, NJ, 1988.

[120] S. A. Smolyak. Quadrature and interpolation formulas for tensor products of certain class of functions. *Sov. Math. Dokl.*, 4:240–243, 1963.

[121] S. Soares-Frazão. *Dam-break induced flow in complex topographies, theoretical, numerical and experimental approaches*. PhD thesis, University Catholique de Louvain, Louvain-la-Neuve, Belgium, 2002.

[122] S. Soares-Frazão, B. Noel, B. Spinewine, and Y. Zech. IMPACT WP3 : The isolated building test case : results from the IMPACT benchmark. In *EC Contract EVG1-CT-2001-00037 IMPACT Investigation of Extreme Flood Processes and Uncertainty, Proceedings 3rd Project Workshop*, Louvain-la-Neuve, Belgium, 2003.

[123] S. Soares-Frazão and G. Testa. Numerical model analysis: The Toce River test case. In *CADAM Proceedings, Milan Meeting*, 1999. `http://www.hrwallingford.co.uk/projects/CADAM/CADAM/Milan/MI2.pdf`.

[124] M. Stone. Cross-validatory choice and assessment of statistical predictions. *J. Royal Stat. Soc. Series B*, 36:111–147, 1974.

[125] A. H. Stroud. *Approximate Calculation of Multiple Integrals*. Prentice-Hall, Englewood Cliffs, NJ, 1971.

[126] B. Sudret and A. Der Kiureghian. Stochastic Finite Element Methods and Reliability, A State-of-Art Report. Technical report, Department of Civil and Environmental Engineering, University of California, Berkeley, CA, 2000.

[127] A. Sundström. Boundary conditions for limited area integration of the viscous forecast equations. *Beitr. zur Physik der Atmosphäre*, 50:218–224, 1977.

[128] Weiyan Tan. *Shallow water hydrodynamics : mathematical theory and numerical solution for a two-dimensional system of shallow water equations*. Water and Power Press, Beijing, China, 1992.

[129] Guido Testa, David Zuccala, Francisco Alcrudo, Jontan Mulet, and Sandra Soares-Frazão. Flash flood flow experiment in a simplified urban district. *Journal of Hydraulic Research*, 45 Extra Issue:37–44, 2007.

[130] G. K. Verboom and A. Slob. Weakly-reflective boundary conditions for two-dimensional shallow water flow problems. *Adv. Water Resources*, 7:192–197, 1984.

[131] C. B. Vreugdenhil. *Numerical Methods for Shallow-Water Flow*. Kluwer, Dordrecht, 1994.

[132] X. Wan and G. E. Karniadakis. Long-term behavior of polynomial chaos in stochastic flow simulations. *Comput. Meth. Appl. Math. Engrg.*, 195:5582–5596, 2006.

[133] Xiaoliang Wan, Dongbin Xiu, and George Em Karniadakis. Stochastic solutions for the two-dimensional advection-diffusion equation. *SIAM Journal on Scientific Computing*, 26(2):578–590, 2004.

[134] J. A. C. Weideman. Numerical integration of periodic functions: A few examples. *The American mathematical monthly*, 109(11):21–36, 2002.

[135] M. G. F. Werner, N. M. Hunter, and P. D. Bates. Identifiability of distributed floodplain roughness values in flood extent estimation. *Journal of Hydrology*, 314:139–157, 2005.

[136] Pieter Wesseling. *Principles of Computational Fluid Dynamics*. Springer, Berlin, 2001.

[137] N. Wiener. The homogeneous chaos. *Amer. J. Math.*, 60:897–936, 1938.

[138] Ellen E. Wohl. Uncertainty in Flood Estimates Associated with Roughness Coefficient. *Journal of Hydraulic Engineering*, 124(2):219–223, 1998.

[139] Zhang Xinhua, Long Wenfei, Xie Heping, Zhu Jiahua, and Wang Jiangping. Numerical simulation of flood inundation processes by 2D shallow water equations. *Front. Archit. Civ. Eng. China*, 1(1):107–113, 2007.

[140] D. Xiu, D. Lucor, C. H. Su, and G. E. Karniadakis. Stochastic modeling of flow-structure interactions using generalized polynomial chaos. *J. Fluids Eng.*, 124:51–59, 2002.

[141] Dongbin Xiu. Fast numerical methods for stochastic computations: A review. *Communications in Computational Physics*, 5(2–4):242–272, 2009.

[142] Dongbin Xiu and George Em Karniadakis. The Wiener–Askey Polynomial Chaos for Stochastic Differential Equations. *SIAM Journal on Scientific Computing*, 24(2):619–644, 2002.

[143] Dongbin Xiu and George Em Karniadakis. Modeling uncertainty in flow simulations via generalized polynomial chaos. *Journal of Computational Physics*, 187:137–167, 2003.

[144] J. C. Yang, S. Y. Tarng, and Y. K. Tung. Analyzing Uncertainty of IUH of Nash. In Hsieh Wen Shen, editor, *Hydraulic engineering '93 : proceedings of the 1993 conference, San Francisco, California*, volume 2, pages 1927–1933, New York, NY, July 1993. Hydraulics Division of the American Society of Civil Engineers, American Society of Civil Engineers.

[145] K. C. Yeh and Y. K. Tung. Uncertainty and sensitivity analyses of pit-migration model. *Journal Hydraulic Engineering*, 119(2):262–283, 1993.

[146] K. C. Yeh, J. C. Yang, and Y. K. Tung. Regionalization of unit hydrograph parameters: 2. uncertainty analysis. *Stochastic Hydrology and Hydraulics*, 11(2):173–192, 1997.

[147] H. Yserentant. On the Multi-Level Splitting of Finite Element Spaces. *Numerische Mathematik*, 49:379–412, 1986.

[148] H. Yserentant. Hierarchical bases. In R. E. O'Malley et al., editors, *Proc. ICIAM'91*, Philadelphia, 1992. SIAM.

[149] Sheng Yue et al. Approach for Describing Statistical Properties of Flood Hydrograph. *Journal of Hydrologic Engineering*, 7(2):147–153, 2002.

[150] M. W Zemansky. *Heat and Thermodynamics*. McGraw-Hill, New York, 4th edition, 1957.

[151] C. Zenger. Sparse grids. In W. Hackbusch, editor, *Parallel algorithms for partial differential equations, Proceedings of the sixth GAMM-seminar, Notes on Numerical Fluid Mechanics*, volume 31, pages 241–251, 1991.

[152] Xinhua Zhang, S. Oishi, H. Ishidaira, and K. Takeuchi. Practical Aspects in the Simulation of Flood Inundation Using 2D Shallow Water Equations on A Complex Land-Cover . *J. Japan Soc. Hydrol. and Water Resour.*, 16(5):501–517, 2003.

[153] B. Zhao, Y. K. Tung, and J. C. Yang. Determination of unit hydrograph by multiple storm analysis. *Stochastic Hydrology and Hydraulics*, 8:269–280, 1994.

[154] Olgierd Cecil Zienkiewicz and Robert Leroy Taylor. *The finite element method: Fluid dynamics*, volume 3. Butterworth-Heinemann, Oxford, 5th edition, 2002.